

ENVIRONMENTAL NOISE IN GRAVITATIONAL WAVE DETECTORS AND
THE SEARCH FOR GRAVITATIONAL WAVE SIGNALS ASSOCIATED WITH
GAMMA-RAY BURSTS DURING LIGO'S THIRD OBSERVING RUN

by

PHILIPPE DAI-QUANG NGUYEN

A DISSERTATION

Presented to the Department of Physics
and the Division of Graduate Studies of the University of Oregon
in partial fulfillment of the requirements
for the degree of
Doctor of Philosophy

July 2022

© 2022 Philippe Dai-Quang Nguyen
All rights reserved.

DISSERTATION ABSTRACT

Philippe Dai-Quang Nguyen

Doctor of Philosophy

Department of Physics

July 2022

Title: ENVIRONMENTAL NOISE IN GRAVITATIONAL WAVE DETECTORS AND THE SEARCH FOR GRAVITATIONAL WAVE SIGNALS ASSOCIATED WITH GAMMA-RAY BURSTS DURING LIGO'S THIRD OBSERVING RUN

This dissertation describes methods used for characterizing the sources and effects of environmental noise in Advanced LIGO detectors from the end of the second LIGO-Virgo observing run through the end of the third observing run. We present the vibrational and magnetic noise budgets for the Hanford and Livingston observatories, results of noise studies focusing on scattered light sources in the Hanford detector and input beam jitter at both detectors, and a system of routine magnetic coupling measurements to track changes throughout an observing run. We describe the implementation of an automated pipeline for determining the effect of environmental noise signals on gravitational wave events.

Noise plays a critical role in understanding the limitations and areas of potential improvement for analyses searching for gravitational waves. We discuss the targeted search for gravitational waves associated with gamma-ray bursts during the third observing run. No gravitational waves were detected coincident with the 86 GRBs analyzed. New upper limit exclusion distances are set for various signal waveform types, and we report exclusion probabilities for specific models.

We discuss the relevance of transient noise on the performance of unmodeled search pipelines.

This dissertation contains previously published co-authored material.

CURRICULUM VITAE

NAME OF AUTHOR: Philippe Dai-Quang Nguyen

GRADUATE AND UNDERGRADUATE SCHOOLS ATTENDED:

University of Oregon, Eugene, OR, USA
California Polytechnic State University, San Luis Obispo, CA, USA

DEGREES AWARDED:

Doctor of Philosophy, Physics, 2022, University of Oregon
Bachelor of Science, Physics, 2016, Cal Poly San Luis Obispo

AREAS OF SPECIAL INTEREST:

Gravitational Wave Astrophysics

PROFESSIONAL EXPERIENCE:

Research Assistant, Department of Physics, University of Oregon, 2017-
present
Teaching Assistant, Department of Physics, University of Oregon, 2016-2019

GRANTS, AWARDS AND HONORS:

PUBLICATIONS:

Abbott, R., et al. (2021). Search for intermediate mass black hole binaries
in the third observing run of Advanced LIGO and Advanced Virgo.
Astronomy & Astrophysics, 659, A84.

- Abbott, R., et al. (2022). Search for Gravitational Waves Associated with Gamma-Ray Bursts Detected by Fermi and Swift during the LIGO–Virgo Run O3b. *The Astrophysical Journal*, 928(2), 186.
- Buikema, A., et al. (2020). Sensitivity and performance of the Advanced LIGO detectors in the third observing run. *Physics Review D*, 102, 062003.
- Davis, D., et al. (2021). LIGO detector characterization in the second and third observing runs. *Classical Quantum Gravity*, 38(13), 135014.
- Fiori I., Effler A., Nguyen P., Paoletti F., Schofield R.M.S., Tringali M.C. (2021) Environmental Noise in Gravitational-Wave Interferometers. In: Bambi C., Katsanevas S., Kokkotas K.D. (eds) Handbook of Gravitational Wave Astronomy. Springer, Singapore.
- Nguyen, P., et al. (2021). Environmental noise in Advanced LIGO detectors. *Classical Quantum Gravity*, 38(14), 145001.

ACKNOWLEDGEMENTS

Acknowledgments go here.

TABLE OF CONTENTS

Chapter	Page
I. INTRODUCTION	1
II. GRAVITATIONAL WAVES	4
2.1. General Relativity	5
2.1.1. Linear gravity	7
2.1.2. Gravitational wave solutions	10
2.2. Sources of gravitational waves	13
2.2.1. Compact binary mergers	13
2.2.2. Continuous wave sources	16
2.2.3. Burst sources	16
2.2.4. Stochastic background	18
2.3. Multi-messenger astronomy	19
2.4. GWs associated with GRBs	21
2.4.1. Short gamma-ray bursts	23
2.4.2. Long gamma-ray bursts	27
III.GRAVITATIONAL WAVE DETECTORS	30
3.1. GW interferometry	30
3.2. Advanced LIGO	33
3.3. Noise sources	36
IV.METHODS FOR STUDYING ENVIRONMENTAL NOISE	41
4.1. The PEM sensor array	42
4.1.1. Monitoring the monitors with ligocam	44
4.2. Environmental noise injections	46

Chapter		Page
4.2.1.	Vibrational injections	48
4.2.1.1.	Beating-shakers technique	49
4.2.1.2.	Impulse injections	52
4.2.2.	Magnetic injections	53
4.3.	Coupling functions	54
4.3.1.	Single coupling site, sensor, and injection	54
4.3.2.	Multiple coupling sites, sensors, and injections	56
4.3.3.	Solving the coupling equations	58
4.4.	Uncertainties and limitations of coupling functions	63
4.4.1.	Comparison to transfer functions	63
4.4.2.	Assumptions about coupling mechanisms	64
4.4.3.	Hardware limitations	65
4.5.	The pemcoupling package	69
4.5.1.	Processing steps	70
4.5.2.	Data products	72
V.	STUDIES OF ENVIRONMENTAL NOISE DURING O3	74
5.1.	Evaluation of coupling functions	75
5.2.	Vibrational noise studies during O3	77
5.2.1.	Scattered light at the HAM5/6 septum	79
5.2.2.	Search for the source of a 48-Hz peak	83
5.2.3.	Input beam jitter	85
5.3.	Magnetic noise studies during O3	86
5.4.	Validation of gravitational wave event candidates	91
5.4.1.	Past methods	92
5.4.2.	Automated validation of O3 events	94

Chapter	Page
5.4.3. Science Case Study of S200114f	96
5.4.4. Event validation in O4	97
5.4.4.1. Coupling function tuning	100
5.4.4.2. Grouping nearby sensors	102
VI.GRAVITATIONAL WAVES ASSOCIATED WITH GAMMA-RAY BURSTS	103
6.1. GW searches	103
6.1.1. X-Pipeline	103
6.1.2. Vetoing noise signals	109
6.2. O3b search for GWs associated with GRBs	112
6.2.1. Results of the O3b search	116
6.2.2. Noise effects in the generic transient search	119
6.2.3. Model exclusion	122
VII CONCLUSION	125
APPENDICES	
A. PEMCOUPLING EXAMPLES	128
B. PEMCHECK EXAMPLES	134
REFERENCES CITED	137

LIST OF FIGURES

Figure	Page
1. Timeline of the discovery of GW170817 and its electromagnetic counterparts.	20
2. Hardness ratios (HR) vs. T_{90} s of Fermi GRBs, showing the distinction between short and long bursts. Reproduced from Bhat et al. (2016)	24
3. Layout of a Michelson interferometer with Fabry-Pérot arm cavities.	32
4. Full optical layout of an Advanced LIGO interferometer (Kissel, 2017).	34
5. Full noise budgets of the LIGO Hanford (top) and Livingston (bottom) observatories at the end of the third observing run.	37
6. The PEM system layout at LLO during O3, as seen on the PEM public website.	43
7. Standard locations for vibration and magnetic injections at the LHO corner station (left), Y end station (top right), and X end stations (bottom right).	46
8. Injection equipment photos	48
9. Comparison of the old small-coil comb magnetic field injections with the new large-coil broadband injections.	54
10. Diagram of a trivial coupling function measurement in the trivial case.	57
11. Expanding Figure 10 to more than one sensor and coupling site.	58
12. Example of a broadband acoustic noise injection and measurement of a single-injection coupling function	61
13. Ambient noise level for the LHO HAM6 Y-axis accelerometer	63

Figure	Page
14. Single-injection coupling functions (upper limits not shown) for the HAM5 Y-axis accelerometer for three different shaker injection locations (on top of HAM5, on top of HAM6, and on the HAM5 chamber door).	66
15. Magnetic coupling function uncertainty.	67
16. Constant-Q transforms of the GW strain channel (left) and an accelerometer (right) during thunder noise at LLO.	76
17. DARM noise from all <i>vibrational</i> coupling sources at LHO (top) and LLO (bottom).	78
18. Spectra of shaker injections exciting scattered light noise at the LHO output arm.	80
19. Time series (left) and spectrograms (right) of a vibrational impulse injection produced at the output arm of the LHO detector.	81
20. Change in HAM5/6 vibrational coupling before and after the replacement of the septum window.	82
21. ASD of a vibrational injection at the LHO input arm exciting a 48-Hz resonance feature in DARM.	83
22. Spectrograms of DARM and various accelerometers near the input arm and beam splitter showing a beating-shakers injection at 48 Hz.	84
23. Improvement in jitter coupling at LHO after test mass replacement.	86
24. DARM noise from all <i>magnetic</i> coupling sources at LHO (top) and LLO (bottom).	87
25. LHO magnetic coupling measured by the last five wall-mounted coil injections performed in O3.	89
26. Time-lines of magnetic coupling changes relative to the start of the observing run.	89
27. Weekly trends in frequency (top) and amplitude (top) of peaks in the magnetic coupling functions.	90
28. Probability spectrogram of an ETMY accelerometer at LLO and a constant-Q transform of the GW strain channel	99
29. Coupling function tuning and the resulting probability spectrogram	101

Figure	Page
30. Example waveform of a ADI-B injection at 100 Mpc. Parameters are given in Table 4.	108
31. Coherent consistency cut performed by x-pipeline to veto noise triggers.	111
32. Gaussianity measures around the time of GRB191101A without autogating.	114
33. Distribution of off-source triggers in the LIGO detectors without autogating. The x- and y-axes are the signal energy in H1 and L1, respectively.	115
34. Detection efficiency of ADI-C injected waveforms without (left) and with (right) autogating.	116
35. Cumulative distribution of p-values for the loudest on- source events of the O3b X-pipeline analyses.	117
36. Cumulative distributions of O3b exclusion distances for 150-Hz sine-Gaussian and ADI-A waveforms.	118
37. Cumulative distributions of O3a and O3b exclusion distances for the ADI-C (top) and 300-Hz sine-Gaussian (bottom) waveforms.	121
38. Cumulative distributions of CSG-300 Hz exclusion distances (top) and the detector network antenna factors (bottom) for GRBs before and after the implementation of RC tracking.	122
39. Histogram of redshift measurements for GRBs detected by Swift BAT.	123
A.1. HTML page for a single-injection coupling function run.	129
A.2. Coupling function in physical units for the Y-axis HAM 5/6 septum accelerometer from a broadband acoustic injection.	130
A.3. Coupling function in ADC counts for the Y-axis HAM 5/6 septum accelerometer from a broadband acoustic injection.	130
A.4. Estimated ambient for the Y-axis HAM 5/6 septum accelerometer from a broadband acoustic injection.	131
A.5. Composite coupling function in physical units for the Y-axis HAM 5/6 septum accelerometer.	132

Figure	Page
A.6. Composite coupling function in physical units for the Y-axis HAM 5/6 septum accelerometer.	132
A.7. Estimated ambient for the Y-axis HAM 5/6 septum accelerometer.	133
A.8. Site-wide estimated ambient for all vibrational sensors at LLO.	133
B.1. Example for a long duration CBC merger candidate S190510g, overlapping with excess noise that is almost certainly associated with vibrational noise at ETMY.	134
B.2. Example for a burst candidate S190804qr reported by cWB, showing that a loud noise observed near ETMY could contribute to the GW event candidate signal but not with a high probability.	135
B.3. Example of a typical short-duration CBC merger candidate S200112r, with no excess noise expected to appear in the GW channel.	136

LIST OF TABLES

Table	Page
1. Specifications for injection equipment.	47
2. Number of injections performed at each station and for each injection type throughout the pre-, and post-O3 injection campaigns.	74
3. Noise projections for five helicopter flyovers at the LIGO detectors.	77
4. Parameters and properties for accretion disk instability waveform injections.	109
5. Median 90% exclusion distances (D_{90}) for the generic transient search during O3b.	119
6. Relative increase in median D_{90} for each x-pipeline simulated waveform.	119
7. Exclusion confidence for each injected waveform model.	124
A.1. Column descriptions for the single-injection coupling function output of the pemcoupling package.	131

CHAPTER I

INTRODUCTION

On April 1, 2019, the Laser Interferometer Gravitational-Wave Observatory (LIGO) collaboration ushered forth a new phase of gravitational wave (GW) astronomy as it began its third observing run, which ran in two six-month stages and concluded March 27, 2020. Together with their European counterpart Virgo, the two LIGO detectors would detect a total of 74 new GW signals throughout the third observing run (O3) (Abbott et al., 2021b, 2021c), over three times the detection rate in the first two runs. In the first observing run (O1) and the second observing run (O2), LIGO had already made the first detection of GWs from the inspiral of binary black hole and binary neutron star systems (GW150914 and GW170817, respectively) (B. P. Abbott et al., 2016b; Abbott et al., 2017a). The detections made in O3 include an additional detection of a binary neutron star merger (B. P. Abbott et al., 2020a), the first two detections of neutron star-black hole mergers (Abbott et al., 2021a), the first clear detection of an intermediate-mass black hole (R. Abbott et al., 2020), and a number of other black hole mergers that have expanded and challenged our understanding of black hole populations.

The dramatic increase in detection rate could not have been achieved without the myriad upgrades made to the LIGO and Virgo interferometers themselves (Buikema et al., 2020). These upgrades range from changes in the laser system to replacing core interferometer optics to mitigation of disruptive external signals. Studying the behavior of the detectors is crucial to finding new ways to improve their sensitivity and stability. Detector characterization involves deploying a wide array of data analysis tools and experimental tests to understand how noise

originating from within and outside of the detectors couples into the GW data stream (Davis et al., 2019, 2021b).

Despite our best efforts, unwanted noise signals still affect the detector in a number of ways. Short-duration transient signals, called *glitches*, impact analysis pipelines searching for GWs. Thus to keep up with the high event detection rates in O3 many analyses necessary in the validation of GW event candidates have been automated, with more sophisticated methods being developed for future observing runs.

This dissertation describes my contributions to GW astronomy along multiple avenues. First, Chapter II introduces gravitational wave emission from a general relativity framework. Chapter III describes the anatomy of a ground-based gravitational wave interferometer and the various limitations to its sensitivity. Chapter IV discusses methods I used to characterize environmental noise, unwanted signals originating from outside an interferometer. Chapter V presents the results of those methods during O3, an overview of several noise investigations in which those methods have played a crucial role, and the implementation of an automated algorithm for vetting GW detections.

The detection of a GW signal coincident with a short gamma-ray burst (GRB) originating from the binary neutron star merger GW170817 was a breakthrough moment for the astronomical community, shedding light on the mysterious properties of GRBs. Even as the LIGO and Virgo detectors improve, GW170817 was a fortunate discovery considering its incredibly close proximity (40 Mpc). Targeted searches for GWs associated with GRBs allow much more sensitive searches for potential joint observations, and are necessary for expanding our ability to make joint detections at greater distances. In the third observing run

I co-led a collaboration search for joint GW-GRB events. Chapter VI describes the connection between GWs and GRBs, presents results of the search, and discusses its implications and considerations for future analyses.

Finally, Chapter VII ends this dissertation with some closing remarks.

CHAPTER II

GRAVITATIONAL WAVES

The first observation of gravitational waves in 2015 (B. P. Abbott et al., 2016b) took place a century after Albert Einstein completed his general theory of relativity (Einstein, 1916). Einstein's original publication proposed that gravitational attraction was not mediated by a force as described by Newtonian physics, but rather it was caused by the curvature of space-time due to the presence of mass. He primarily discussed the relevance of general relativity to predicting gravitational redshift, the curvature of light rays, and the perihelion precession of the orbit of Mercury, a mystery that perplexed late nineteenth and early twentieth century astronomers. However, the idea that gravitational forces might propagate in the form of waves similar to electromagnetic waves had existed since it was first speculated by Henri Poincaré a decade prior (Henri, 1905), and Einstein would soon make the conjecture that his theory of general relativity could provide a robust mathematical framework for gravitational waves.

Initially, Einstein was not highly confident in his conjecture. Electromagnetic waves are typically produced in the form of dipole radiation, formed by a positive and negative electric charge, whereas no “negative mass” exists to produce an analogous gravitational dipole. His early efforts in making approximations to his field equations to yield wave-like solutions were mostly fruitless due to the complexity of the equations. Nevertheless progress made by Einstein and his collaborators over the following decades would culminate in a theory for gravitational radiation propagating as transverse waves that squeeze and stretch matter perpendicular to the direction of propagation.

This chapter gives an overview of the theoretical background necessary for understanding the emission of GWs (Section 2.1), following discussions from Creighton and Anderson (2011), Hartle (2003), Jaranowski and Krolak (2009), and Misner, Thorne, and Wheeler (1973), and describes known and expected sources of GW radiation (Section 2.2).

2.1 General Relativity

In Newtonian mechanics, gravitational attraction is described as the manifestation of a gravitational potential Φ generated by a source of mass density ρ :

$$\nabla^2 \Phi = 4\pi\rho. \quad (2.1)$$

General relativity relates the geometry of spacetime to the density and flux of energy and momentum through the Einstein field equations

$$G_{\mu\nu} = \frac{8\pi G}{c^4} T_{\mu\nu} \quad (2.2)$$

where c and G are the speed of light and gravitational constant, respectively, $G_{\mu\nu}$ is the Einstein tensor, analogous to the Newtonian potential Φ , and $T_{\mu\nu}$ is the energy-momentum tensor, analogous to ρ . Since the tensors are 4-by-4 and symmetric, eq. (2.2) represents ten separate equations, as opposed to the single Newtonian equation. The energy-momentum tensor represents not just the mass density (which is described by the T^{00} component alone) but also the momentum density (T^{i0} and T^{0j} terms, where $i, j = 1, 2, 3$) and the mechanical stress tensor (T^{ij}).

To unpack $G_{\mu\nu}$ we have to define some basic quantities of general relativity. The geometry of spacetime is described by the metric tensor $g_{\mu\nu}$, via the

relationship between the coordinate distances and the line element:

$$ds^2 = g_{\mu\nu} dx^\mu dx^\nu. \quad (2.3)$$

In a flat Minkowski spacetime, where the metric is

$$\eta_{\mu\nu} = \begin{pmatrix} -1 & 0 & 0 & 0 \\ 0 & 1 & 0 & 0 \\ 0 & 0 & 1 & 0 \\ 0 & 0 & 0 & 1 \end{pmatrix} \quad (2.4)$$

the line element is that of special relativity: $ds^2 = -c^2 dt^2 + dx^2 + dy^2 + dz^2$.

Analogous to Newton's laws of motion in classical mechanics, the geodesic equations dictate how free-falling particles in general relativity move through spacetime along geodesics

$$\frac{d^2 x^\mu}{ds^2} + \Gamma_{\alpha\beta}^\mu \frac{dx^\alpha}{ds} \frac{dx^\beta}{ds} = 0 \quad (2.5)$$

where

$$\Gamma_{\alpha\beta}^\mu = \frac{1}{2} g^{\mu\nu} (\partial_\alpha g_{\beta\nu} + \partial_\beta g_{\nu\alpha} - \partial_\nu g_{\alpha\beta}) \quad (2.6)$$

are called the Christoffel symbols. Equations (2.5)–(2.6) can be derived by asserting that vectors remain unchanged under parallel transport from one point to another within the spacetime described by $g_{\mu\nu}$. The Christoffel symbols thus encode the effects of curvature on otherwise straight paths; note that in rectilinear coordinates they vanish and eq. (2.5) reduces to the equation for a straight line.

A useful quantity is the Riemann curvature tensor

$$R_{\mu\nu\rho\sigma} = g_{\rho\lambda} (\partial_\mu \Gamma_{\nu\sigma}^\lambda - \partial_\nu \Gamma_{\mu\sigma}^\lambda + \Gamma_{\mu\eta}^\lambda \Gamma_{\nu\sigma}^\eta - \Gamma_{\nu\eta}^\lambda \Gamma_{\mu\sigma}^\eta) \quad (2.7)$$

from which we can define the Ricci tensor and its trace, the Ricci scalar:

$$R_{\mu\nu} = g^{\rho\sigma} R_{\rho\mu\sigma\nu} \quad (2.8)$$

$$R = g^{\mu\nu} R_{\mu\nu} \quad (2.9)$$

The Einstein tensor from eq. (2.2) can be written in terms of these quantities and the metric:

$$G_{\mu\nu} = R_{\mu\nu} - \frac{1}{2} R g_{\mu\nu} \quad (2.10)$$

2.1.1 Linear gravity

We define our coordinate system such that the metric can be expressed as the flat Minkowski metric $\eta_{\mu\nu}$ plus a small perturbation $|h_{\mu\nu}| \ll 1$: $g_{\mu\nu} = \eta_{\mu\nu} + h_{\mu\nu}$. This allows us to develop a linearized form of the field equations, which we can then solve to arrive at a theory of *weak* gravitational radiation. The Christoffel symbols become

$$\Gamma_{\alpha\beta}^\mu = \frac{1}{2} \eta^{\mu\nu} (\partial_\alpha h_{\beta\nu} + \partial_\beta h_{\nu\alpha} - \partial_\nu h_{\alpha\beta}) + \mathcal{O}(h^2). \quad (2.11)$$

Combining these with eq. (2.7) gives the linearized Riemann tensor:

$$R_{\mu\nu\rho\sigma} = \frac{1}{2} (\partial_\rho \partial_\nu h_{\mu\sigma} + \partial_\sigma \partial_\mu h_{\nu\rho} - \partial_\sigma \partial_\nu h_{\mu\rho} - \partial_\rho \partial_\mu h_{\nu\sigma} + \mathcal{O}(h^2)). \quad (2.12)$$

Thus we can write the linearized Ricci tensor

$$R_{\mu\nu} = \frac{1}{2} (\partial_\alpha \partial_\mu h_\nu^\alpha + \partial_\alpha \partial_\nu h_\mu^\alpha - \partial_\mu \partial_\nu h - \square h_{\mu\nu} + \mathcal{O}(h^2)) \quad (2.13)$$

and Ricci scalar

$$R = \eta_{\mu\nu} R^{\mu\nu} = \partial_\mu \partial_\nu h - \square h_{\mu\nu} + \mathcal{O}(h^2) \quad (2.14)$$

where $h = \eta^{\mu\nu} h_{\mu\nu}$ is the trace of the metric perturbation and \square is the Minkowski-spacetime D'Alembertian operator:

$$\square := \eta^{\mu\nu} \partial_\mu \partial_\nu = -\frac{1}{c^2} \partial_t^2 + \partial_x^2 + \partial_y^2 + \partial_z^2. \quad (2.15)$$

This yields the linearized Einstein tensor

$$G_{\mu\nu} = \frac{1}{2} (\partial_\mu \partial_\sigma \bar{h}_\nu^\rho + \partial_\nu \partial_\sigma \bar{h}_\mu^\rho - \square \bar{h}_{\sigma\rho} - \eta_{\mu\nu} \partial_\sigma \partial_\rho \bar{h}^{\sigma\rho}) + \mathcal{O}(h^2) \quad (2.16)$$

where $\bar{h}_{\mu\nu} := h_{\mu\nu} - \frac{1}{2} \eta_{\mu\nu} h$ is the trace-reversed metric perturbation (called so because its trace is $\bar{h} = -h$).

We can simplify these terms further by choosing the appropriate gauge. To do so we must first investigate how $g_{\mu\nu}$ behaves under a gauge transformation. Suppose we make a small transformation to the coordinate system

$$x^\alpha \rightarrow x'^\alpha = x^\alpha + \xi^\alpha. \quad (2.17)$$

The metric transforms as

$$g_{\alpha\beta} \rightarrow g'_{\alpha\beta} = \frac{\partial x^\mu}{\partial x'^\alpha} \frac{\partial x^\nu}{\partial x'^\beta} g_{\mu\nu}(x) \quad (2.18)$$

$$= g_{\alpha\beta} - \partial_\alpha \xi_\beta - \partial_\beta \xi_\alpha + \mathcal{O}((\partial\xi)^2). \quad (2.19)$$

or in terms of the metric perturbation,

$$g'_{\alpha\beta} = \eta_{\alpha\beta} + h_{\alpha\beta} - \partial_\alpha \xi_\beta - \partial_\beta \xi_\alpha + \mathcal{O}(h(\partial\xi), (\partial\xi)^2). \quad (2.20)$$

We can write this as $g'_{\alpha\beta} = \eta_{\alpha\beta} + h'_{\alpha\beta} + \mathcal{O}(h(\partial\xi), (\partial\xi)^2)$, from which we see how the perturbation has transformed:

$$h'_{\alpha\beta} = h_{\alpha\beta} - \partial_\alpha \xi_\beta - \partial_\beta \xi_\alpha \quad (2.21)$$

Trace-reversing again, we get

$$\bar{h}'_{\alpha\beta} = \bar{h}_{\alpha\beta} - \partial_\alpha \xi_\beta - \partial_\beta \xi_\alpha + \eta_{\alpha\beta} \eta^{\mu\nu} \partial_\mu \xi_\nu. \quad (2.22)$$

Analogous to the Lorenz gauge choice in electromagnetism, we assert the condition $\partial_\alpha \bar{h}^{\alpha\beta} = 0$ in this gauge and find ξ must satisfy

$$\square \xi_\beta = \partial_\mu \bar{h}_\beta^\mu. \quad (2.23)$$

Indeed solutions to this exist, therefore we are safe to make the gauge transformation. The Lorenz gauge condition is chosen because it results in the divergence terms (all but the \square term) of eq. (2.16) vanish. In doing so, we reduce

the linearized Einstein field equations to simply

$$-\square \bar{h}_{\mu\nu} + \mathcal{O}(h^2) = \frac{16\pi G}{c^4} T_{\mu\nu}. \quad (2.24)$$

In the Newtonian (slowly-varying) limit, the D'Alembertian operator becomes a spatial Laplace operator, and it can be shown (Creighton & Anderson, 2011) that the trace-reversed perturbation reduces to the Newtonian gravitational potential Φ and the energy-momentum tensor reduces to just the mass density, recovering the Poisson equation for Newtonian gravity: $\nabla^2 \Phi = 4\pi G\rho$.

2.1.2 Gravitational wave solutions

In vacuum, the energy-momentum tensor is zero so the field equation is simply $\square \bar{h}_{\mu\nu} = 0$, the solution to which is a monochromatic plane wave propagating at the speed of light:

$$\bar{h}_{\mu\nu} = A_{\mu\nu} \cos(k_\sigma x^\sigma - \phi_{\mu\nu}) \quad (2.25)$$

where $A_{\mu\nu}$ and $\phi_{\mu\nu}$ are the amplitude and phase of the wave. The 4-vector k^μ contains the frequency $k^0 = -\omega = -2\pi f$ and the wave vector \mathbf{k} pointing in the direction of propagation. The Lorenz gauge condition can now be expressed as $0 = \partial_\mu \bar{h}^{\mu\nu} = -k_\mu A^{\mu\nu} \sin(k_\alpha x^\alpha)$, which is satisfied if

$$k_\mu A^{\mu\nu} = 0. \quad (2.26)$$

This means that the plane wave only has components orthogonal to k_μ , i.e. it is transverse wave. Furthermore, eq. (2.26) sets four conditions on what was

originally ten components, so our choice of the Lorenz gauge has reduced the number independent components in the solution to six.

In the slowly-varying case the gauge condition can be further restricted by making the metric perturbation purely spatial, ($h_{00} = h_{0i} = 0$) and traceless ($h = h_i^i = 0$). In this *transverse-traceless (TT) gauge*, we write the metric perturbation as $h_{\mu\nu}^{TT}$ (no overline necessary because in this gauge $\bar{h}_{\mu\nu} = h_{\mu\nu}$). These gauge conditions again reduce the number of components by four, so now the solution has only two independent components. For a monochromatic plane wave propagating in the z direction, these two components are

$$h_{11}^{TT} = -h_{22}^{TT} = h_+(t) \quad (2.27)$$

$$h_{12}^{TT} = h_{21}^{TT} = h_\times(t) \quad (2.28)$$

and are called the plus and cross polarizations, respectively. The effect of these polarizations on an array of test particles is a stretching and compressing of the distances between the particles in the xy -plane. This gives us a means of observing a gravitational wave: measuring the distances between two “test masses” along one axis and between two separate test masses along another axis perpendicular to first.

To determine the energy emitted by gravitational waves, we must consider a source, i.e. a non-zero energy-momentum tensor. This requires a general solution to eq. (2.24). To do so we define an *effective energy-momentum tensor* $\tau^{\mu\nu}$ that incorporates the $\mathcal{O}(h^2)$ terms such that the field equations become

$$\square \bar{h}^{\mu\nu} = \frac{8\pi G}{c^4} \tau^{\mu\nu} \quad (2.29)$$

The solution to which is

$$\bar{h}^{\mu\nu}(t, \mathbf{x}) = \frac{4G}{c^4} \int \frac{\tau^{\mu\nu}(t - \|\mathbf{x} - \mathbf{x}'\|/c, x')}{\|\mathbf{x} - \mathbf{x}'\|} d^3x'. \quad (2.30)$$

At some fixed distance r far from the zone (much greater than the GW wavelength), $\|\mathbf{x} - \mathbf{x}'\| \simeq r$, so we get

$$\bar{h}^{\mu\nu}(t, \mathbf{x}) \simeq \frac{4G}{c^4 r} \int \tau^{\mu\nu}(t - r/c, x') d^3x'. \quad (2.31)$$

Imposing the Lorenz gauge conditions on eq. (2.29) results in a set of conservation laws $\partial_\mu \tau^{\mu\nu} = 0$. These can give us an explicit expression for the spatial components of $\tau^{\mu\nu}$ in terms of its temporal component t^{00} , resulting in the following integral for the spatial components of $\bar{h}^{\mu\nu}$:

$$\bar{h}^{ij}(t, \mathbf{x}) \simeq \frac{2G}{c^4 r} \frac{\partial^2}{\partial t^2} \int x'^i x'^j \tau^{00}(t - r/c, x') d^3x' \quad (2.32)$$

$$\simeq \frac{2G}{c^4 r} \ddot{I}^{ij}(t - r/c) \quad (2.33)$$

where

$$I^{ij}(t) \equiv \int x'^i x'^j \tau^{00}(t - r/c, x') d^3x' \quad (2.34)$$

is the quadrupole tensor. The conservation laws have implicitly removed terms corresponding to the time evolution of total linear and angular momentum, in contrast to electromagnetic theory where the equivalent electric and magnetic dipole terms do not vanish.

Finally, we can once again project to the TT gauge using the projection operator $P_{ij} = \delta_{ij} - n_i n_j$, where $n^i \equiv x^i/r$ is the wave propagation unit vector, to

get

$$\bar{h}_{ij}^{TT}(t, \mathbf{x}) \simeq \frac{2G}{c^4 r} \ddot{I}_{ij}^{TT}(t - r/c) \quad (2.35)$$

$$I_{ij}^{TT}(t) = P_{ik} I^{kl} P_{lj} - \frac{1}{2} P_{ij} P_{kl} I^{kl}. \quad (2.36)$$

2.2 Sources of gravitational waves

Equations (2.35)–(2.36) show that any system whose quadrupole moment has a non-vanishing second derivative can generate GWs, which requires some non-spherically symmetric motion of masses. We can make an order-of-magnitude estimate of the GW amplitude by thinking of the quadrupole tensor in terms of the velocity of the non-spherically symmetric motion of the source (Misner et al., 1973): $\ddot{I} \sim d^2/dt^2(MR^2) \sim Mv_{\text{NS}}^2$. Then the GW amplitude is

$$h_0 \sim \frac{GMv_{\text{NS}}^2}{c^4 r}. \quad (2.37)$$

For a terrestrial, human-scale source this is incredibly small: given an object of mass $M = 1 \text{ kg}$ rotating with a tangential velocity of $v_{\text{NS}}^2 = 1 \text{ m/s}^2$, observed at a distance $r \gg c/v_{\text{NS}}^2$, the amplitude is $h \ll 10^{-53}$. Clearly much higher masses and rotational speeds are needed to produce observable GWs.

2.2.1 Compact binary mergers

Consider a binary system of massive, compact objects m_1 and m_2 (with total mass $M = m_1 + m_2$), orbiting about their common center of mass. The most compact examples are binary black hole (BBH), binary neutron star (BNS), and neutron star-black hole (NSBH) binaries. For most of its lifetime, the binary

generates continuous GWs at a frequency twice the orbital frequency ω :

$$h_+ = -\frac{4G\mu}{c^2 r} \left(\frac{v}{c}\right)^2 \cos(2\omega t) \quad (2.38)$$

$$h_\times = -\frac{4G\mu}{c^2 r} \left(\frac{v}{c}\right)^2 \sin(2\omega t) \quad (2.39)$$

where $\mu = m_1 m_2 / M$ is the reduced mass. Over time, the orbit decays due to the loss of energy to GW emission, causing the frequency and amplitude of the emission to increase as the objects spiral in towards each other. It turns out that this time-evolution scales quite dramatically:

$$\dot{f}_{\text{GW}} = \frac{96}{5} \pi^{8/3} \left(\frac{G\mathcal{M}}{c^3}\right)^{5/3} (f_{\text{GW}})^{11/3} \quad (2.40)$$

where $\mathcal{M} \equiv \mu^{3/5} M^{2/5}$. The coalescence of the two objects therefore creates a distinct GW signature, characterized by a relatively short-duration ($\lesssim 1$ s for BBHs, tens to hundreds of seconds for NSBHs and BNSs) upwards sweep in frequency (from tens to hundreds of Hertz) and amplitude, known as a *chirp* signal. Accordingly, we refer to \mathcal{M} as the *chirp mass*. The characteristic GW amplitude is:

$$h_0 = 2.6 \times 10^{-23} \left(\frac{\mathcal{M}}{M_\odot}\right)^{5/3} \left(\frac{f_{\text{GW}}}{100 \text{ Hz}}\right)^{2/3} \left(\frac{r}{100 \text{ Mpc}}\right)^{-1}. \quad (2.41)$$

As we shall see later this makes the detection of compact binary coalescences (CBCs) feasible for systems of neutron stars and stellar-mass black holes around 100 Hz. These violent merger events also happen very frequently, making them the prime candidate for detecting gravitational waves with the current generation of detectors (B. P. Abbott et al., 2020b).

Observing GW signals from compact mergers allows us to infer properties of the source components. As is evident from eq. (2.40), the rate of the frequency evolution provides information about the masses of the merging objects. Naively one might infer from eq. (2.41) that the luminosity distance can be determined directly from the observed GW amplitude. However, eqs. (2.38)–(2.39) assume a “face-on” observation of the gravitational waves. Emissions from a compact merger are not isotropic, but diminish by a factor $(1 + \cos^2 \iota)/2$, where ι is the *inclination angle* between the orbital axis of the binary and the path to the observer. This results in a degeneracy between the estimation of the source inclination angle and its distance from us, which can be resolved with independent observations by non-GW observatories, as discussed later (Section 2.3).

Furthermore, there are many source properties we cannot yet infer from eqs. (2.38)–(2.40), as they are computed in the Newtonian limit. More properties are introduced by expanding the theory to include *post-Newtonian* correction terms to the multipole expansion of the energy-momentum tensor, i.e. beyond the τ^{00} quadrupole term of eq. (2.32). The first corrections yield frequency evolution terms that capture the ratio of the masses of the binary as well as the mass-weighted effective spin parameter χ_{eff} ; combined with a measurement of \mathcal{M} we can use the mass ratio to infer the individual component masses m_1 and m_2 , although there is a degeneracy between the effects of high mass ratio and high χ_{eff} , muddying the estimation of either property. Equations (2.38)–(2.39) describe emissions from circularly-orbiting binaries; this is likely to be the case late in the evolution of most systems, since eccentric orbits will be circularized by the gravitational radiation reaction, although in extreme situations high eccentricity produces higher-order harmonics of f_{GW} as well as a shorter coalescence time.

2.2.2 Continuous wave sources

Continuous GWs generated from binary systems may range from very low frequency (nanoHertz-range) waves from supermassive black hole (BH) binaries, to milliHertz waves from stellar-mass galactic binaries, but in higher frequency bands the best candidate sources for continuous waves are isolated rapidly-rotating neutron stars (NSs) (Riles, 2017). If such an NS is non-axisymmetric, it generates GWs with a characteristic amplitude dependent on the z -axis moment of inertia, the ellipticity of the star ε , and its rotational frequency f_0 :

$$h_0 = 4.2 \times 10^{-25} \left(\frac{\varepsilon}{10^{-5}} \right) \left(\frac{I_{33}}{10^{45} \text{ g cm}^2} \right) \left(\frac{f_0}{100 \text{ Hz}} \right)^2 \left(\frac{r}{10 \text{ kpc}} \right)^{-1}. \quad (2.42)$$

These emissions would have to be much closer to be observable, but unlike CBCs, isolated NSs are much more abundant within our galaxy. Low-mass X-ray binaries, consisting of a neutron star accreting matter from a stellar companion, are another potential source of continuous GWs. Since many of these NS sources are well studied by electromagnetic astronomers, they allow for targeted GW searches that account for the known sky locations (Abbott et al., 2022).

2.2.3 Burst sources

GW bursts are short-duration events not associated with well-characterized waveforms; their time evolution is too difficult to model in a confined parameter space due to their unpredictable or poorly understood dynamical behavior. The most promising burst source to be detected are core-collapse supernovae (CCSNe), although their GW emission is still expected to be too weak for detecting events outside the galactic neighborhood, and the rate of galactic CCSNe is expected to

be only one to a few per century (Adams, Kochanek, Beacom, Vagins, & Stanek, 2013; Maoz & Badenes, 2010). Nonetheless there is evidence from electromagnetic observations that many CCSN exhibit the necessary asymmetries for GW emission.

There are many proposed scenarios for how such asymmetries could manifest, many supported by simulations (Fryer, Holz, & Hughes, 2002; Fryer & New, 2011). These simulations also face many hurdles that limit their accuracy: they have to capture the effects of general relativity, neutrino transport, and magnetic field interactions. Different models also focus on different phases of the collapse, and account for different supernova remnants (either a neutron star or a black hole). In summary, models have been formulated to predict GW emission from asymmetries in the core bounce phase due to stellar rotation or an asymmetric core; from convection processes, or bar-mode instabilities in the proto-neutron star (if one forms); from fragmentation of the core itself, or within a massive accreting disk if the remnant becomes a black hole; and from Rossby wave (r-mode) instabilities in a cooling proto-neutron star. The result is a wide range of predictions for the amplitude, frequency evolution, and duration of the gravitational waves produced by CCSN.

That said, we can still roughly estimate a characteristic GW amplitude for core-collapse emission. Sutton (2013) provides a rule of thumb for relating the energy emitted by a gravitational-wave burst E_{GW} for an isotropic emission

scenario to the root-sum-squared GW amplitude h_{rss} , which we can write as

$$h_{\text{rss}} \equiv \int_{-\infty}^{\infty} [h_+^2(t) + h_x^2(t)] dt \quad (2.43)$$

$$= \left(\frac{GE_{\text{GW}}}{\pi^2 c^3} \right)^{1/2} \frac{1}{rf_0} \quad (2.44)$$

$$\simeq 6.7 \times 10^{-20} \text{ Hz}^{-1/2} \left(\frac{10 \text{ kpc}}{r} \right) \left(\frac{100 \text{ Hz}}{f_0} \right) \left(\frac{E_{\text{GW}}}{10^{-2} M_{\odot}c^2} \right)^{1/2} \quad (2.45)$$

where f_0 is the central frequency of the GW burst. An emission energy of $10^{-2} M_{\odot}c^2$ lies on the optimistic end of expectations. Predictions for E_{GW} from core-collapse models range across a few orders of magnitude.

A number of other non-CBC emission models exist for various astrophysical objects and phenomena. For example, neutron stars with extremely strong magnetic fields, called *magnetars*, exhibit X-ray flaring behavior believed to originate from the cracking of their crusts due to magnetic field interactions, which may also produce gravitational waves by exciting oscillatory modes in the neutron star (Lasky, 2015). Other potential burst sources include pulsar timing glitches (Abadie et al., 2011), nonlinear memory effects (Ebersold & Tiwari, 2020), and cosmic string cusps (Abbott et al., 2021a).

2.2.4 Stochastic background

The superposition of all GWs forms a stochastic GW background analogous to the cosmic microwave background (CMB) (Christensen, 2018). This background is comprised of stellar-mass binary BH and NS mergers at frequencies currently observable by GW detectors, but at lower frequencies galactic white dwarf binaries and supermassive BH mergers would also contribute to the stochastic background.

At cosmological distances, relic gravitational waves from the very early universe could be detectable via their effect on the polarization of the CMB radiation.

2.3 Multi-messenger astronomy

In 2017, the first binary neutron star merger GW170817 was detected by the Advanced LIGO and Virgo detectors, immediately accompanied by the detection of a relatively low-luminosity, short gamma-ray burst GRB170817A by the space-based Fermi Gamma-ray Burst Monitor (GBM) two seconds later (Abbott et al., 2017a). The combined sky localizations of the LIGO-Virgo network and Fermi GBM prompted a world-wide follow-up campaign from observatories across the electromagnetic spectrum (Figure 1). Within a day this led to the identification of an optical counterpart near NGC 4993 that would become the first confirmed observation of a kilonova, the multi-band emission of electromagnetic waves resulting from the radioactive decay of r-process material formed and ejected in all directions by the merger.

This was a major step forward for the field of *multi-messenger astronomy*, in which joint detections between independent observational methods allow scientists to answer questions that cannot be tackled by probing just one type of signal. They can also be critical in confirming detections by observatories that have yet to detect a particular phenomenon. Before GW170817 the only multi-messenger detection of a distant astrophysical event was that of the type II supernova SN 1987A in the Large Magellanic Cloud by electromagnetic and neutrino observatories (Alekseev, Alekseeva, Krivosheina, & Volchenko, 1988; Bionta et al., 1987; Hirata et al., 1987).

There is much to be gained by using the time and sky localizations of non-GW observatories to conduct *targeted* searches for GW signals that can be

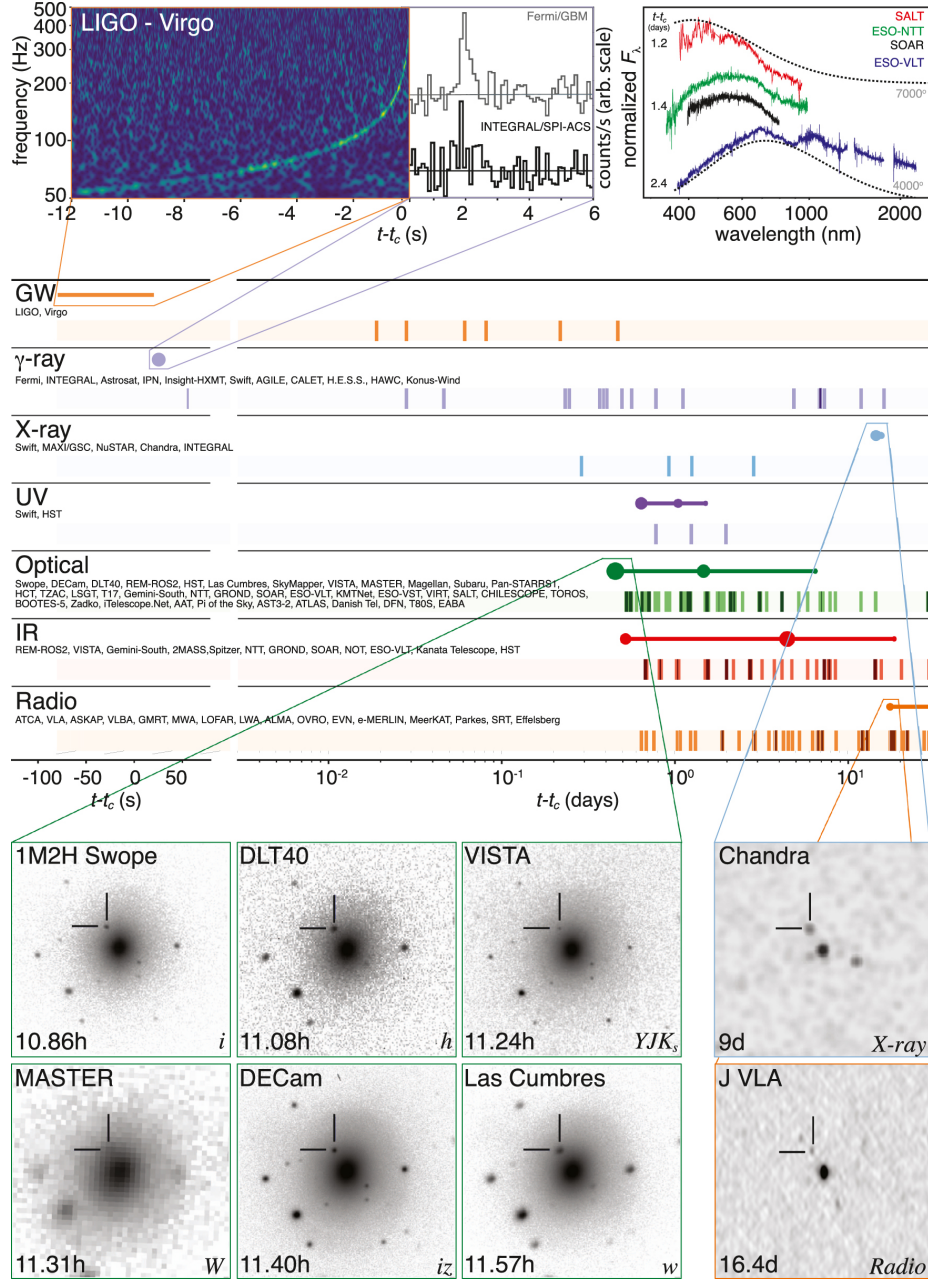


Figure 1. Timeline of the discovery of GW170817 and its electromagnetic counterparts. The vertical lines in each row represent times when information from one of the observatories listed in that row was reported to collaborators. Reproduced from Abbott et al. (2017b).

much more sensitive than the uninformed all-sky searches. Searching around the time of a known EM or neutrino counterpart already permits a much more computationally intensive analysis, since we can focus on short periods of time ranging from seconds to hours, as opposed to searching over an entire observing run. The sky localizations also allow us to “point” our GW detectors. The delay in the time-of-arrival of a GW signal at two or more detectors is dependent on its direction of propagation, so we can specifically search for signals matching the expected delay based on the known sky location of the source. Furthermore, the response of an interferometer to GWs is not isotropic, but instead is strongest along its z -axis and weakest along its xy -plane. This “antenna response” can be used to combine the data streams of multiple interferometers in a way that maximizes sensitivity to a specific sky location.

Although there are many possible associations between GWs and other types of signals, the association with GRBs has already been confirmed and will likely continue to be a dominant avenue for multi-messenger detections involving the LIGO detectors. Distance measurements of GRBs (*Swift GRB Archive*, 2022) place most well beyond LIGO’s range, so golden events like GW170817 may not be so common among joint detections. There could therefore be GWs detectable only through targeted searches.

2.4 GWs associated with GRBs

GRBs are energetic bursts of gamma rays in the MeV range, first discovered in 1967 (Klebesadel, Strong, & Olson, 1973). It is believed that the ultra-relativistic jets required to produce GRBs can come from black holes (Woosley, 1993) or magnetars (Dai & Lu, 1998), as they can possess the energy required

to act as *central engines* (Kumar & Zhang, 2015). If the accretion rate around a black hole is sufficiently high, a large amount of neutrinos and anti-neutrinos are emitted as the accretion disk cools. Pair annihilation of these particles results a “fireball” of photons and electrons-positron pairs, as well as protons accelerated by neutrinos (Chen & Beloborodov, 2007). Alternatively, the angular momentum of a rapidly spinning black hole can be extracted by a strong accretion disk magnetic field to create the jet, a process known as the Blanford-Znajek mechanism (Blandford & Znajek, 1977; Lee, Wijers, & Brown, 2000). This process likewise believed to be responsible for jets produced by *millisecond* magnetars, which have rotation periods of ~ 1 ms (Metzger, Giannios, Thompson, Bucciantini, & Quataert, 2011).

Whether the central engine is produced from a core-collapsing star or a merger involving a neutron star, the jet has to propagate through the surrounding material left behind by the progenitor, which is mostly distributed in the plane perpendicular to the central axis (the rotational axis of the star or orbital axis of the merger). This results in the jet being collimated, emerging from the envelope as a narrow, bipolar beam along the central axis.

Once the jet has emerged, its kinetic energy must be converted into gamma-rays. The internal shock model is widely accepted as the mechanism for producing the initial *prompt emission* (Rees & Meszaros, 1994). In this model, the jet is treated as a series of shells emerging at different speeds. When the shells collide, their kinetic energy is converted to thermal energy, and gamma-ray photons are produced via either synchrotron radiation or inverse-Compton scattering. At greater distances, the external shock model proposes that the shells eventually coalesce into a single shell that collides with the circum-burst medium (Blandford

& McKee, 1976). Again kinetic energy is converted into thermal energy, this time radiating photons in the X-ray, visible, and radio bands in addition to gamma-rays. This phenomenon is referred to as the GRB *afterglow* and can last days after the prompt emission. Observation of afterglows is crucial to localizing the GRBs and identifying source galaxies and measuring redshifts.

GRBs vary widely in their temporal and spectral properties, but there is a bimodality in the distribution that has led to them being classified as either short/hard or long/soft (Kouveliotou et al., 1993). GRB durations are defined based on their T_{90} , the time interval over which 90% of the total background-subtracted photon counts are observed by the reporting GRB detector. Spectral hardness is described using the ratio of the flux density in the 50–300 keV band to the flux density in the 10–50 keV band, therefore representing the abundance of high energy photons (von Kienlin et al., 2020). GRBs with $T_{90} \lesssim 2$ s and hard emission spectra are classified as short, while long bursts last $\gtrsim 2$ s and have soft emission spectra (Figure 2). Photometry and spectroscopy data have provided evidence that long GRBs originate from the deaths of massive stars, whereas short GRBs are believed to be associated with compact binary mergers involving neutron stars, like GW170817.

2.4.1 Short gamma-ray bursts

In a compact binary merger, a viable central engine is produced once an neutron star has coalesced with a black hole or another neutron star, leaving behind either a more massive black hole or a hypermassive neutron star (Eichler, Livio, Piran, & Schramm, 1989; Nakar, 2007). Material stripped from the neutron star(s) by *tidal disruption* forms an accretion disk around the central engine, fueling

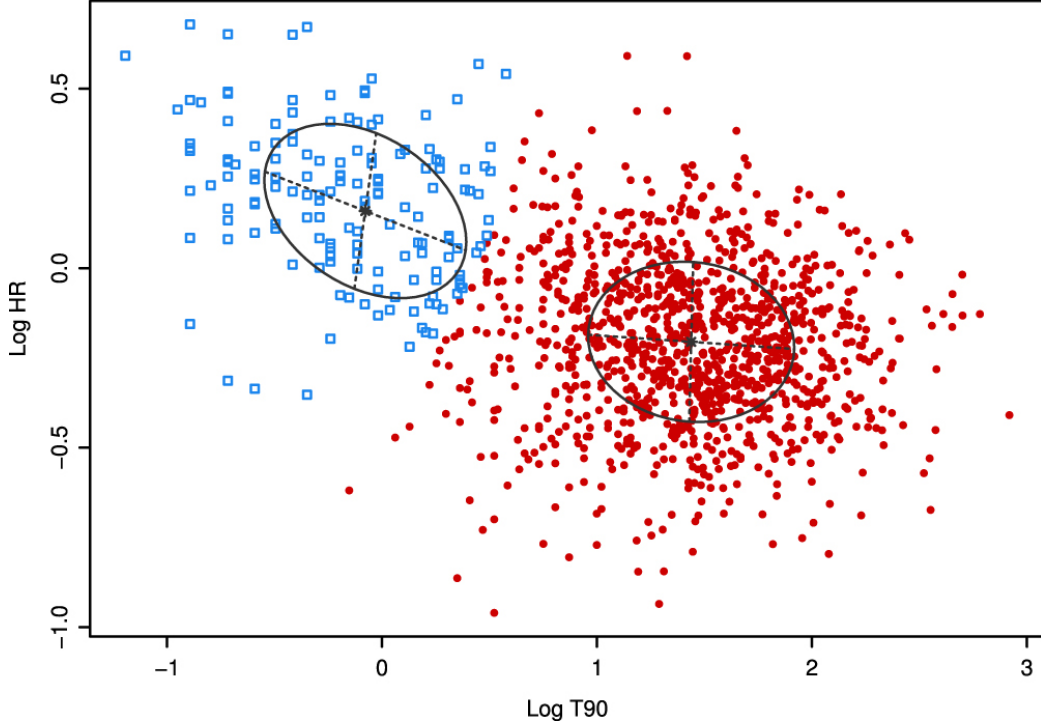


Figure 2. Hardness ratios (HR) vs. T_{90} s of Fermi GRBs, showing the distinction between short and long bursts. Reproduced from Bhat et al. (2016)

the emission of a GRB. The mass of the disk would only be a fraction of a solar mass, since neutron stars are themselves are only $\sim 1.4 M_\odot$, resulting in a short window for engine activity before accretion subsides and the fuel is spent.

A lot can be learned from joint observations of short GRBs and their GW counterparts. GW parameter estimation suffers from a degeneracy between distance and orbital plane inclination; increasing the distance of the merger and orienting its orbital plane would both result in a lower GW amplitude. This degeneracy can be broken if either one could be measured externally. If the joint detection localization were good enough to determine a host galaxy, this would greatly help resolve the distance, however this will more likely require observation of an optical or ultraviolet counterpart due to the poor localization provided by current GRB and GW detectors. In the case of GW170817, the host galaxy whose redshift was

known was used to determine the distance, which then allowed for a more precise measurement of the inclination angle.

A separate analysis using the distance measured from the GW detection combined with the known redshift made the first joint GW-EM measurement of the Hubble constant, albeit with very large uncertainty due to the small sample size, of $H_0 = (70.3 \pm 5.0) \text{ km s}^{-1} \text{ Mpc}^{-1}$ (Abbott et al., 2017). The Hubble constant, which describes the rate of the expansion of the universe, has been measured in other ways. The Planck collaboration measured the Hubble constant based on CMB data to be $H_0 = (67.4 \pm 0.5) \text{ km s}^{-1} \text{ Mpc}^{-1}$ (Planck Collaboration et al., 2020), which disagrees with the SH0ES team measurement of $H_0 = (73.04 \pm 1.04) \text{ km s}^{-1} \text{ Mpc}^{-1}$, drawn from observations of Cepheid variables in Type Ia supernova host galaxies, to 5σ (Riess et al., 2021). Although the LIGO-Virgo result from GW170817 alone does not disfavor either side of the issue, GW detectors could play a major role in resolving this tension as we detect more binary neutron star mergers in the future.

One of the many unanswered questions surrounding GRBs pertains to their jet profile, the luminosity as a function of viewing angle (the angle between the observer and the symmetric axis of the jet; the profile is assumed to be axially symmetric and independent of distance). When information about the jet profile is required, e.g. for making rate estimates for GRB detections, the profile is historically modeled as a top-hat (uniform within some opening angle and dropping sharply beyond it) for simplicity, but the true profile may be different.

Determining the viewing angle θ_{obs} of a GRB is essential for distinguishing between different jet profile models, but it relies on the ability to observe an afterglow emission. Afterglow emissions exhibit a signature *jet break* in the their light curves, resulting from the slowing down of the jet as it sweeps up

matter in its path. An abrupt decline in on-axis luminosity is observed as the relativistic beaming of the jet diminishes. The timing of this jet break can be used to determine the opening angle of the jet, although few jet breaks have been observed for short GRBs, so existing EM observations do not place tight constraints (Biscoveanu, Thrane, & Vitale, 2020).

Joint GW-GRB observations can provide much more information on jet properties (Farah et al., 2020; Mogushi, Cavaglià, & Siellez, 2019). GRB170817 was orders of magnitude less energetic than most short GRBs, so it likely would have been ignored in the absence of a GW coincidence. Its low luminosity immediately ruled out an on-axis top-hat jet. An off-axis top-hat jet was considered unlikely as well because the narrow opening angle predicted for top-hat jets based on theory and past GRB measurements only allowed for $\theta_{\text{obs}} \lesssim 10$ deg. More evidence against an off-axis top-hat model arose when the bright afterglow expected to emerge after ~ 1 day was not observed. These observations instead favored a wide-angled, structured jet model for GRB170817. A structured jet model may refer to any luminosity function that decreases gradually with θ_{obs} rather than abruptly, e.g. a Gaussian or power-law with uniform center. One mechanism that would explain such a model is a *cocoon* emission, in which the relativistic jet interacts dissipatively with the surrounding merger ejecta, depositing its energy into a cocoon fireball that results in a structured jet (Abbott et al., 2017).

The connection between GWs and short GRBs may extend beyond binary neutron star systems like GW170817. Some NSBH mergers may be capable of producing GRBs in the right conditions. The neutron star could be tidally disrupted if the mass ratio between the black hole and the neutron star is not too unequal, due to a low black hole mass, and the black hole has a high prograde spin.

These conditions would produce a short GRB in much the same way as in a BNS merger. However, estimates of the accretion disk mass are highly uncertain, being heavily dependent on the neutron star equation of state, so it is unknown what fraction of NSBH are truly capable of GRB emissions.

2.4.2 Long gamma-ray bursts

Long GRBs are believed to come from the core collapse of massive stars, which as discussed above have many models predicting GW emission. The majority (about 70%) of GRBs are long GRBs, so although the expected GW amplitudes are quite weak they present an abundance of electromagnetic sources that each hold the potential of a GW counterpart. Since these events could also emit high energy neutrinos, they hold the potential of a triple-messenger detection in which GWs, EM waves, and neutrinos are all observed from the same source.

Some models predict GW emission would occur as a result of asymmetries in the core-collapse phase. Such GWs would be short, lasting less than a second. Extreme emission models predict a wide variety of signals, often longer in duration. Matter surrounding the core-collapse remnant forms an accretion disk, in which turbulent behavior can arise. For instance, instabilities in the thick outer regions of the accretion disk can lead to the formation of a gravitationally bound clump of matter. If the clump is cooled quickly enough (on a time scale less than its orbital period about the central BH), instead of returning to stability it can collapse to form a low-mass NS. This NS would then migrate inwards, shedding angular momentum in the form of GWs similar to an NSBH merger (Piro & Pfahl, 2007).

The characteristic strain amplitude for this mechanism is

$$h_0 = 6.4 \times 10^{-24} \left(\frac{\mathcal{M}}{M_\odot} \right)^{5/3} \left(\frac{f_{\text{GW}}}{100 \text{ Hz}} \right)^{2/3} \left(\frac{r}{100 \text{ Mpc}} \right)^{-1}. \quad (2.46)$$

Radiative cooling is too slow in the thick outer disk, but the high temperature and density of the accretion environment allows nuclear processes to provide sufficient cooling. The disk fragments are eventually torn apart by tidal disruption as they get too close to the central black hole, placing a maximum limit on the duration of potential GW emissions for this scenario of about 1 s.

In an even more extreme scenario, instabilities can arise in a magnetized, thick accretion “torus” that is strongly coupled to the central BH via magnetohydrodynamic effects (M. H. van Putten, 2001; van Putten et al., 2004). These instabilities can form quadrupole mass moments in the torus that emit GWs of energy

$$E_{\text{GW}} = 0.2 M_\odot \left(\frac{\eta}{0.1} \right) \left(\frac{M_{\text{BH}}}{7 M_\odot} \right) \quad (2.47)$$

where η is the ratio of the torus angular velocity to that of the black hole, which has mass M_{BH} .

Accretion disk instability models are particularly interesting due to their potential connection to X-ray flares. Many GRBs exhibit a diverse range of X-ray flaring behavior that could be attributed to disk fragments falling in at different times after the formation of the central black hole (Dall’Osso, Perna, Tanaka, & Margutti, 2017; Perna, Armitage, & Zhang, 2006).

A fraction of long GRBs could even originate from compact mergers: some short GRBs have been observed to exhibit extended emissions that can last much longer than the initial short GRB impulse (Norris & Bonnell, 2006;

M. H. P. M. van Putten, Lee, Della Valle, Amati, & Levinson, 2014). These, too, may be associated with X-ray flaring, as accretion disks formed around NSBH mergers could likewise produce infalling clumps (Mu et al., 2018). A recent observation of a kilonova counterpart to the long-duration GRB 211211A at 350 Mpc is believed to have originated from a BNS merger (Rastinejad et al., 2022). Based on this observation and the number of nearby long GRBs not accompanied by a supernova, at least 10% of long GRBs could arise from mergers. These scenarios and observations raise questions about the simplistic short/long classification of GRBs.

CHAPTER III

GRAVITATIONAL WAVE DETECTORS

Detection of gravitational waves requires measuring the transverse stretching and compressing of space. The earliest attempt at this was done through resonant mass detectors, solid, vibrationally isolated cylinders tuned to a particular frequency that could be used to detect the effect of gravitational waves on the length of the cylinders (Weber, 1968). These proved incapable of reaching the required sensitivity for detecting even the strongest gravitational waves in the frequency band they were designed for ($\sim 1 \text{ kHz}$).

The current era of GW detection is dominated by laser interferometers inspired by the simple Michelson interferometer. There are currently three observatories in operation: LIGO Hanford Observatory (LHO) in Washington, LIGO Livingston Observatory (LLO) in Louisiana, and the Virgo observatory in Italy. Additional detectors in Japan (KAGRA) and India (LIGO India) are under construction, and projects for next-generation detectors (Einstein Telescope, Cosmic Explorer, and Laser Interferometer Space Antenna (LISA)) are on the horizon.

3.1 GW interferometry

To understand how an interferometer detects gravitational waves, consider a simple Michelson interferometer with arm lengths L_x and L_y . The interferometer measures the difference in the changes of its arm lengths, $\Delta L = \Delta L_x - \Delta L_y$, by splitting a laser beam down each arm via a beam splitter placed at the vertex, having the light reflected back by a mirror (called a *test mass*) at the end of each arm, and producing an interference pattern when the beams reunite. Differential

changes in arm length manifest as phase shifts in the output. In a LIGO detector, a photodetector is placed at the anti-symmetric output port (the output not leading back to the laser source). The detector is tuned (by the choice of arm length) to operate at its dark fringe, i.e. the photodetector observes no signal due to destructive interference. If one interferometer arm is elongated relative to the other, the phase shift between the signals from both arms results in some constructive interference; thus the amplitude of a gravitational wave passing through the plane of the detector arms is converted to an amplitude in laser light measured at the output port.

A gravitational wave passing through the instrument induces a *strain* $h = \Delta L/L$. Our ability to measure gravitational waves therefore depends on how precisely we can measure ΔL and the length of the interferometer arms. The photodiode measurement is ultimately limited by *shot noise*, the random fluctuations in the number of photons observed. This is a Poisson process, so the fluctuations scale with the square root of the photon count N_{photon} , which itself is dependent on the laser power and wavelength and the frequency of the GW signal we are searching for:

$$N_{\text{photon}} \sim \frac{P_{\text{laser}} \lambda_{\text{laser}}}{hc f_{\text{GW}}} \quad (3.1)$$

The minimum detectable differential arm length change for a photodiode limited by shot noise is

$$\Delta L \sim \frac{N_{\text{photon}}^{1/2} \lambda_{\text{laser}}}{N_{\text{photon}}} = \sqrt{\frac{hc \lambda_{\text{laser}} f_{\text{GW}}}{P_{\text{laser}}}} \quad (3.2)$$

which gives a minimum detectable strain, for a 4-km interferometer with a 1-W, 1- μm infrared laser observing 300-Hz gravitational waves, of $h \sim 10^{-17}$. This is

impressive but orders of magnitude away from being able to observe at high signal-to-noise ratio (SNR) the GW sources discussed in the previous chapter ($h \lesssim 10^{-20}$).

We can also extend the interferometer, but to get an order of magnitude improvement requires an order of magnitude extension of the arms, which is not entirely practical. Instead, we can increase the *effective arm length* by designing the arms as Fabry-Pérot cavities, forcing the light in the arms to bounce back and forth many times before returning to the beam splitter, as shown in Figure 3. This works as long as the light does not spend an amount of time comparable to the passing of a full gravitational wavelength, so the effective arm length should not exceed $L_{\text{eff}} \sim \lambda_{\text{GW}}$. For signals in the hundreds of Hertz, this limits the effective arm length to a few hundred kilometers, or a few hundred round trips for a LIGO detector. Nevertheless, combined with the optimal photodiode above, this setup can detect a strain of $h \sim 10^{-20}$. We will see in the following discussion of the Advanced LIGO (aLIGO) design how we can extend our sensitivity even further.

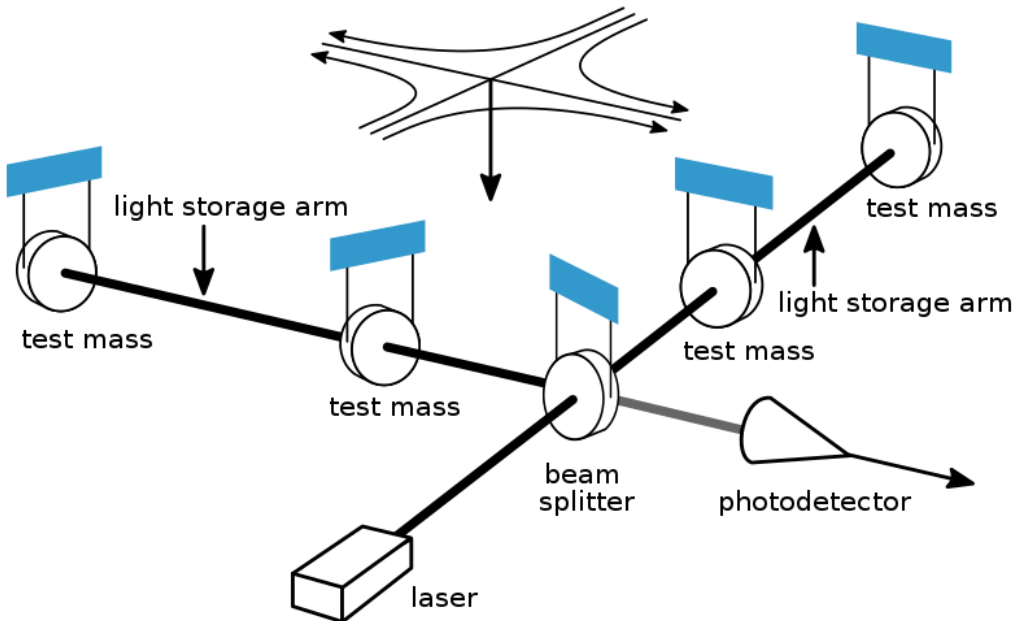


Figure 3. Layout of a Michelson interferometer with Fabry-Pérot arm cavities.

3.2 Advanced LIGO

The LIGO detectors completed the transition to their current aLIGO design stage in 2015, and began first observing run (O1) on September 12 that year, making the first detection of a GW from a BBH merger on September 14 (B. P. Abbott et al., 2016b). This was followed by two more BBH detections before the end of the run on January 16, 2016 (Abbott et al., 2019). O2 started on November 30, 2016 after a period of detector upgrades and ended on August 25, 2017. During that run, in addition to several more BBH detections, the LIGO network (with the addition of the Virgo detector in Italy towards the end of the run) observed the first BNS merger on August 17, 2017 (Abbott et al., 2017a). O3, which spanned April 1, 2019 to March 27, 2020, came after another round of major improvements in the performance of the detectors (Buikema et al., 2020) and the full inclusion of the Virgo detector in the GW network. By the end of O3, the LIGO and Virgo detectors had observed an all-time total of 90 GW events (Abbott et al., 2021b, 2021c).

The performance of the LIGO detectors can be assessed in terms of its astrophysical range and its duty cycle. The range is the distance at which a detector can observe a given GW source; in O3, LHO and LLO had binary neutron star inspiral ranges of about 111 Mpc and 134 Mpc, respectively. Their duty cycles, the percentage of time each was in science observation mode, were 75% and 77%, with a joint-observing duty cycle of 62%.

A number of technological advances building on top of the basic Fabry-Pérot interferometer design have been necessary to achieve this incredible sensitivity (Aasi et al., 2015). Increasing laser power and injecting squeezed light reduces the effects of shot noise. A power recycling cavity at the symmetric output

sends the constructively-interfering light leaving in that direction back into the interferometer (essentially increasing laser power). A signal recycling cavity at the anti-symmetric output is used to modify the shape of the detector response function, effectively tuning it to be more sensitive to a specific frequency band.

We now walk through the full journey on which the interferometer laser embarks, giving names to the various components of the aLIGO detector as these will be relevant in later discussions of detector noise and instrumentation. A detailed optical layout is shown in Figure 4.

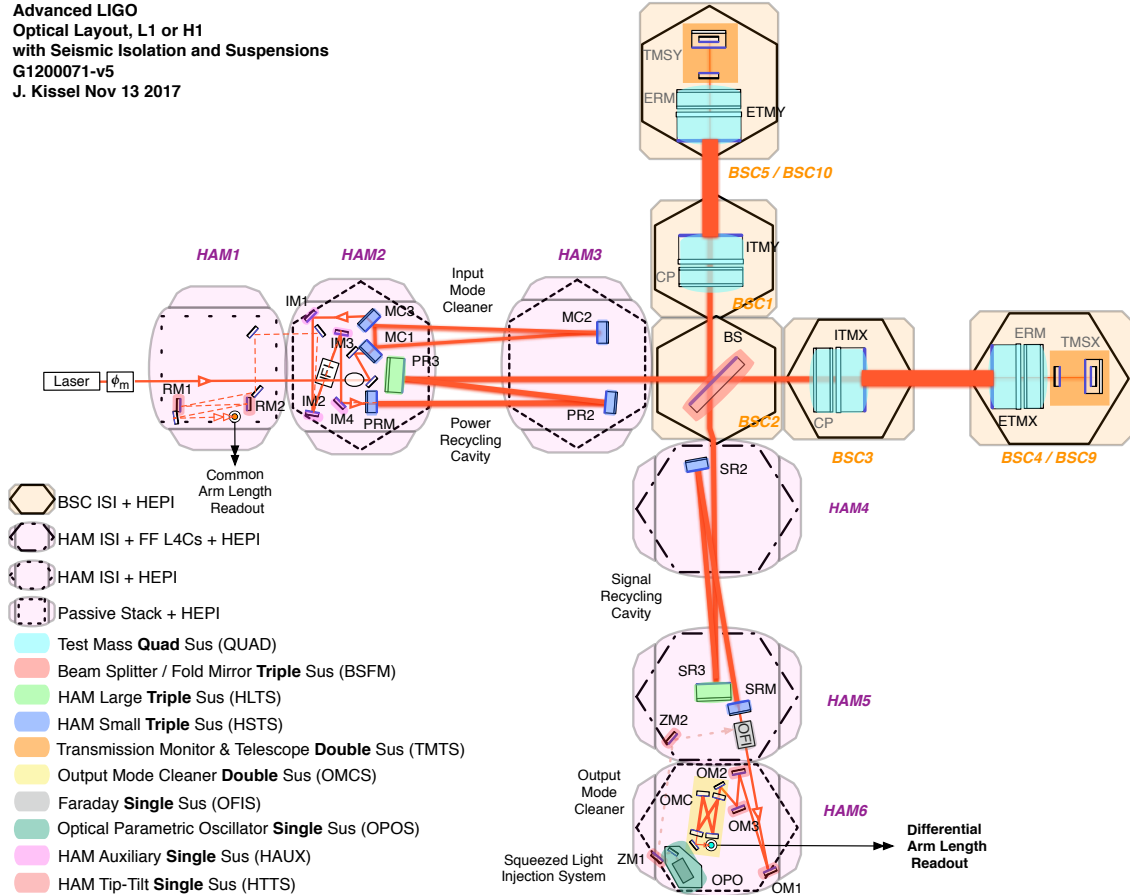


Figure 4. Full optical layout of an Advanced LIGO interferometer (Kissel, 2017).

The laser is produced at the start of the *input arm*. In O3, this pre-stabilized laser (PSL) is a 1064 nm infrared source amplified to 70 W before entering the main beam tube of the interferometer, where it then passes through an input mode cleaner (IMC) optical cavity that filters out higher-order spatial beam modes. The IMC optics are located inside two vacuum chambers called horizontal access modules (HAMs) (namely HAM2 and HAM3) spanning the mode cleaner tube, which comprises the majority of the input arm length. As it reaches the interferometer vertex, the beam is split into two by the beam splitter. In each arm, it passes through an input test mass (ITM), beyond which it has entered a 4-km-long Fabry-Pérot cavity. The beams now leave the *corner station* en route to the *end stations* (End-X and End-Y) where the end test masss (ETMs) are housed. Between the ITMs and ETMs the laser bounces some 300 times before returning to the beam splitter.

The carrier light exits along the input arm and enters the power recycling cavity, whose optics are located in the same HAM chambers as the IMC optics. In the *output arm*, the signal recycling cavity (in HAM4 and HAM5) extracts the GW signal from the exiting signal sidebands, transmitting them to the output mode clearer (OMC) in HAM6 which again filters out higher-order modes. This is also where a squeezed vacuum state is injected into the interferometer light to reduce shot noise. Finally, the output photodiode in HAM6 receives the signal light, which is converted by the calibration system into a measurement of ΔL , referred to as differential arm length measurement (DARM). From that we compute the strain $h = \Delta L / 4000$ m.

3.3 Noise sources

We have seen that photon shot noise limits the sensitivity of any GW interferometer, and is reduced by using a high-power input laser. However, increasing laser power brings up a second noise source, similarly associated with the quantum mechanical behavior of light. The force of the laser light hitting the test masses causes fluctuations in the test mass positions, referred to as *radiation pressure noise*. These random displacements similarly limit the sensitivity, although in contrast with shot noise they fall off with the GW frequency. Radiation pressure is addressed by increasing the size of the test masses themselves (40 kg in the aLIGO detectors).

In addition to the quantum mechanical limitations of shot noise and radiation pressure noise, there are a plethora of noise sources not intrinsic to the design of an interferometer. Figure 5 is the *noise budget* of the LHO and LLO detectors. It shows measurements and estimates of all known noise sources affecting both LIGO detectors at the end of O3, including those presented in this dissertation (scattered light and input beam jitter). Each detector is fitted with thousands of auxiliary instruments for monitoring the internal and external state of the interferometer. For sources whose effects are well understood this allows estimates to be made of their contributions to the overall DARM sensitivity. Still, some sources are unknown: note that in the few tens of Hertz at either detector there is a significant discrepancy between the sum of known noises and the measured noise. Constant study of the interferometers is necessary to identify new noise effects so that performance improvements can be made.

At low frequencies there is *seismic noise*, which comes from ground motion caused by seismic and human activity. The core optics must be suspended on

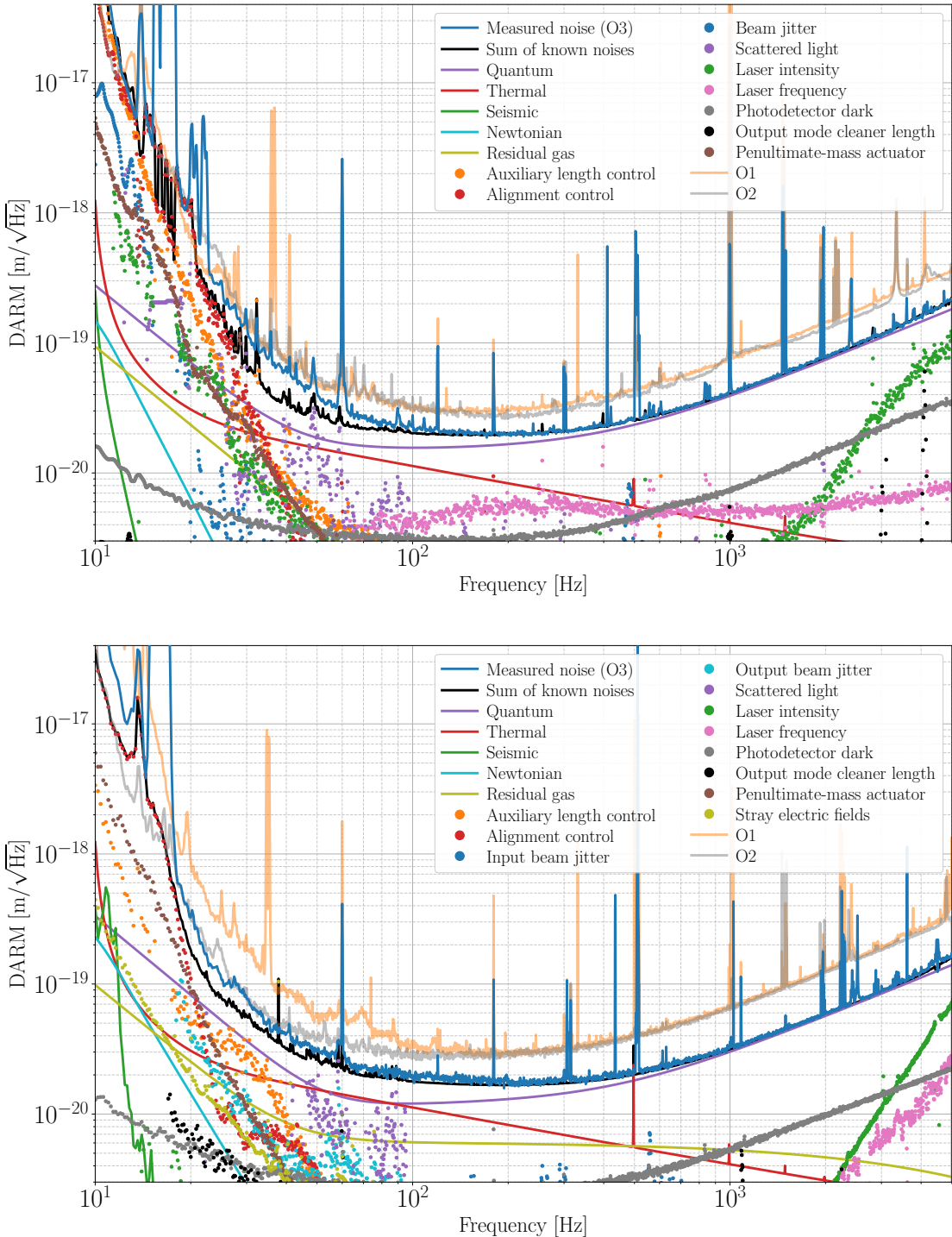


Figure 5. Full noise budgets of the LIGO Hanford (top) and Livingston (bottom) observatories at the end of the third observing run. Quantum noise refers to both shot noise and radiation pressure noise. Reproduced from Buikema et al. (2020).

multi-stage isolation systems to dampen these movements; otherwise they would completely swamp out the tiny fluctuations induced by gravitational waves. The transfer function of a pendulum, derived by taking the Fourier transform of the simple pendulum equation of motion, describes the attenuation of motion it provides:

$$A(f) = \frac{1}{1 - (f/f_{\text{pend}})^2} \quad (3.3)$$

where $f_{\text{pend}} \equiv \sqrt{g/l}/(2\pi)$ is its natural frequency. Designing a pendulum with low f_{pend} , i.e. a long one, allows substantial attenuation above that frequency, but it can be physically impractical to go too long. Rather, stacking multiple pendulums each with a low enough $f_{\text{pend}} \lesssim 1 \text{ Hz}$, each providing a $\propto f^{-2}$ attenuation, results in much better damping in the tens of Hertz. This construction suppresses the contribution of seismic noise to orders of magnitude below that of other noise sources, except at the very low frequencies $f \lesssim f_{\text{pend}}$ outside of the LIGO detection band.

Brownian motion of molecules in the test masses themselves results in *thermal noise*, which is dependent on the temperature of the optics. Thermal noise excites the internal vibrational modes of the test masses, as well as the “violin” modes of the glass fiber suspensions that make up the final pendulum stage. These modes have very high Q-factors, resulting in the very loud, narrow lines at their resonances ($\sim 500 \text{ Hz}$).

Scattered light noise occurs when the laser beam reflecting off the beam spot on a test mass or other optic ends up hitting surfaces that are moving relative to the optic, like vacuum chamber walls. A very small fraction of the light reaching the moving surface is reflected to the originating or another beam spot, where it scatters back into the main interferometer beam. When the distance to the moving

surface is modulated by vibrations, the phase of the returning light changes relative to the main beam, producing fluctuations in the amplitude of the beam, that, at just 1 part in 10^{20} can be on the scale of those produced by gravitational waves. In addition to this sensitivity to recombined scattered light, the scattering noise is problematic because of non-linear coupling when the path length modulation becomes comparable to the wavelength of the light, producing noise at harmonics of modulation frequencies (Soni et al., 2020).

The input laser system can itself be a source of *beam jitter noise*. Alignment fluctuations in the beam, called jitter, cause variations in the coupling of the fundamental optical mode to the arm cavities (Hardwick, 2019; Mueller, 2005). In principle the symmetry of the interferometer arms should reject the effects of jitter, but defects in the test masses can break this symmetry, resulting in significant noise at the jitter frequencies, which are typically associated with mechanical resonances of optic mounts the input laser table.

All of the above represent mechanical influences on the strain measurement. However, even oscillating magnetic fields can affect components of the detector, causing *magnetic field noise*. The fields can couple by directly affecting permanent magnets on or near the test masses. In Initial LIGO, permanent magnets were placed on the test mass suspensions as well as on the test masses themselves; the test mass ones were removed prior to LIGO, so only the magnets on the suspension systems remain. The suspension system suppresses permanent magnet displacement $\propto f^{-2}$, so it is only likely to dominate at low frequencies. At higher frequencies, magnetic noise is dominated by the induction of currents in the various cables and connectors that are part of the interferometer control system. These effects may

be unpredictable: changes to electronic hardware are made frequently, each time potentially introducing a new source of noise or modifying an existing one.

There are still many noise sources shown in the noise budget that are beyond the scope of this dissertation. The noise investigations carried out through the duration of this PhD mainly covered noise effects associated with external vibrations and magnetic fields. For the sake of brevity we will stop here and turn our focus towards methods used to perform these investigations.

CHAPTER IV

METHODS FOR STUDYING ENVIRONMENTAL NOISE

Environmental noise refers to any signal originating from outside the structure of a GW detector that can impact the detector's sensitivity or disrupt its ability to achieve and maintain lock (Effler et al., 2015; Nguyen et al., 2021). Some of the most problematic environmental influences were introduced in Section 3.3. Their effects on detector sensitivity can range from persistent excess noise in the GW strain data, to short-duration transient signals, or *glitches*.

One goal of studying environmental noise is to directly aid in the validation of GW events. Due to the sophisticated nature of the search pipelines used to detect gravitational waves in the LIGO data, environmental glitches are highly unlikely to fully account for a GW event candidate. However, glitches capable of influencing analyses occur frequently at both observatories.

Unlike instrumental noise, environmental noise can potentially be correlated between different detectors, i.e. stemming from a common source as opposed to stemming from chance coincidence. For example a sufficiently strong lightning strike can produce magnetic field noise in both LIGO detectors. Such correlated noise is not accounted for in the estimation of false-alarm probabilities, which is done by time-shifting background data from each LIGO detector to generate long stretches of artificial joint-observing data under the assumption that the backgrounds are non-correlated.

Environmental noise is particularly important in searches for unmodeled sources of gravitational waves, as these look for excess power without the use of waveform templates. Even for highly significant CBC events, contamination of the strain data can bias parameter estimation analyses that infer source properties from

the morphology of the event. Thus it is critical that we have a quantitative solution for identifying and evaluating the impact of environmental transients when they coincide with candidate events.

The second goal is to improve the sensitivity and performance of the detector by localizing noise sources and coupling mechanisms. Once tracked down, coupling can be mitigated in three ways: eliminating the noise source, attenuating the propagation of the signal, or modifying the detector itself.

In this chapter I describe the hardware used to monitor environmental noise sources (Section 4.1) and to reproduce them experimentally (Section 4.2). I present a method for quantifying environmental coupling (Section 4.3), then I discuss the limitations (Section 4.4) and software implementation (Section 4.5) of the method.

4.1 The PEM sensor array

Understanding environmental influences on the detectors requires comprehensive monitoring of its physical surroundings. This is done through the physical environmental monitoring (PEM) system of auxiliary sensors (Figure 6), which consists of accelerometers for high-frequency vibrations (between tens to thousands of Hertz), seismometers for low-frequency vibrations (up to tens of Hertz), microphones, magnetometers, voltage monitors that measure the voltage of electric power supplied to the detector sites, radio-frequency (RF) receivers, a cosmic-ray detector for high-energy particles, and wind, temperature and humidity sensors. Detailed information on PEM sensors, including example background spectra and calibration data, can be found on the PEM website, PEM.LIGO.org (R. Schofield, Effler, Nguyen, et al., 2021).

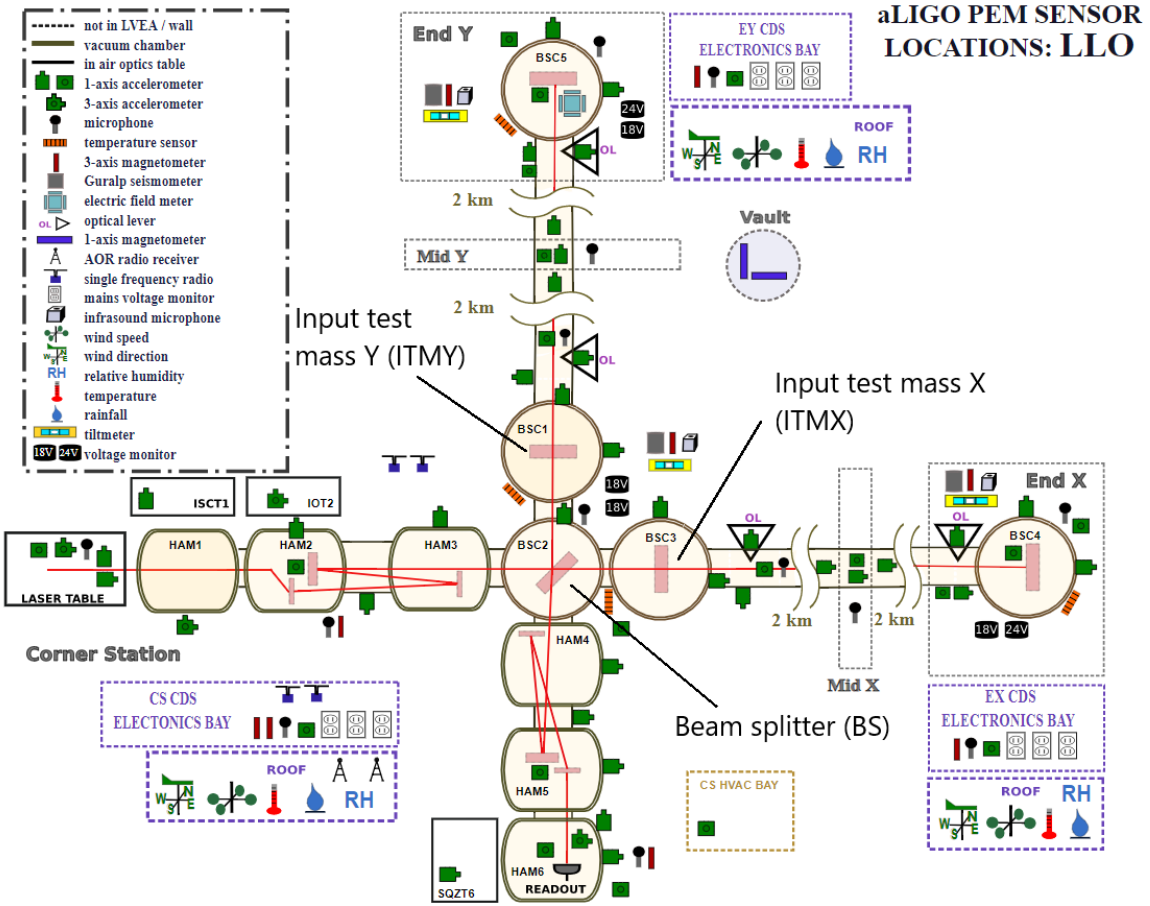


Figure 6. The PEM system layout at LLO during O3, as seen on the PEM public website.

Most sensors produce an analog signal that is converted to a digital signal via an analog-to-digital converter (ADC), then processed by a data acquisition system and saved into frame files. The frame file are the primary data format for GW detector data (Blackburn et al., 2019) and are remotely accessible via the LIGO grid computing clusters located at the observatories as well as various LIGO-affiliated institutions. From here on, I will use *sensor* to refer to the physical monitoring device and *channel* to refer to the data stream as read from frame files.

4.1.1 Monitoring the monitors with `ligocam`

Maintaining an extensive, ever-expanding array of auxiliary sensors requires a scalable solution for monitoring their behavior. Frequent changes to the sensors, as well as of interferometer hardware, result in changes in ambient spectral characteristics. Worse yet, sensors, their power supplies, their ADCs, and the data acquisition system that process their signals all have the potential to malfunction, leaving blind spots in our ability to detect signals that may affect the GW strain data.

The LIGO channel activity monitor, or `ligocam`, is a program that checks for various signs of unusual sensor behavior using a number of spectral cues (Taluker, Nguyen, et al., 2021). The goal of `ligocam` is to produce human-readable summaries of sensor behavior for the entire PEM network at an observatory, and send email alerts to experts when significant malfunctions are identified.

Leveraging the LIGO data grid computing clusters, `ligocam` parallelizes its analysis by splitting the full channel list (over 100 channels and potentially increasing in future runs), processing only five per job. This allows it to run hourly, scheduled by a `cron` job, outputting a summary page and transmitting email alerts (if applicable) within minutes. A `cron` job is scheduled at each of the LIGO observatories. Although such expediency is not necessary for fixing malfunctioning hardware, it is important to have up-to-date channel status when validating recently detected GW event candidates, as discussed in Section 5.4.

The program reads in time series data using the `gwpy` library (Macleod et al., 2021) and converts each time series to an amplitude spectral density (ASD). When run for the first time, `ligocam` saves the current ASDs as reference ASDs.

On each subsequent run at a later time t , the new ASD $X_t(f)$ is compared to the reference $\bar{X}_{t-1}(f)$ to determine if there is anomalous behavior present. If $X_t(f)$, shows no anomalous behavior relative to $\bar{X}_{t-1}(f)$, then the reference is updated as an exponential average of all past non-anomalous ASDs:

$$\bar{X}_t(f) = \begin{cases} X_0(f), & t = 0 \\ \alpha X_t(f) + (1 - \alpha) \cdot \bar{X}_{t-1}(f), & t > 0 \end{cases} \quad (4.1)$$

where α^{-1} is the averaging decay length. If `ligocam` is run hourly with $\alpha^{-1} = 1/6$, for instance, then $\bar{X}_t(f)$ is roughly the average of the past six hours of channel data. If any anomalous behavior is detected, it is reported on the output HTML page and (if sufficiently egregious) via email to the relevant parties, and $\bar{X}_t(f)$ is not updated.

Anomalies are identified and reported in a number of ways. Noise far above or below the reference is a sign of changes to hardware or infrastructure in the vicinity of the sensor, which may not adversely affect coverage of the area but could adversely affect noise estimates as described in Section 5.4. If $X_t(f)$ is many orders of magnitude below the reference but still above the electronic noise background of the ADC, the sensor is considered to be faulty. Some sensors, especially magnetometers, can have background noise levels low enough to be near the ADC noise floor. For this reason, `ligocam` checks for magnetometers are performed specifically on the 60 Hz mains signal, while other sensors (accelerometers, microphones, etc.) are analyzed for broadband variations. If the signal is even weaker than the electronic noise background, then the data acquisition system is blamed for the failure.

Leading up to O3, ligocam was also redesigned for improved user and developer accessibility, including organizing the various thresholds and options for customizing the reporting of anomalous spectra into a single configuration file for each observatory and subsystem.

4.2 Environmental noise injections

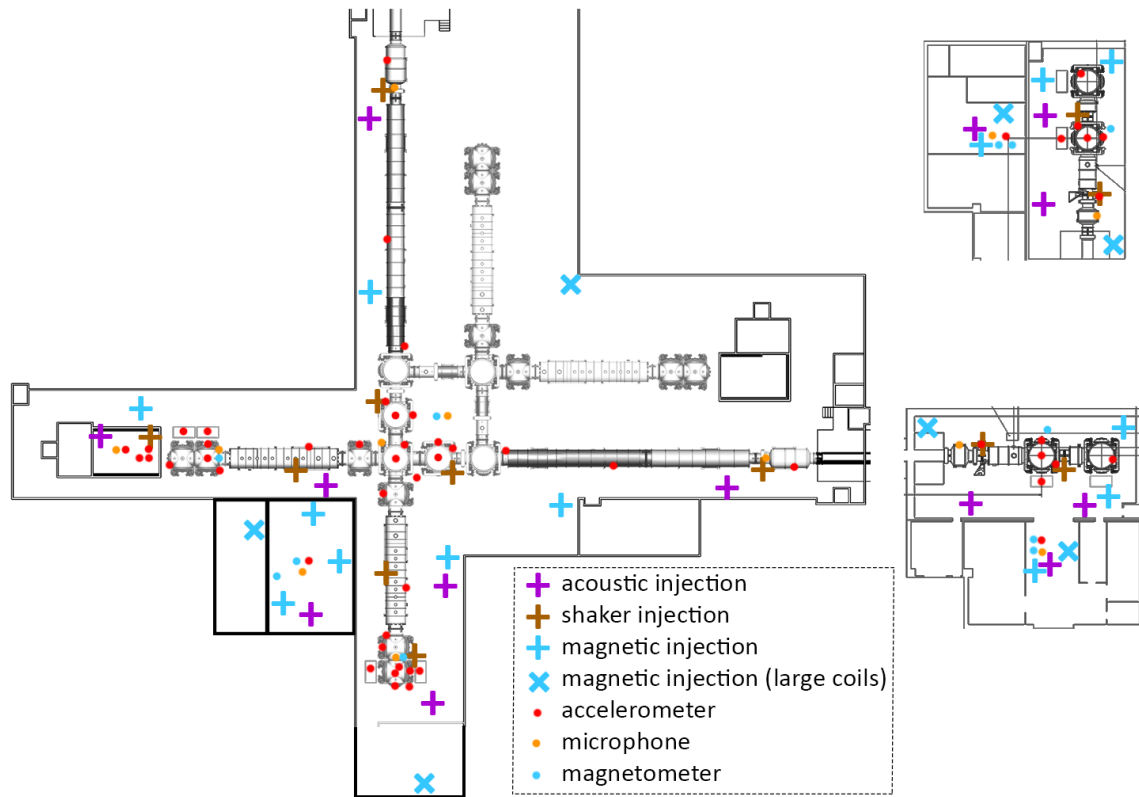


Figure 7. Standard locations for vibration and magnetic injections at the LHO corner station (left), Y end station (top right), and X end stations (bottom right).

The effect of environmental influences on the sensitivity of a GW detector can be studied by making noise *injections*. These are signals produced by human-operated sources with the intention of replicating environmental disturbances with sufficient amplitude to produce excess noise in the DARM spectrum. The amplitude of the excess, combined with measurements of the input signal, can be

used to quantify the coupling behavior (Section 4.3). The most common examples are acoustic injections, generated using speakers, seismic injections generated by vibrational shakers, and magnetic field injections generated by electrical current loops.

At each observatory we inject from 13 locations with acoustic injections, about 12 with shaking injections, and 15 with small-coil magnetic injections, with 7 large-coil magnetic injection locations planned for the fourth observing run (O4) (as explained in Section 4.2.2). The number and locations of shaker injections vary between injection campaigns. For all injection types, multiple injections are made at each location in order to focus on different frequency bands. Additionally, impulse injections (not shown) are made at locations where vibrational injections have revealed strong coupling sites.

Table 1. Specifications for injection equipment.

Equipment	Injection type
Custom enclosure with two 14-in. speakers	Acoustic
Various smaller speakers	Acoustic
APS 113 Electro-Seis® Long Stroke Shaker (APS Dynamics, 2014)	Vibrational
Piezosystem® (Piezosystems, n.d.) shaker with custom reaction mass	Vibrational
Brüel & Kjær® (Brüel & Kjær, 2021) EM shaker with custom reaction mass	Vibrational
1 m diameter copper coil (100 turns)	Magnetic
3 x 3 m and 5 x 5 m coils (80-100 turns)	Magnetic

Injection locations are chosen to best mimic disturbances from outside the detector (Figure 7). To do so we choose them to be as far from the detector and environmental sensors as possible, but we are usually limited by the size of the detector sites themselves (some injections can be made from outside). Time

dedicated to these tests has to be balanced against other instrumental work and observing time, which leads to a trade-off between measurement uncertainty and coverage. We perform injections from as many locations as time allows in order to maximize coverage of potential coupling sites. Increased time allocation toward environmental studies in recent years has allowed for a significant increase in the number of injection locations. Table 1 summarizes the current equipment used and Figure 8 shows photos of some of the equipment.



Figure 8. Injection equipment photos. From left to right: wall-mounted magnetic field injection coil; 14-in. speakers; APS 113 shaker connected to the door of a vacuum chamber by a rigid fiberglass rod; modified Piezosystem shaker clamped to an electronics rack; modified B&K shaker clamped to a beam tube support.

4.2.1 Vibrational injections

Acoustic injections are produced by large speakers. For the corner stations, a pair of speakers mounted on a vibrationally isolated cart (to minimize ground-based vibrational signals) are used. Typically, the injection signal is white noise band-passed between 20-2000 Hz, with narrower bands being used for special follow-up of particular coupling sites.

Seismic injections at low frequency (up to tens of Hertz) during Initial LIGO (iLIGO) were performed with small electromagnetic and piezoelectric

shakers and a weighted cart. A large shaker has been used since the beginning of noise studies for O3. The large shaker can impart up to 133 N of sine force and a peak-to-peak displacement of 158 mm (APS Dynamics, 2014), compared to the electromagnetic shaker which imparts up to 45 N of force and a displacement of 8 mm (Brüel & Kjær, 2021). While smaller shakers can be directly clamped to the interferometer supports, a rigid fiberglass rod is used to connect the large shaker to the interferometer. This has an added benefit of being better able to adjust the direction of the actuation by angling the rod and shaker accordingly.

Two new injection techniques have been developed for localizing vibration coupling sites connected to the vacuum enclosure, such as locations on the vacuum enclosure that reflect scattered light. The techniques rely on the slow propagation speeds (hundreds of meters per second) of shear wave vibrations on the steel vacuum enclosure walls, or of sound waves in the case of acoustic injections. These two techniques were essential in the localization of coupling sites in O3, as discussed in Section 5.2.

4.2.1.1 Beating-shakers technique.

The beating-shakers technique is narrow-band, and involves vibrating the vacuum enclosure at two slightly different frequencies, each injected from a shaker or a speaker at a different location (e.g. a shaker at one location injects a sine wave at frequency f and a shaker at the other location injections at frequency $f + 0.01 \text{ Hz}$). The two injections are adjusted in amplitude to produce strong beats in the GW channel.

Because the injection locations are different, the relative phase of the two injected signals varies with location on the vacuum enclosure, producing a spatial interference pattern. As a result, the phase of the beat envelope varies

with position, and different sites experience maximum chamber wall motion at different times. Consider two sine waves of unit amplitude injected at frequencies f_1 and $f_2 = f_1 + \delta f$ from two source locations where $\delta f \ll f_1$. For simplicity, we can consider that the sources lie along the x -axis. Let r_1 and r_2 be the distances of source 1 and source 2, respectively, to some destination point. The individual signals are

$$y_1(t) = \cos(k_1 r_1 + 2\pi f_1 t) \quad (4.2)$$

$$y_2(t) = \cos(k_2 r_2 + 2\pi f_2 t) \quad (4.3)$$

where $k_1 = 2\pi f_1/c_s$ and $k_2 = \pi f_2/c_s$ with c_s the speed of sound in the injection medium ($c_s \simeq 3000$ m/s in stainless steel). We measure the sum of these signals at their destination:

$$\begin{aligned} y_1(t) + y_2(t) = & 2 \cos \left\{ \frac{1}{2} [k_1 r_1 + k_2 r_2 + 2\pi(f_1 + f_2)t] \right\} \\ & \times \cos \left\{ \frac{1}{2} [k_1 r_1 - k_2 r_2 + 2\pi(f_1 - f_2)t] \right\}. \end{aligned} \quad (4.4)$$

The first cosine factor is a wave with the average frequency $f_{\text{avg}} = (f_1 + f_2)/2$, while the second cosine factor represents a wave with the difference frequency $\delta f/2$. This slowly evolving second factor is the amplitude modulation that results in the familiar beat pattern in the time series of our observation. Its spatial phase is dependent on the difference between the sources, $\Delta r = r_1 - r_2$ is the path length

difference:

$$\varphi \equiv \frac{1}{2}(k_1 r_1 - k_2 r_2) \quad (4.5)$$

$$= \frac{\pi}{c_s}(f_1 r_1 - f_2 r_2) \quad (4.6)$$

$$\simeq \pi \left(\frac{f_1}{c_s} \right) \Delta r \quad (4.7)$$

where we have invoked the assumption that δf is small.

Consider a second destination located r'_1 and r'_2 away from the same sources.

Here we observe a similar signal but with a spatial phase $\varphi' \simeq \pi(f_1/c_s)\Delta r'$ where $\Delta r' = r'_1 - r'_2$. The phase difference between these observations is dependent on the differential path length:

$$\varphi - \varphi' \simeq \pi \left(\frac{f_1}{c_s} \right) (\Delta r - \Delta r'). \quad (4.8)$$

We can see that the peaks of the amplitude modulation (where the second cosine factor evaluates to ± 1) will be spatially separated by a distance $\simeq 30$ m for $f_1 = 100$ Hz in stainless steel.

To observe these amplitude modulations, we can produce spectrograms of the DARM signal, representing the coupling site as one destination, and various sensors as our secondary destinations. The signal appears in spectrograms as a line at f_{avg} rising and fading in amplitude at the beat frequency δf . Realistically we can distinguish the peak arrival times a fraction of a beat period apart, so we can reject the possibility that a sensor less than a few meters from a coupling site if its spectrogram pattern is visibly offset from that of the DARM signal. Of course sensors that lie a full peak away from the coupling site would also appear

to line up with the DARM peaks, not unlikely considering the scale of the corner station vacuum enclosure area, so based on one test we cannot rule out these false positives.

We reject false positives by varying the locations of the shakers and therefore the shape of the spatial interference pattern. A sensor within a few meters of a coupling site will still correlate with DARM, but the phase of far away sensors will change, allowing us to rule out a new set of locations. This technique is therefore a deductive one: we vary and repeat the injection until we are left with only the most likely candidate(s).

4.2.1.2 Impulse injections.

The second injection technique, which is broad band, involves propagation delays in impulse injections. Impulse injections are performed by striking the vacuum enclosure directly with enough force to produce a transient in the GW channel and in nearby accelerometers. The vibrational impulse propagates through the structure of the vacuum enclosure, arriving at different accelerometers and coupling sites at different times.

We can distinguish these arrival times because the propagation velocity is much slower than in solid material, and is only roughly 300 m/s in our case. Using time series plots, the arrival time of the impulse in the GW channel is compared to the arrival time of the impulse in multiple accelerometers. The accelerometers that show the same arrival time as in the GW channel are more likely to be near a coupling site than those that observe the impulse much earlier or later. Again, varying the location of the injection eliminates sensors that match the detector time-of-arrival by chance but are actually far from the coupling site.

An additional consistency check is that the coupling of accelerometers near the coupling site will vary less between different impulse locations than that of accelerometers far from the coupling site. Finally, if the accelerometer is at the coupling site, the impulse in the GW channel will have a resonance structure that is similar to the resonance structure of the accelerometer signal, which can be judged from spectrograms.

4.2.2 Magnetic injections

Improvements have also been made to the magnetic field injection equipment. In order to generate fields strong enough to couple into the GW channel using the 1-m magnetic field coils built during iLIGO, we must focus the power of the coil into narrow bands and combs instead of injecting broadband signals. This was sufficient in iLIGO when strong magnetic coupling occurred primarily through permanent magnets. However, due to the removal of permanent magnets from the test masses, coupling from those sources has decreased and cables and connectors have become the dominant coupling sites above about 80 Hz, introducing more structure to the coupling functions and requiring stronger injections.

To achieve high-amplitude broadband magnetic injections, seven wall-mounted coils, each one a 3 m x 3 m or 5 m x 5 m square of 80-100 turns, are being installed at each site; three at the corner station and two at each end station. These coils are fixed in place and can be operated remotely, allowing for weekly injections to monitor variations in magnetic coupling caused by changes to electronics. Figure 9 compares the old and new magnetic injections. Some coils

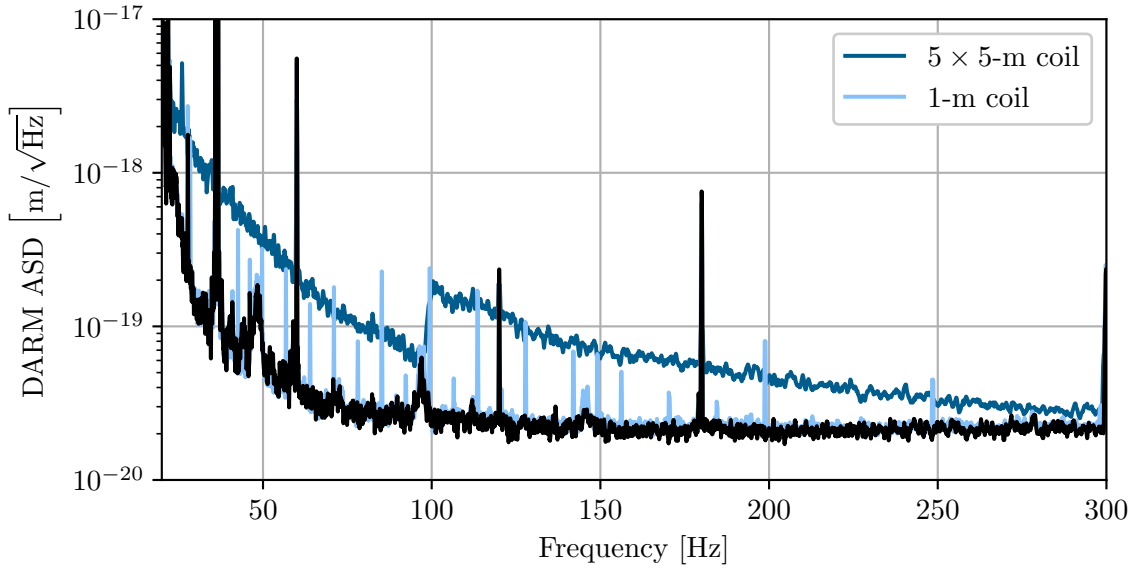


Figure 9. Comparison of the old small-coil comb magnetic field injections with the new large-coil broadband injections.

were installed and operated at the sites during O3 (discussed in Section 5.3); the project will be completed by the start of O4.

4.3 Coupling functions

4.3.1 Single coupling site, sensor, and injection

Suppose there exists exactly one coupling site, i.e. one location at which incident environmental signals result in excess noise in the GW strain data. Suppose also that a sensor is placed at the location of the coupling site, and a noise injection is performed that produces a signal observable by the sensor and the interferometer readout. The coupling mechanism can be modeled in the frequency domain as a linear system:

$$h(f) = C(f)x(f), \quad (4.9)$$

where $h(f)$ is the ASD of the detector (strain) response, x is the ASD of the injection signal as measured by the sensor, and $C(f)$ is the *coupling function*, which represents the amplitude of gravitational wave strain noise per unit amplitude in the sensor. By convention, the strain is typically converted to DARM, in meters, in which case $C(f)$ represents test mass displacement per unit of sensor amplitude. If the injection signal is an acoustic signal and the sensor is a microphone measuring amplitude in Pa, for instance, then the acoustic coupling function is in units of m/Pa.

In both the witness sensor and the detector, some ambient background noise is always present whether or not an injection is produced. Let $h_{\text{bkg}}(f)$ and $h_{\text{inj}}(f)$ be the ASDs of the detector during a period of background noise and during the injection, respectively. Likewise let $x_{\text{bkg}}(f)$ and $x_{\text{inj}}(f)$ be the background and injection ASDs of the sensor. Since the noise adds linearly in the power spectral domain, the actual signal in each is the difference between the injection-time and background-time power spectral densities (PSDs):

$$[h(f)]^2 = [h_{\text{bkg}}(f)]^2 - [h_{\text{bkg}}(f)]^2 \quad (4.10)$$

$$[x(f)]^2 = [x_{\text{bkg}}(f)]^2 - [x_{\text{bkg}}(f)]^2 \quad (4.11)$$

Combining eqs. (4.9)–(4.11), we can measure the coupling function from the background and injection ASDs (Kruk & Schofield, 2016; Nguyen, 2020):

$$C(f) = \sqrt{\frac{[h_{\text{inj}}(f)]^2 - [h_{\text{bkg}}(f)]^2}{[x_{\text{inj}}(f)]^2 - [x_{\text{bkg}}(f)]^2}}. \quad (4.12)$$

The value of a coupling function at a single frequency bin is referred to as a *coupling factor*.

4.3.2 Multiple coupling sites, sensors, and injections

Suppose now there are multiple coupling sites, and a sensor is placed at the location of each site. The detector response to an environmental signal now becomes a linear combination of the sensor signals and their sensor-specific coupling functions:

$$h(f) = \sum_{j=1}^m C_j(f)x_j(f), \quad (4.13)$$

Solving for the coupling function now would require producing multiple injections instead of just one, resulting in a system of n equations with m unknown coupling functions, where n and m are the numbers of injections and sensors, respectively:

$$h_i(f) = \sum_{j=1}^m C_j(f)x_{ij}(f). \quad (4.14)$$

Here $h_i(f)$ is the detector response during injection i , $x_{ij}(f)$ is the amplitude measured by sensor j during injection i , and $C_j(f)$ is the coupling function of sensor j . If $n = m$, eq. (4.14) could be solved to determine the coupling functions of all sensors.

Thus far it has been assumed that the witness sensors are placed precisely at the locations of the coupling mechanisms, but such perfect placement is not realistically feasible given that there are an unknown number of coupling sites at unknown locations. A sensor, even if it is near a coupling site, only measures the injection amplitude at its own location, not at the coupling location. Therefore,

when using real-world sensors, eq. (4.11) is not exact, so eq. (4.12) does not exactly describe the coupling at the coupling site. Nevertheless, as explained above, sensors are distributed in order to maximize coverage of coupling sites and this has been sufficient for producing reliable coupling functions for all sensors, as discussed further in Section 4.4. As seen in Figure 10, the sensor coupling function $C_j(f)$ is a good approximation to the true coupling $C(f)$ if the injection distance from the sensor r_{ij} is much greater than the distance between the coupling site and sensor. This allows us to estimate excess noise in the GW channel $h_i(f)$ without directly measuring the coupling actuation $A_i(f)$.

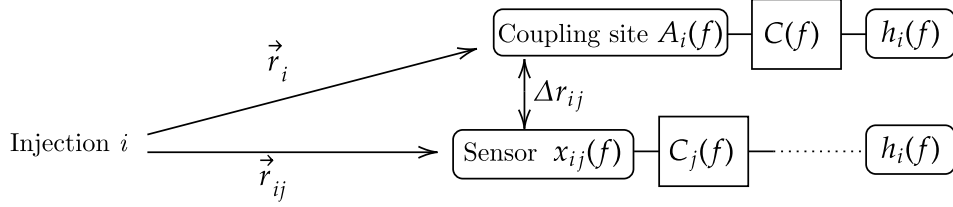


Figure 10. Diagram of a coupling function measurement in the trivial case. An injection i produces a signal $A_i(f)$ at a coupling site, which cannot be measured directly. If the injection is performed sufficiently far, then $\Delta r_{ij} \ll |\vec{r}_{ij}|$, so $C_j(f) \approx C(f)$.

In Figure 11 we can see how complex the experiment system becomes when there are multiple coupling sites of unknown location. If there are two coupling sites A and B , at least two injections i_1 and i_2 are required to distinguish between the coupling mechanisms. The GW channel response to injection i_1 is therefore the sum of the contributions of the actuation signals $A_{i_1}(f)$ and $B_{i_1}(f)$, and likewise for injection i_2 . Again, at best we merely approximate the actuation signals $A_i(f)$ and $B_i(f)$ with sufficiently close sensors, although we do not know *a priori* which sensors are near coupling sites.

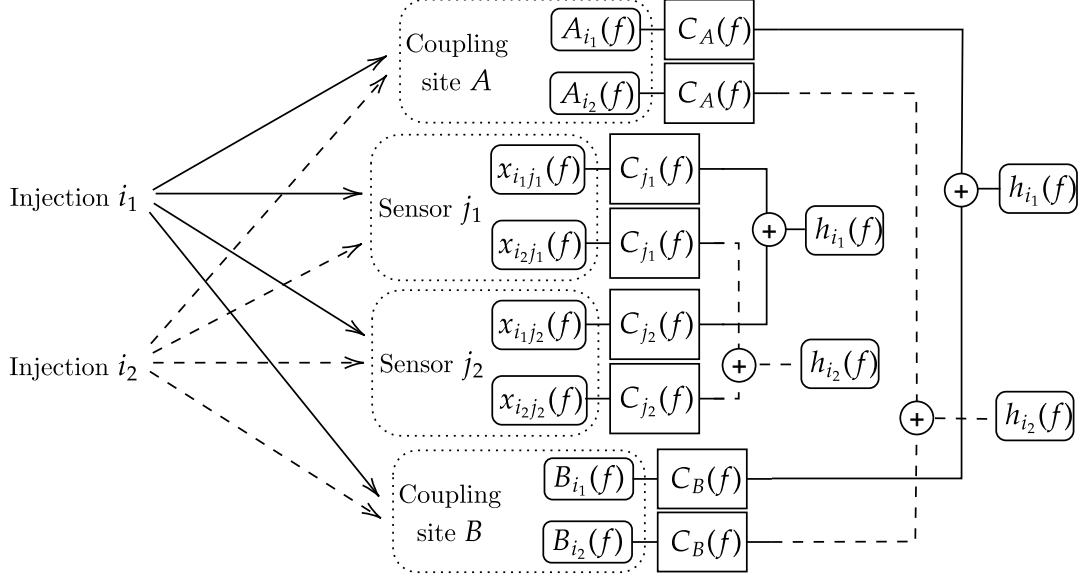


Figure 11. Expanding Figure 10 to two injections i_1 and i_2 , two sensors j_1 and j_2 , and two coupling sites A and B . Each injection response $h_i(f)$ is itself a sum across contributions from A and B . The goal is to determine the sensor couplings $C_j(f)$ that reproduce $h_i(f)$ using the sensor measurements $x_{ij}(f)$ since the true coupling actuations $A_i(f)$ and $B_i(f)$ are not known.

4.3.3 Solving the coupling equations

One hurdle remains in attempting to solve eq. (4.14). In practice, typically $n < m$ due to logistical constraints on the number of injections one could perform during a realistic time window, which makes the system of equations underdetermined. A straight-forward least-squares regression is therefore not always feasible. Below are two approximation methods for determining $C_j(f)$ for all sensors.

Nearest-sensors approximation. One method of forcing $n = m$ is reducing the number of sensors in each equation, by asserting $x_{ij}(f) = 0$ for sensors that are sufficiently far from the source of injection i . This can be done by ordering the sensors by distance from the injection source and applying the assertion to the

$m - n$ farthest sensors. Issues can arise if there are sensors that are never near enough to any injection source, causing them to zeroed out for all injections; this requires that injections be distributed such that each sensor is near enough to at least one injection.

Nearest-injection approximation. Instead of solving eq. (4.14) in full, one can approximate $C_j(f)$ for each sensor independently of other sensors. Given a sensor j , eq. (4.12) can be repurposed by replacing x with x_{ij} and h with h_i to compute a single-injection “coupling function” $\mathcal{C}_{ij}(f)$ for each injection:

$$\mathcal{C}_{ij}(f) = \sqrt{\frac{[h_{i,\text{inj}}(f)]^2 - [h_{i,\text{bkg}}(f)]^2}{[x_{ij,\text{inj}}(f)]^2 - [x_{ij,\text{bkg}}(f)]^2}}. \quad (4.15)$$

The closer an injection is to a sensor i , the more accurately $\mathcal{C}_{ij}(f)$ approximates $C_j(f)$, since the detector response would be dominated by coupling near sensor j . Therefore one can construct the sensor coupling function by choosing at each frequency bin the coupling factor corresponding to the nearest injection, determined by the highest sensor amplitude (using the assumption that injection amplitudes are equivalent). That is, for a frequency f_k and a set of injections \mathcal{I} , one can measure the sensor amplitudes $\{x_{ij}(f_k) \mid i \in \mathcal{I}\}$, compute the single-injection coupling functions $\{\mathcal{C}_{ij}(f_k) \mid i \in \mathcal{I}\}$, and construct the approximate sensor coupling function

$$\tilde{C}_j(f_k) := \mathcal{C}_{lj}(f_k) \text{ where } l = \underset{i \in \mathcal{I}}{\operatorname{argmax}} (x_{ij}(f_k)). \quad (4.16)$$

If the distribution of injection locations provides sufficient coverage of sensor locations, then $\tilde{C}_j(f) \approx C_j(f)$. Shortcomings of this assumption are discussed in Section 4.4.

Figure 12 provides an example of a single-injection coupling function measurement for a PSL acoustic injection. Figure 13 shows an estimated ambient noise based on an accelerometer coupling function constructed from five single-injection coupling functions. For simplicity only five injections were used to produce this example, however in practice the number of injections performed near a sensor can be much higher.

Due to hardware limitations it can be possible for an injection signal to be strong enough to produce excess noise in a sensor ASD but not in the GW detector ASD. For frequency bins where this is the case, an upper limit on $\mathcal{C}_{ij}(f_k)$ can be established by assuming, as a worst-case scenario, that all of the detector noise at that frequency is produced by the coupling alone

$$\mathcal{C}_{ij,\text{UL}}(f) = \frac{h_{i,\text{bkg}}(f)}{\sqrt{[x_{ij,\text{inj}}(f)]^2 - [x_{ij,\text{bkg}}(f)]^2}}. \quad (4.17)$$

The larger the injection amplitude, the better this upper limit can be constrained. The boundaries between measurements, upper limits, and null results are established by two ASD ratio thresholds: a sensor threshold and a detector threshold. Let $r_x := x_{ij,\text{inj}}(f)/x_{ij,\text{bkg}}(f)$ and $r_h := h_{i,\text{inj}}(f)/h_{i,\text{bkg}}(f)$ represent the injection signal-to-noise ratios if the sensor and GW detector ASDs, respectively. If $r_x \geq t_x$ and $r_h \geq t_h$, where t_x is the sensor threshold and t_h is the detector threshold, then a measurement is computed via eq. (4.15). Otherwise, if $r_x \geq t_x$ but $r_h < t_h$, then eq. (4.17) is used to place an upper limit on the coupling. If $r_x < t_x$ and $r_h < t_h$, then neither a measurement nor upper limit is computed. The null hypothesis is thus assumed:

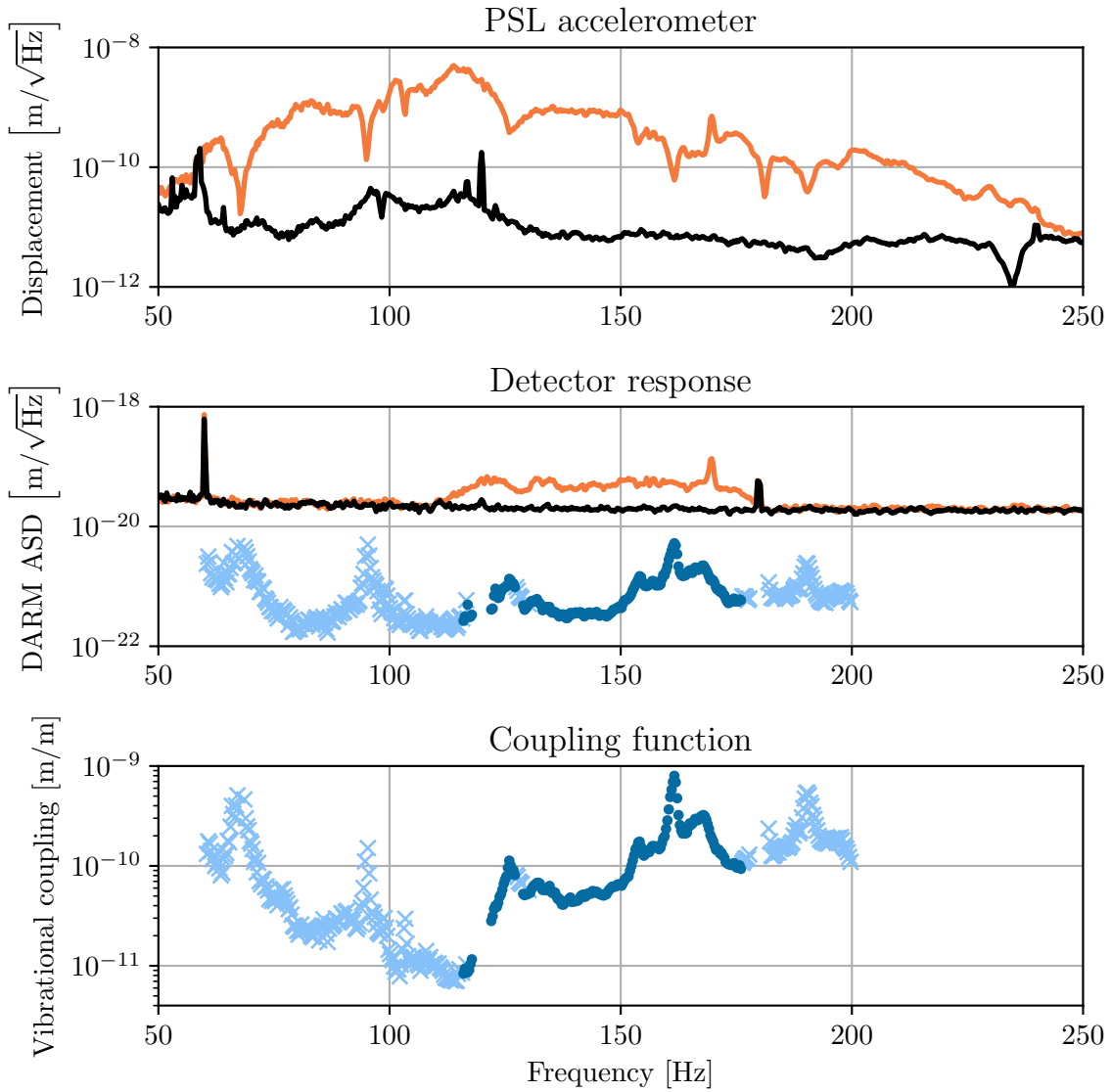


Figure 12. Example of a broadband acoustic noise injection and measurement of a single-injection coupling function. Top: displacement of an accelerometer in the PSL room during background time (black) and injection time (orange). Middle: DARM during background time (black) and injection time (orange). Estimated ambient levels for the accelerometer are shown as dark blue dots, with upper limits shown as light blue crosses. Bottom: single-injection coupling function used to produce estimated ambient above.

$$\mathcal{C}_{ij,\text{null}}(f) = \frac{h_{i,\text{bkg}}(f)}{x_{i,\text{bkg}}(f)}. \quad (4.18)$$

The values of t_x and t_h are determined based on typical level of random fluctuations observed in the spectra, but often values of $t_x = 10$ and $t_h = 2$ are used for most types of sensors and injections. The higher choice of t_x is due to the environmental sensors being much more sensitive to random fluctuations in the ambient noise level than the interferometer is.

The coupling function as approximated in eq. (4.16) is used for comparing coupling between different sensor locations and producing estimates of interferometer noise levels, e.g. as part of event validation (see Section 5.4). References to a sensor's coupling function will hereafter refer to this approximate quantity. Figure 13 provides an example of an estimated ambient for an accelerometer on the HAM6 vacuum chamber (which houses the interferometer output optics). The PEM website provides coupling functions for all accelerometers, microphones, and magnetometers produced from the most recent campaign of injections (R. Schofield et al., 2021).

Once enough injections are performed and reliable coupling functions are measured for the complete array of PEM sensor, the results from all sensors for a single coupling type are aggregated once more, into a single *site-wide* coupling function. A site-wide coupling function is produced for each coupling type and interferometer: vibrational noise at LHO, magnetic noise at LHO, vibrational noise at LLO, and magnetic noise at LLO. These are made by choosing, in each frequency bin, the highest coupling value across all sensors. This aggregation method can be applied to the estimated ambients as well, picking the highest ambient noise estimated by all sensors. The site-wide estimated ambient is

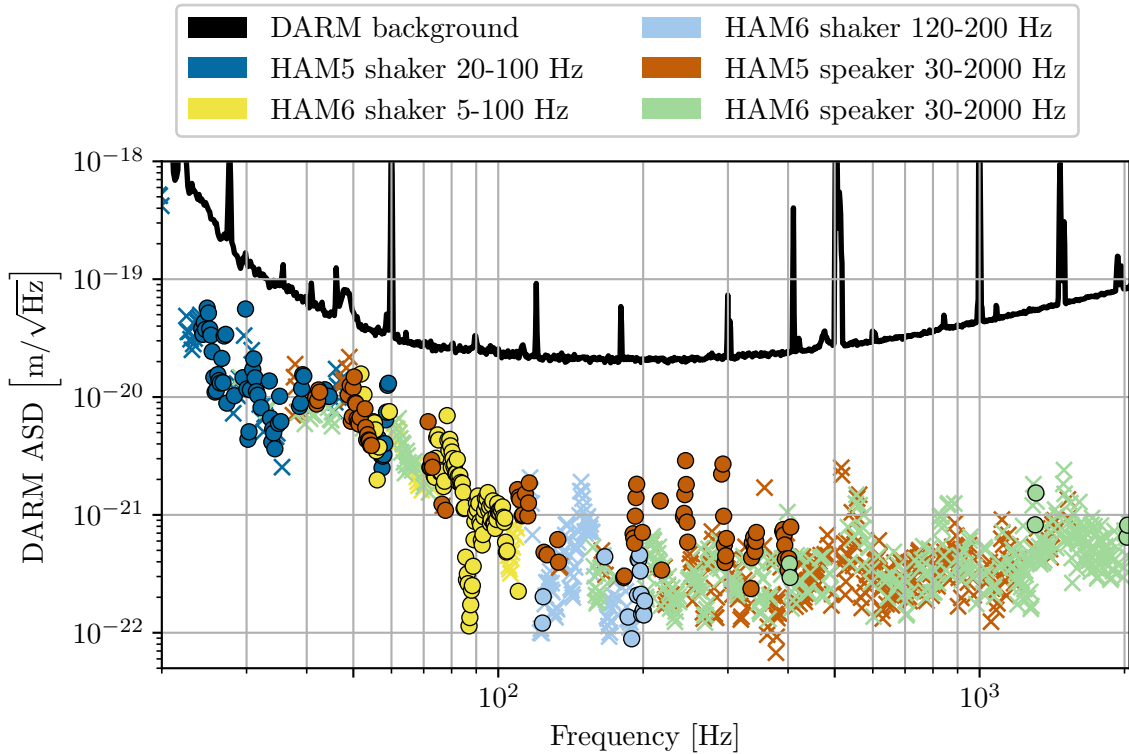


Figure 13. Ambient noise level for the LHO HAM6 Y-axis accelerometer estimated from a composite coupling function, using acoustic and seismic injections near the output arm.

usually more useful, as it summarizes the coupling mechanisms that affect the interferometer the most, with the sensor chosen in each frequency bin indicating the rough location of the dominant coupling site at that frequency. These site-wide estimated ambients represent the environmental noise budget of the LIGO detectors and are therefore the primary data products of an extensive injection campaigns.

4.4 Uncertainties and limitations of coupling functions

4.4.1 Comparison to transfer functions

Environmental coupling is characterized using coupling functions instead of transfer functions because perfect coherence is not assumed in the system. Low

coherence can arise either due to non-linearity in the coupling or due to the spacing between the sensor and coupling site. On a superficial level, a coupling function lacks a phase response component, representing only the magnitude response in the system. Coupling functions also differ fundamentally from transfer functions in the sense that they do not assume the input signal to be the true actuation signal, but rather merely a witness of the actuation, while the actuation is in fact occurring at the location of the true coupling site.

4.4.2 Assumptions about coupling mechanisms

Equation (4.12) relies on two assumptions about the coupling mechanism. First, the coupling is assumed to be linear in amplitude, e.g. doubling the amplitude of the injection would double the amplitude of the GW detector response. This is confirmed when performing injections by repeating them with different amplitudes and ensuring that the detector response scales proportionally with the injection amplitude. Second, the coupling function ignores any up- or down-conversion of the signal between the sensor and the GW detector. Such non-linear coupling can be very significant for scattering noise and bilinear coupling, but is not accounted for in the estimates of linear coupling. One way to check for non-linear coupling is by sweeping single frequency injections over time and searching for off-frequency responses in the GW detector. Frequency changes from non-linear coupling can be an issue in broadband injections where up- or down-converted noise in the interferometer readout appears in the injection band, resulting in artificially higher estimates at those frequencies. We split broadband injections into smaller frequency bands to avoid this effect when necessary. One approach for quantifying non-linear coupling is presented in Washimi et al. (2020).

4.4.3 Hardware limitations

Injection amplitudes. To measure coupling, we inject signals large enough to produce a response in the detector, but the maximum amplitude of injections is limited by the sensitive range of the environmental sensors (saturation produces an overestimate of coupling). This effectively limits how far below the detector noise background we can probe for coupling or establish upper limits.

Recall that eq. (4.16) was based on assuming that injection amplitudes are equivalent. However, this assumption is ambitious: since injections vary with distance to sensors, the amplitudes used have to be adjusted to achieve a large signals in the sensors and in the GW channel. This means that the highest-amplitude injection measured by a sensor is not necessarily the nearest injection to that sensor. If a further injection was performed using a much larger amplitude, its measured amplitude can trump that of a nearer injection, leading to the algorithm choose a more distant injection source location when determining \tilde{C}_j . To prevent this issue, once C_{ij} is computed for all sensors for a single injection, an additional sensor threshold is applied that is a fraction of the highest amplitude observed by all sensors. This threshold is used only to demote measurements to upper limits. By doing so, this injection-dependent threshold vetoes measurements produced by sensors that are far from the injection. The lower it is, the more it will limit measurements to only those we are most confident of. For the O3 injections, the threshold was set at one third, meaning that a coupling measurement is demoted to an upper limit if the sensor measuring it observes the injection at less than a third of the amplitude observed by the sensor closest to the injection.

Uncertainty due to injection locations. As mentioned above, the model in eq. (4.14) relies on the assumption that the environment is monitored at the

coupling site. The density of sensors is not great enough for this to be strictly true, especially if the source of the environmental signal is closer to the coupling site than the sensor is. The detector response to an injection depends on the distance between the injection and coupling site, whereas the sensor response depends on the distance between the injection and sensor. Varying the injection location therefore varies the relative scaling of the numerator and denominator of eq. (4.15), affecting the measurement of $\mathcal{C}_{ij}(f)$ and subsequently the sensor coupling function via eq. (4.16). Therefore, a finite spacing of sensors leads to some degree of uncertainty in the coupling functions. This uncertainty also propagates to projected noise levels in the GW channel using these coupling functions.

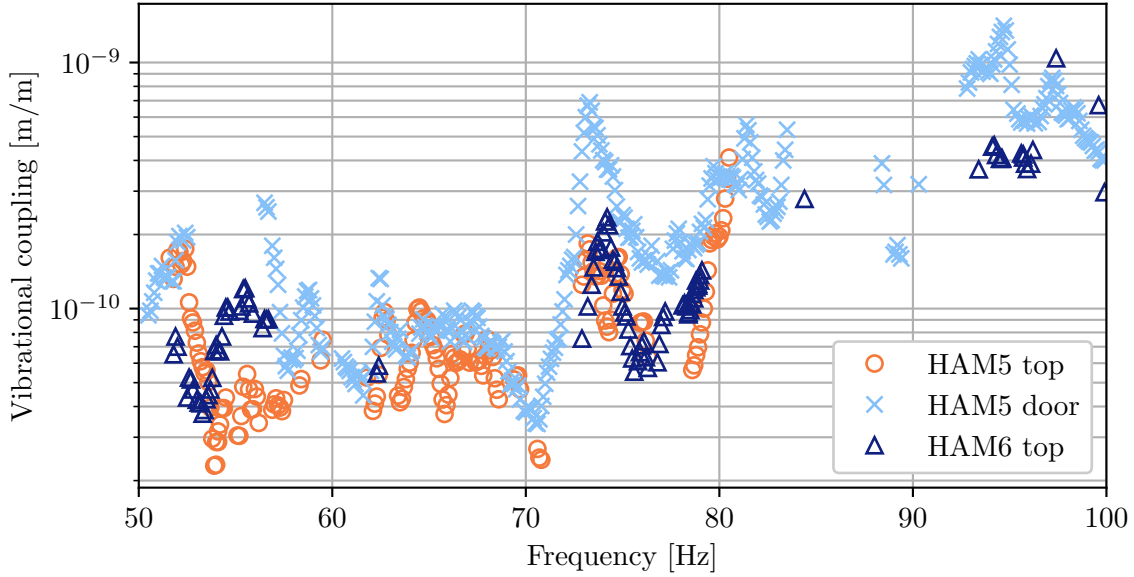


Figure 14. Single-injection coupling functions (upper limits not shown) for the HAM5 Y-axis accelerometer for three different shaker injection locations (on top of HAM5, on top of HAM6, and on the HAM5 chamber door).

Since the uncertainty manifests as a multiplicative scaling of $\mathcal{C}_{ij}(f)$, it can be described by computing a geometric standard deviation of $\mathcal{C}_{ij}(f)$ for a single sensor over a range of injection locations, at each frequency bin. Figure 14 shows

single-injection coupling functions for an accelerometer measured from shaker injections produced from three locations (the distribution of injection locations is discussed in Section 4.2. Since the injection locations are close enough to the accelerometer, it can be assumed that the variance is primarily due to finite spacing effect. Averaged across all frequency bins, the geometric standard deviation between injection locations is 1.4, i.e. coupling functions measured from vibrational injections can be expected to vary by a factor of 1.4 when measured by different injection locations.

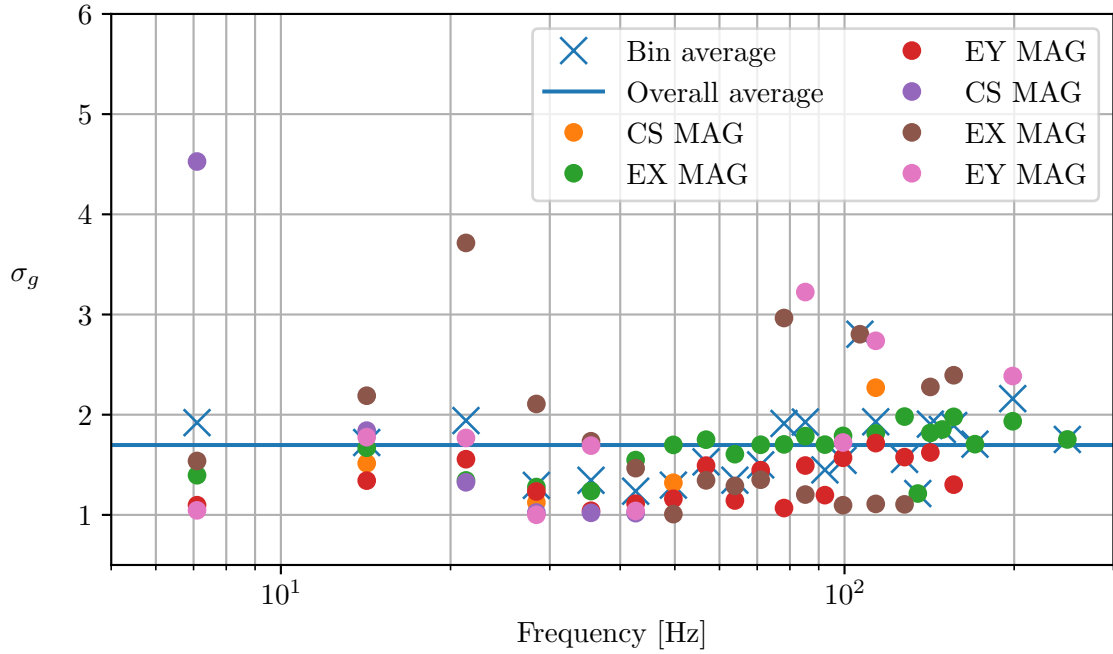


Figure 15. Magnetic coupling function uncertainty. Points show geometric standard deviations of magnetic coupling measurements when varying the injection location.

A similar study was performed combining geometric standard deviations for various magnetometers at both observatories (Figure 15). There are fewer magnetic injection locations to use for the comparison, but since coupling can be measured at each station (a corner station and both end stations) at each of the two LIGO observatories, there are twelve magnetometers that can be used, each with two

or more injections nearby. The result of this study is that magnetic coupling measurements and noise projections vary by a factor of 1.7. This is slightly greater than that of vibrational measurements, since the lower number of magnetometers means that the distances between coupling sites and sensors is greater, amplifying the finite spacing effect.

For both vibrational and magnetic coupling, these estimated uncertainties are acceptable given that conclusions made from coupling functions are often more qualitative than strictly quantitative, i.e. identifying and localizing coupling mechanisms is more important than precise estimates of the detector response. That said, more precise noise estimates may become important for quantifying the impact of environmental transients on GW event candidates, as discussed in Section 5.4.

Nodal artifacts from acoustic injections. In the case of acoustic injections, the uncertainty in a coupling function can be exacerbated when nodes and anti-nodes in the acoustic signal coincide with the location of a sensor but not a coupling site. This results in peaks and troughs in the sensor spectrum at frequencies that have a node or anti-node at the sensor location, respectively. These artifacts can impact any sensor, but are more noticeable in microphone spectra than accelerometer spectra, possibly because the stiffness of the vacuum enclosure results in effectively averaging over a larger area; in microphones, the peak-to-trough ratio is typically a factor of a few. The peaks and troughs are present in the sensor but not in the detector spectrum, because the sensor monitors a single point whereas the coupling to the interferometer is spread across a large enough area for the effects of nodes and anti-nodes to average out. Consequently, this effect imprints troughs and peaks onto the coupling function.

The artifacts can be smoothed out of the spectra by applying a moving average over $x_{ij,\text{inj}}(f)$ before computing $\mathcal{C}_{ij}(f)$. The moving average window must be on the scale of a few Hz since this is typically the scale of the peak-to-peak distances. On the other hand, smoothing of spectra can also result in less accurate coupling measurements when narrow mechanical resonances are present, so the window must balance the smoothing of artifacts against this disadvantage. For accelerometer spectra, analyzing injections with various smoothing parameters show that the best smoothing window is a frequency-scaled window (which we call “logarithmic smoothing”) with a width of $\Delta f = 0.005f$ (e.g. the amplitude of the 100-Hz frequency bin is an average of the bins in the range 100 ± 0.5 Hz). Since microphones are much more sensitive to nodal artifacts while being less sensitive to narrow mechanical resonances (they would have to be strong enough to produce audible signals), their spectra can be smoothed much more aggressively: we use a window of width $\Delta f = 0.15f$ (e.g. the amplitude of the 100-Hz frequency bin is an average of the bins in the range 100 ± 15 Hz).

4.5 The `pemcoupling` package

This section covers the technical details of the `pemcoupling` python package (Nguyen, 2020), which includes command-line tools for processing large numbers of injections and producing single-injection coupling functions, coupling functions, and multi-channel summary coupling functions.

The package uses the `gwpy` library for fetching raw time series data and producing ASDs of the GW strain channel and auxiliary channels from user-provided background and injection times.

4.5.1 Processing steps

A number of pre-processing steps are performed to condition the data for analysis. First, the auxiliary channel time series are examined for evidence of saturation. Injections can cause saturation in two ways: actuator saturation due to over-driven amplifiers, or sensor saturation due to hitting the maximum amplitude the sensor can record.

During magnetic injections, the injection amplitude typically has to exceed background by a few orders of magnitude to produce noise in the GW channel, so comb magnetic injections are the most likely to saturate at the actuator. They are also capable of saturating the sensors if performed too close (such as in the electronics racks). In either case, intermodulation distortion occurs, generating peaks at sums and differences of the comb line frequencies while also reducing signal power in the injection lines. If the saturation is occurring at the actuator, the measured coupling is still accurate, but upper limits are higher due to the reduced signal power. On the other hand, sensor saturation results in inaccurate coupling measurements, because the line amplitudes no longer reflect the true magnetic signal at the sensor location.

During vibrational injections, the high number of accelerometers means it is often possible that the nearest ones saturate. This results in artificial white noise in the amplitude spectra. The consequence is measuring a lower coupling function at frequencies where the saturation artifact dominates. For most accelerometers, the highest background noise levels are observed in the hundreds of Hertz, so usually accelerometer saturation mainly affects measurements at the quieter low frequencies. In more extreme cases that affect the entire spectrum, distinguish

between real signals and artificial saturation noise is not feasible, so no reliable measurements can be made at all.

To avoid these negative effects, coupling functions are only measured for sensors whose time series do not exceed 32,000 ADC counts in absolute amplitude, close to the maximum amplitude of the raw sensor data processed by the data acquisition system.

Once the valid time series have been selected, they are converted to ASDs. At this point, triaxial magnetometer channels are combined in quadrature. Each magnetometer measures the x , y , and z components of its local magnetic field independently. The directions of magnetic signals are not important to coupling, however. Instead we are concerned with the absolute magnitude of the field. Thus, a new channel is produced by summing the ASDs of the individual components in quadrature. Note that when measuring coupling using the field magnitude in the frequency domain the quadrature sum has to be performed in the frequency domain, not the time domain prior to Fourier transforming. This is because there may be DC offsets to the raw time series, which are removed when taking the Fourier transform of the signals. The quadrature sum of two time domain signals with DC offsets, on the other hand, will have cross-terms between the DC offset component and the AC components.

All PEM channels have accompanying calibration measurements (R. Schofield et al., 2021). Calibration for microphones and magnetometers is simply a constant conversion of Pa/count or T/count, respectively. Accelerometer ASDs are calibrated to acceleration units (m/s^2); additionally, they are converted to displacement (m) by dividing each bin by $(2\pi f)^2$ where f is the bin frequency. The

calibration factors for all sensors are not always constant with respect to frequency, but coupling measurements are always in the range where they are.

For acoustic injections, spectral smoothing is applied at this point, in order to suppress nodal artifacts as explained in Section 4.4.3. Finally, the single-injection coupling functions and upper limits are measured as in eqs. (4.15)–(4.18). For comb or line injections, user input defines the frequencies to analyze and the width, in Hz, of the frequency-domain window around each frequency to analyze. If there is more than one bin in each search window, as is usually the case given the high frequency resolution we use to analyze narrowband injections, only the highest coupling computed from among the bins is kept so that each line produces one measurement or upper limit.

4.5.2 Data products

For each $\mathcal{C}_{ij}(f)$, the data are saved in the following forms:

1. comma-separated text file consisting of coupling measurements, flags, and raw spectra
2. plot of the coupling function in physical units (meters per calibrated sensor unit, e.g. Tesla for magnetometers)
3. plot of the raw coupling function (units of meters per analog-to-digital counts)
4. figure containing two subplots: one showing the background and injection spectra of the auxiliary sensor, and one showing the background and injection spectra of the GW strain data and the estimated environmental noise projection.

Post-processing, to aggregate single-injection coupling functions into coupling functions, is done with the `pemcoupling-composite` command. For each sensor, the composite coupling code takes all coupling functions measured and builds a new one using the nearest-sensor (highest-amplitude) method. For sensors for which the coupling functions are measured from comb injections, i.e. magnetometers, again a frequency search window around each line frequency is used to check for coupling measurements within the windows, as opposed to processing all bins individually.

Lastly, the composite coupling functions are combined to produce the site-wide results using the `pemcoupling-summary` command. The site-wide coupling plots are produced in two ways: by taking the sensor with the highest coupling value in each bin, and by taking the sensor with the highest estimated ambient value in each bin.

See Appendix A for examples of figures produced by the `pemcoupling` code.

CHAPTER V

STUDIES OF ENVIRONMENTAL NOISE DURING O3

O3 was preceded by an engineering run (ER13), a month-long period during which the interferometer is operational at low-noise levels but not observing GW events, to provide time for detector commissioning and noise studies. The main injection campaigns used to measure coupling for all PEM sensors are performed during these engineering runs. A mid-run commissioning break ER14 took place in the month of October of 2019, during which some of the most crucial coupling measurements were repeated. Although the observing run does not end with an engineering run, some time is still made for end-of-run commissioning that assesses changes in detector performance, including PEM noise studies, before the instruments are finally shut down for major upgrades. The pre- and post-O3 campaigns are summarized in Table 2. There were fewer post-O3 injections due to the premature termination of O3 in the wake of the COVID-19 pandemic.

Table 2. Number of injections performed at each station and for each injection type throughout the pre-, and post-O3 injection campaigns.

	Station	Magnetic (comb)	Magnetic (broadband)	Vibrational (acoustic)	Vibrational (shaker)
Pre-O3	Corner	16	10	11	63
	End-X	9	0	6	7
	End-Y	9	0	9	14
Post-O3	Corner	10	2	11	0
	End-X	4	0	4	0
	End-Y	9	0	5	0
Pre-O3	Corner	7	3	14	0
	End-X	3	0	2	0
	End-Y	4	0	4	0
Post-O3	Corner	0	5	0	0
	End-X	0	3	0	0
	End-Y	0	4	0	0

5.1 Evaluation of coupling functions

Before discussing results of injection studies and coupling function measurements in O3, it is necessary that we take a moment to assess how well they estimate excess noise in the interferometer when the noise source is known to be the result of environmental coupling. Of course, one could do this by applying coupling functions to a set of “test” injections, but this would require performing more injections, which as mentioned before is typically not feasible. Furthermore, since the intention of the coupling functions is to estimate the impact of noise signals originating from a broad variety of sources, it make sense to use non-laboratory signals when evaluating coupling estimates. Therefore, we use noise events not produced by injection equipment to evaluate how accurately the coupling functions recover the actual excess noise observed in the GW strain data.

Thunderstorms are known to produce short-duration transients in the strain data at tens of Hz by exciting vibrational coupling associated with scattered light. S190510g, a long-duration GW trigger observed while a thunderstorm was underway at LLO, overlapped many such noise artifacts throughout its 255-s time span. We can rule out any astrophysical origins for these signals: they are observed by accelerometers at all stations with reasonable delays for sound propagation, they sound like thunder on the microphone channels, and they have the right frequency content and duration. One of the loud events was also consistent with the time put in by an operator for a loud thunder clap. Figure 16 shows constant-Q transforms of one of these thunder noises as seen in the LLO strain channel as well as one of the End-Y accelerometers, where scattered light coupling was a dominant noise source. Coupling functions for this accelerometer and several others at the End-Y station, are capable of estimating the amplitude of multiple noise transients to

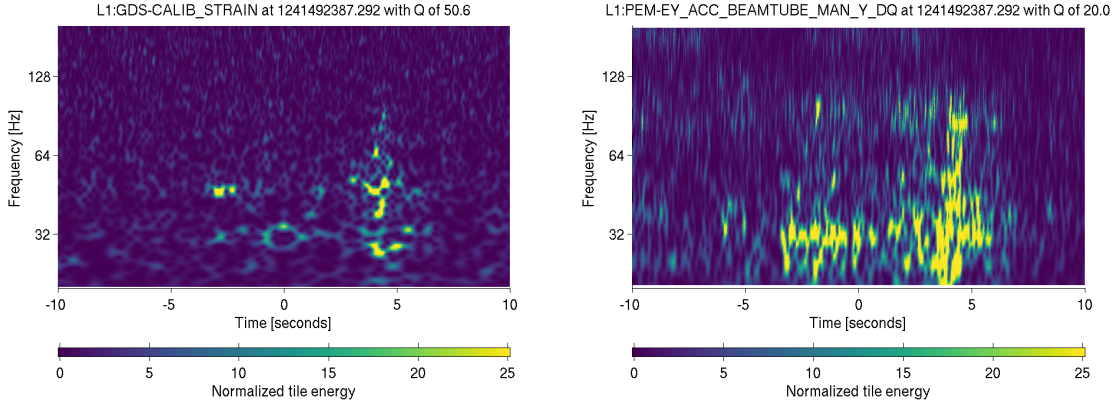


Figure 16. Constant-Q transforms of the GW strain channel (left) and an accelerometer (right) during thunder noise at LLO.

within a factor two during a particularly loud thunderstorm (Nguyen & Schofield, 2019).

Helicopter flyovers can produce narrow-band features up to tens of seconds long at harmonics of the main helicopter rotor frequency. These are reported by site operators if they are loud enough to be heard even within the observatory buildings. At each site, three flyovers were reporting during O3. Table 3 presents the noise estimates from coupling functions for various sensors during these events (Nguyen & Schofield, 2020). One of the events at LLO was omitted because no excess noise was visible in DARM spectrograms. For each flyover, the sensor with the highest projection in DARM is reported. The last column shows the ratio between the estimated projection amplitude and the actual amplitude, confirming that coupling functions can predict the amplitudes of lines produced by helicopter flyovers to within a factor of two in most cases.

Long-duration noise due to vibrations from rain and the building heating, ventilation, and air conditioning (HVAC) is also well characterized by coupling

Table 3. Noise projections for five helicopter flyovers at the LIGO detectors.

Frequency [Hz]	Channel	Estimated noise / Actual noise
	Observatory: LHO Time: 2019-05-09 21:30 UTC	
27	H1:PEM-CS_ACC_HAM6_OMC_Y_DQ	0.7
27	H1:PEM-EY_ACC_BSC10_ETMY_X_DQ	0.5 (upper limit)
90-100	H1:PEM-CS_ACC_HAM6_OMC_X_DQ	0.8
90-100	H1:PEM-EY_ACC_BSC10_ETMY_X_DQ	0.8 (upper limit)
	Observatory: LHO Time: 2019-05-21 03:11 UTC	
26	H1:PEM-CS_ACC_HAM6_OMC_Y_DQ	0.4
39	H1:PEM-CS_ACC_HAM6_OMC_Y_DQ	1.4
52	H1:PEM-CS_ACC_HAM6_OMC_X_DQ	0.3
75	H1:PEM-CS_ACC_HAM6_OMC_X_DQ	0.4
	Observatory: LHO Time: 2019-06-08 17:24 UTC	
33-40	H1:PEM-CS_ACC_HAM6VAC_SEPTUM_Y_DQ	1.8
	Observatory: LLO Time: 2019-09-02 17:34 UTC	
70-80	L1:PEM-CS_ACC_HAM6_OMC_X_DQ	2
	Observatory: LLO Time: 2020-01-22 22:25 UTC	
40-44	L1:PEM-CS_ACC_HAM6_OMC_X_DQ	0.6
90-95	L1:PEM-CS_ACC_HAM6VAC_SEPTUM_Y_DQ	1.8

functions at LHO (Banagiri, Covas, & Schofield, 2019; R. M. S. Schofield, Nguyen, Banagiri, Merfeld, & Effler, 2019).

5.2 Vibrational noise studies during O3

Aggregating our coupling measurements made during O3, we arrive at Figure 17, the total ambient contribution of vibrational noise sources during O3, produced by combining the highest coupling measurements from accelerometers and microphones and computing their ambient noise projections to the DARM channel. At both observatories, scattered light noise dominates at low frequency (below 100 Hz): at the output arm at LHO and at ETMY at LLO. At higher frequencies the input beam jitter noise dominates. The physical mechanisms behind these effects were described in Section 3.3.

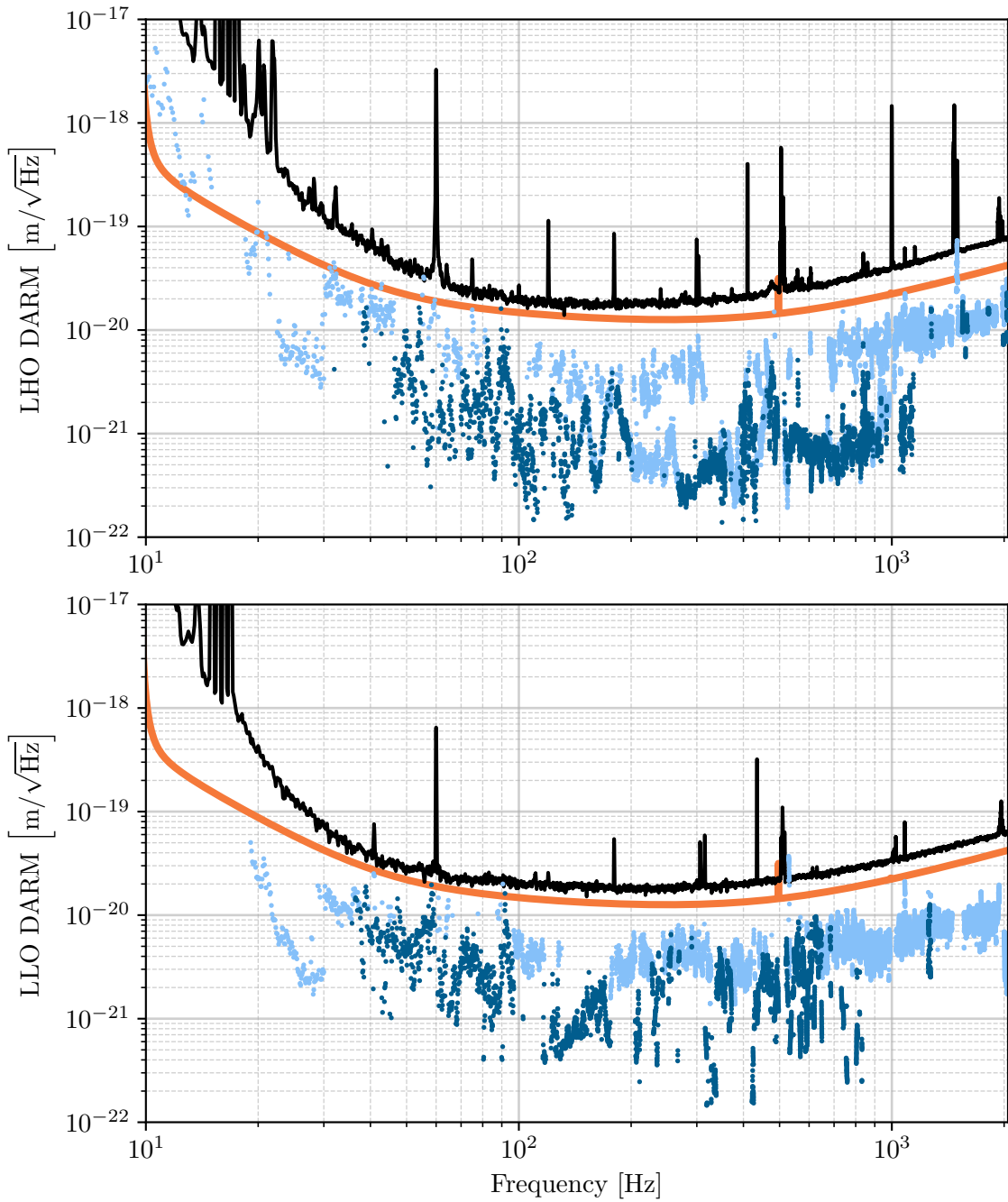


Figure 17. DARM noise from all *vibrational* coupling sources at LHO (top) and LLO (bottom). Dark blue dots represent measurements, while light blue dots represent upper limits. The black and orange curves show the O3 sensitivity and design sensitivity, respectively.

5.2.1 Scattered light at the HAM5/6 septum

At LHO, investigations throughout O3 showed that scattering noise at the output arm produces noise near the detector noise background in the frequency range of 38–100 Hz. The sensors with the highest ambient projections in this band were accelerometers located on the HAM5 and HAM6 vacuum chambers, which contain the GW channel readout, as well as the optics of the output mode cleaner, squeezed light system, and signal recycling cavity. The coupling was excited most strongly by injections around the output arm, but acoustic noise produced as far as the Y-arm manifold ≈ 50 m away produced excess noise in DARM. Figure 18 shows shaker injections performed at the HAM5/6 area. Mechanical resonances in the vacuum chamber structure alter the frequency content of the injection signal as it propagates, so the sensitivity of the detector to the shaker injections is not uniform but rather characterized by various peaks and troughs. The estimated ambient noise levels of the worst of these peaks reaches within a factor of two below the DARM background in the 50-60 Hz and 80-100 Hz bands, higher than observed by other corner station shaker injections.

A more thorough investigation was required to localize the exact scattering surface. We carried out impulse injections, as described in Section 4.2.1.2, at 37 locations throughout the corner station, including a number of spots on the chamber walls and doors of HAM5 and HAM6. Figure 19 shows time series and spectrograms the GW channel and in various output optics accelerometers during a single impulse injection performed in the HAM5/6 area. Multiple sensors observe an impulse time-of-arrival matching that of the GW channel, but repeating the injection from several other locations rules out sensors that do not match it consistently across multiple injections. In this case we find that the septum

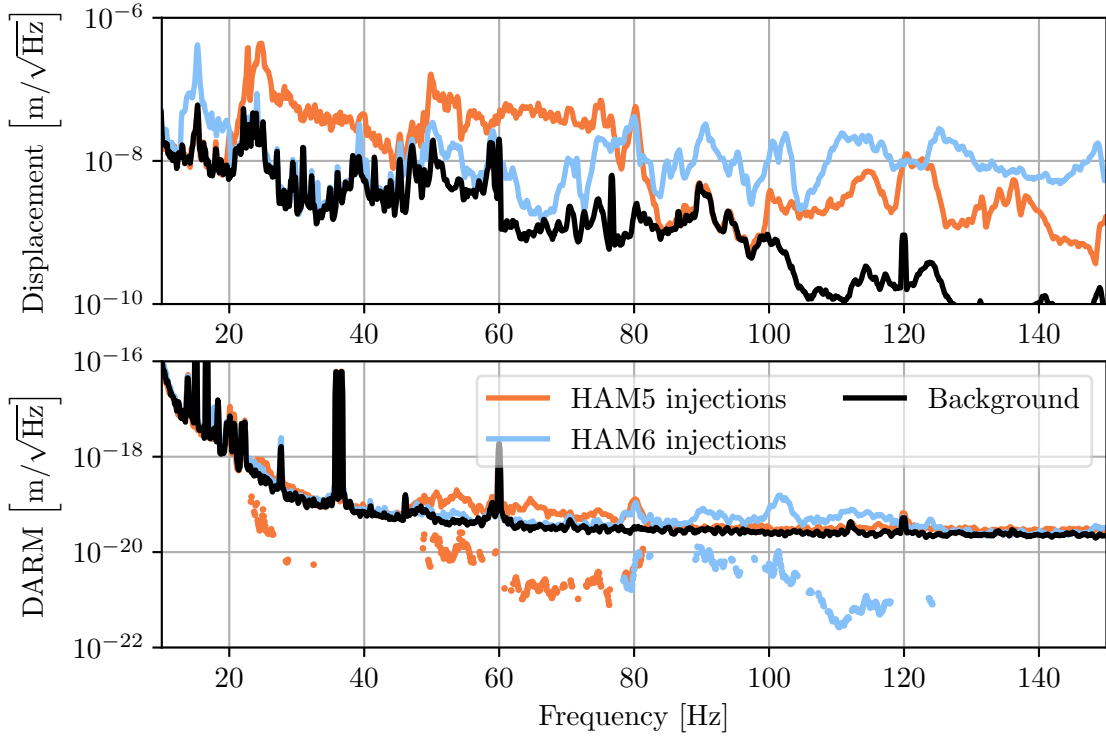


Figure 18. Spectra of shaker injections exciting scattered light noise at the LHO output arm. Top: Injections observed by the HAM5/6 septum accelerometer, stitched together from multiple bandpassed injections (each covering a 20-Hz range). Bottom: DARM responses to the injections (solid lines) and estimated ambients from coupling functions in dots.

(separating the HAM5 and HAM6 chambers) accelerometer signal matches the DARM signal most consistently. The accompanying spectrograms of the same impulse injection for DARM and the three sensors with the closest matching time-of-arrival to that of DARM reveal similarities between the frequency structure of the septum accelerometer signal and that of DARM.

Additionally, we performed a series of beating-shakers injections during the commissioning break as described in Section 4.2.1.1, attaching the large and small shakers to the HAM5/6 chamber doors, the outside of the septum itself, and the chamber roofs. We injected at 100, 200, and 400 Hz, each time with $\delta f = 100.01$ Hz

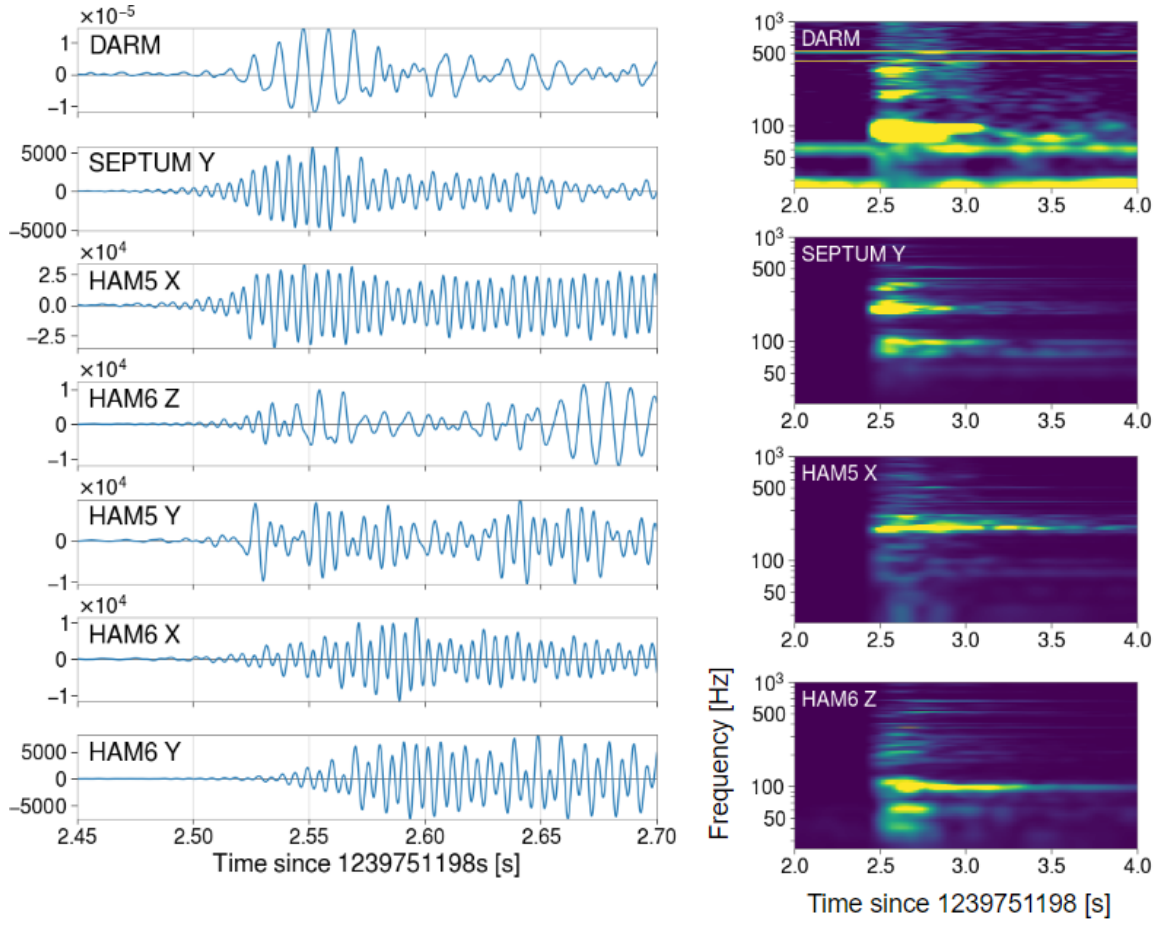


Figure 19. Time series (left) and spectrograms (right) of a vibrational impulse injection produced at the output arm of the LHO detector.

and observing for about five minutes. Due to a metal scaffolding structure placed around the chambers for commissioning work we were limited in our ability to produce strong enough signals to give a clear beat envelope. Nevertheless these injections did not rule out the septum as a coupling site.

The septum wall is a physically likely coupling site because it is highly reflective, exhibits more ambient motion than other surfaces on the HAM chambers, and stands perpendicular to the path of the interferometer beam, which passes through it via a glass window. This window was particularly suspected to be the culprit and was replaced during the commissioning break in order to eliminate

the scattered beam. Follow-up measurements, however, show no significant changes in the coupling between the start of O3 and the commissioning break (Figure 20), suggesting that perhaps the solid septum wall itself is the scattering surface.

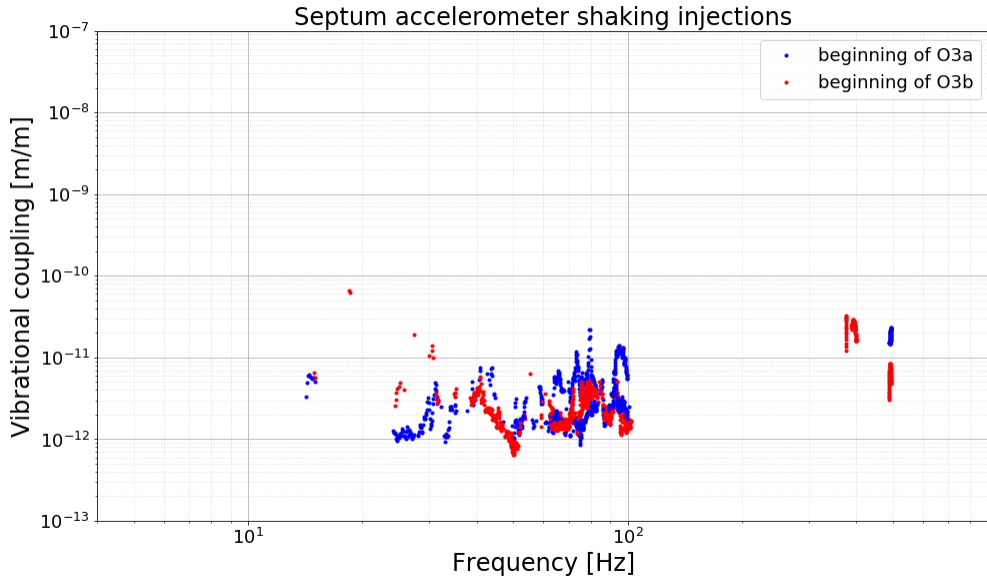


Figure 20. Change in HAM5/6 vibrational coupling before and after the replacement of the septum window.

The plan for post-O3 upgrades was to install light baffles, surfaces with low reflectivity, around the septum to block stray light from hitting the wall. More recent measurements suggest that even this has not mitigated coupling, however. This means that the window is indeed the coupling site but that a higher-quality window is not sufficient to eliminate the scattering, so the window must be entirely removed. This has been done at LLO with preliminary analyses showing significant noise reduction.

The investigation on the septum coupling will continue on the road towards O4. The results of this investigation and the vibrational noise budget measurements have made it clear that localizing and mitigating coupling due to

scattered light beams will be crucial to reaching the design sensitivity of Advanced LIGO.

5.2.2 Search for the source of a 48-Hz peak

During O3a, a 48-Hz peak with no known source was visible in the DARM spectrum. This peak often fluctuated in amplitude on the time scale of minutes. During the pre-O3 injections, we observed that this noise signal was amplified by many vibrational injections in the corner station, especially the input arm acoustic speaker injections (Figure 21). Follow-up impulse injections revealed that it was likely near the vertex, potentially pointing to a scattered light source in one of the beam splitter chambers or in HAM3.

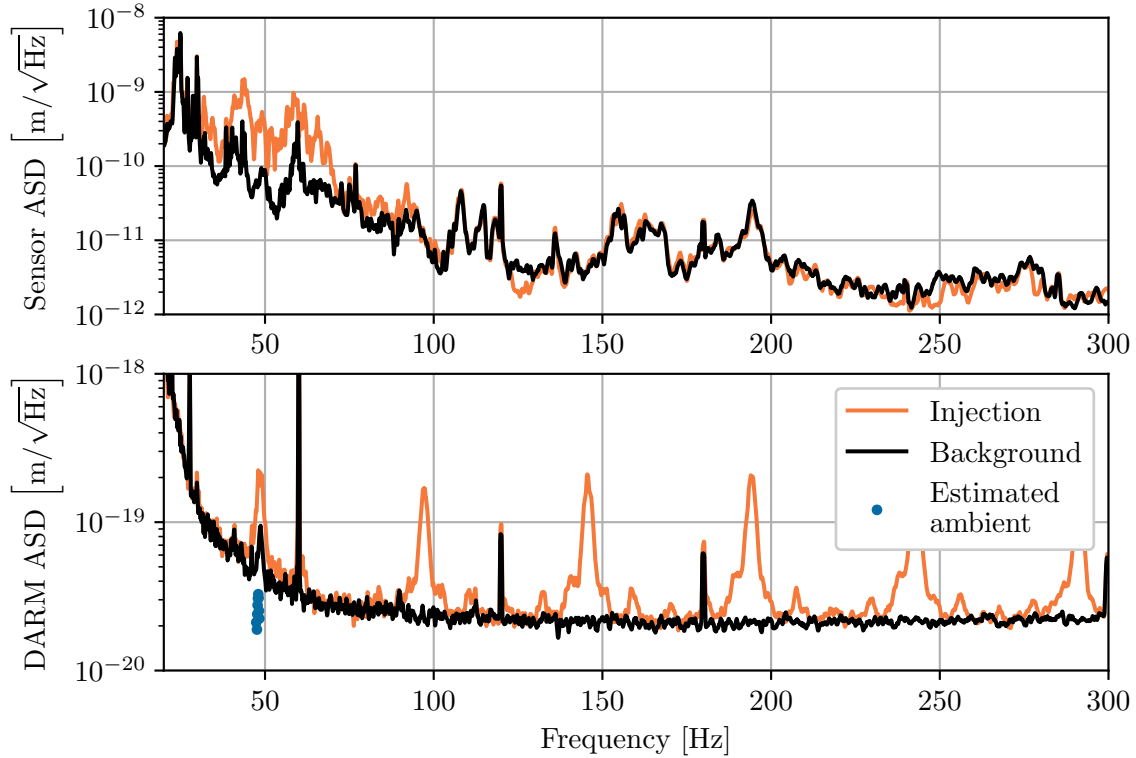


Figure 21. ASD of a vibrational injection at the LHO input arm exciting a 48-Hz resonance feature in DARM.

Beating-shakers injections were then used to localize the coupling site. The shakers were injecting from different locations near the input arm and vertex. One shaker injected at 48 Hz and the other at 48.01 Hz. Figure 22 shows spectrograms of the injection signals measured by DARM and by various nearby accelerometers. The Y-axes of the spectrograms are centered along at 48 Hz and show the combined signal in each sensor modulating at the beat frequency (0.01 Hz). This set of spectrograms suggests that the accelerometers on the ITM chambers and the Y-axis HAM2 accelerometer are likely not close to the true coupling location, since the beat envelopes have the greatest phase offset from the beat envelope in the DARM response.

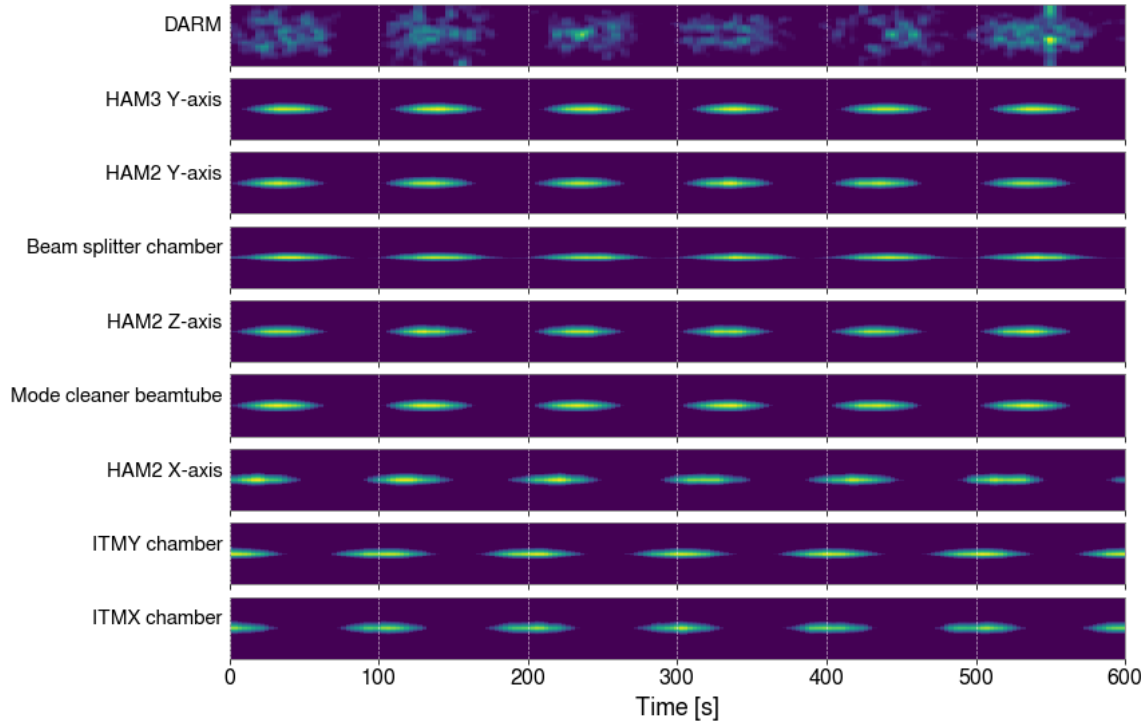


Figure 22. Spectrograms of DARM and various accelerometers near the input arm and beam splitter showing a beating-shakers injection at 48 Hz.

Multiple other injections were made (not shown here) with varying shaker locations in order to rule out other sensors until the most likely candidate

remaining was the HAM3 Y-axis accelerometer. Black glass was used to block scattered light at this location and the peak was eliminated for the second half of the O3 observation run.

5.2.3 Input beam jitter

Jitter noise was a dominant noise source for both detectors in the hundreds of Hertz frequency range. The impact was much greater at LHO than at LLO. Around 480 Hz, a peak associated with jitter noise could be seen in the LHO DARM spectrum. It was hypothesized that the higher coupling at LHO was due to a point absorber that was identified on the Y-arm ITM. Point absorbers are defects usually less than a millimeter across found in the test mass coatings. They are heated by the intense laser power in the Fabry-Pérot arm cavities, deforming the test mass and increasing the cavity optical loss. As discussed in Section 3.3, such defects enhance the coupling of jitter noise since they introduce an asymmetry between the arms.

In December 2020, the affected ITM was replaced with a new one, as part of the upgrades for O4. Thus far no point absorbers have been found on the new test mass. Jitter coupling functions measured some months later show a dramatic order-of-magnitude reduction compared to the O3 results (Figure 23). The ambient noise contribution is now roughly equivalent to that of LLO.

Although point absorbers can be avoided by offsetting the beam spot on the test mass, the only perfect solution is to completely change out the test mass. Therefore we these jitter coupling measurements emphasize the importance of addressing the issue of point absorbers as soon as possible. The existence of just one point absorber on any of the test masses enhances jitter coupling to the point

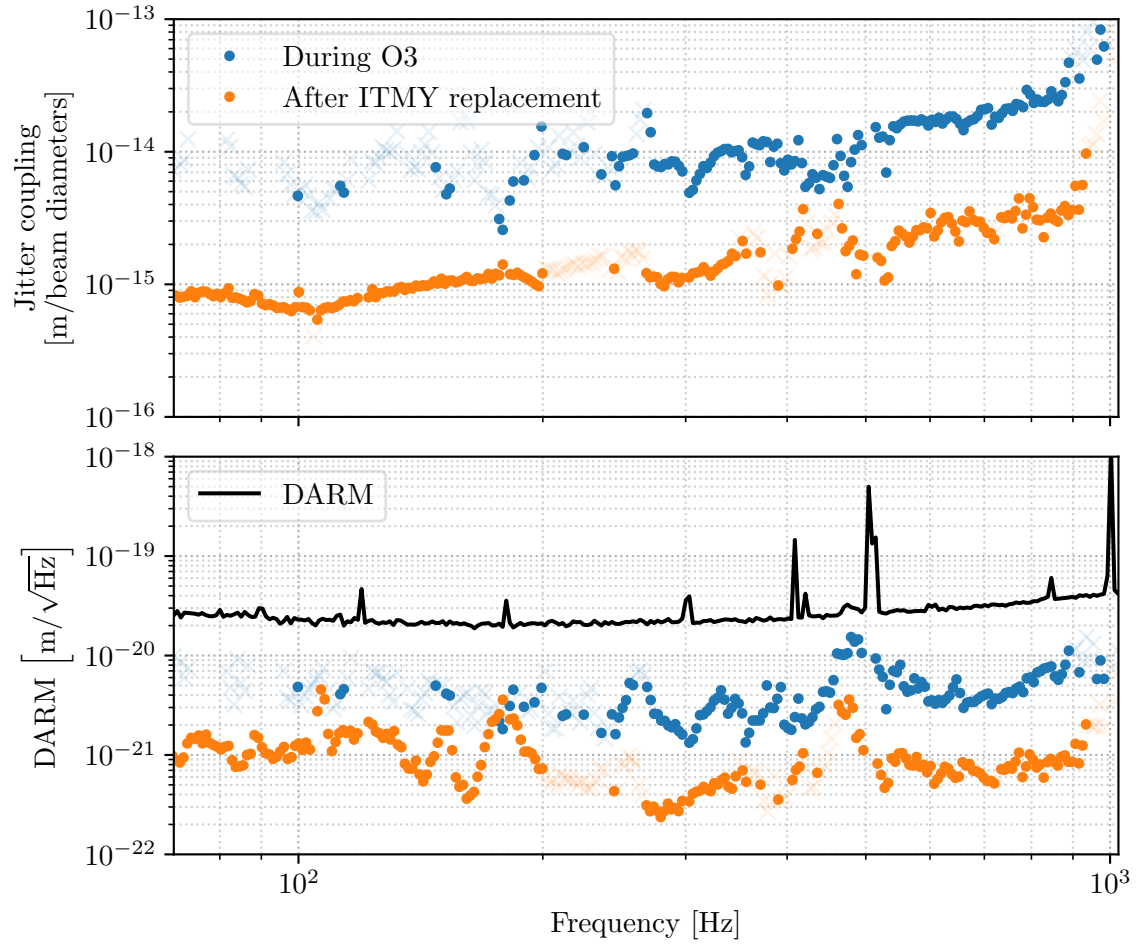


Figure 23. Improvement in jitter coupling at LHO after test mass replacement.

of introducing excess DARM noise, requiring that we new measurements every time some part of the input optics changes.

5.3 Magnetic noise studies during O3

Figure 24 shows the magnetic noise budget produced from coupling functions for all magnetometers for both LIGO observatories. Magnetic injections in previous runs suggested that coupling to permanent magnets in the suspension system could prevent LIGO from reaching design sensitivity in the 10-20 Hz regions (R. M. S. Schofield, 2013). While the test mass actuator is electrostatic

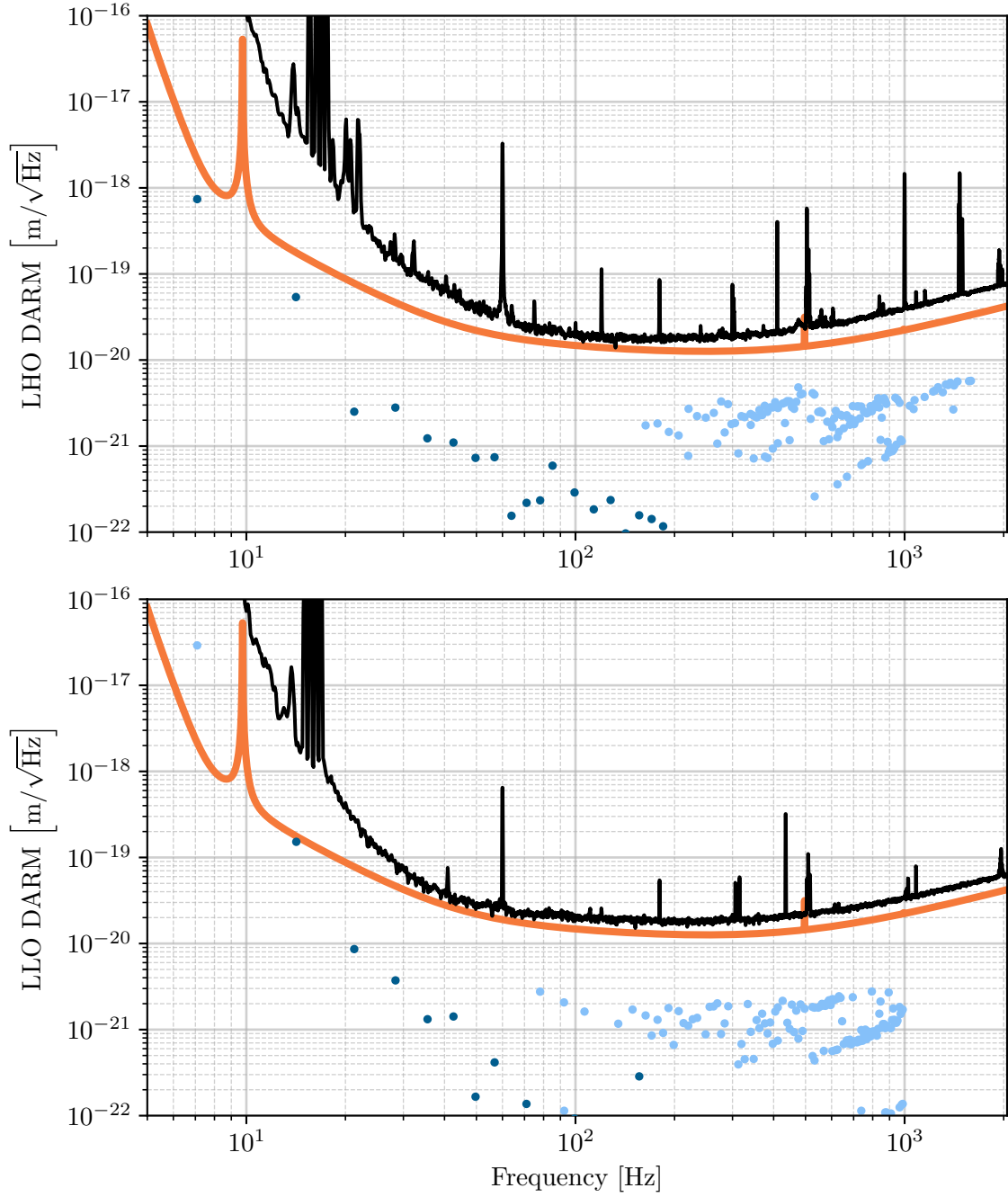


Figure 24. DARM noise from all *magnetic* coupling sources at LHO (top) and LLO (bottom). Dark blue dots represent measurements, while light blue dots represent upper limits. The black and orange curves show the O3 sensitivity and design sensitivity, respectively.

and not magnetic (as in iLIGO), a number of permanent magnets were used in the suspensions, including for actuation in the first three of the four levels of the isolation chain and for eddy current damping. The greatest number of permanent magnets were in the eddy current damping arrays and these were removed. Nevertheless, the current noise budget shows that ambient fields are still predicted to produce noise at a level close or even equal to the design sensitivity in the 10-20 Hz range (Figure 24). Thus low-frequency noise from permanent magnet coupling may need to be revisited in future runs.

At higher frequencies, generally above about 30 Hz, the dominant magnetic coupling appears to be through induction of currents in cables and at connectors, mainly to actuator cabling and other cabling in the control system. Mitigation of coupling to cables and connectors has required a continuing program of monitoring coupling since cables are often disconnected and reconnected during runs as electronics are replaced for problems or upgrades. This program consists of making weekly, broadband magnetic field injections using the large wall-mounted coils described in Section 4.2.2. Since the injections are scheduled for every Tuesday morning before the routine detector maintenance period, the interferometer may or may not be in a locked state at the time, so an injections were not always performed.

Figures 25, 26, and 27 are automatically generated every week by the code that analyzes the injections. The first of these shows magnetic coupling functions measured over the last five weeks for which a broadband injection was performed. At this point a single injector was implemented at each of the three stations at LHO; the coupling functions show the highest coupling per frequency bin between the three stations.

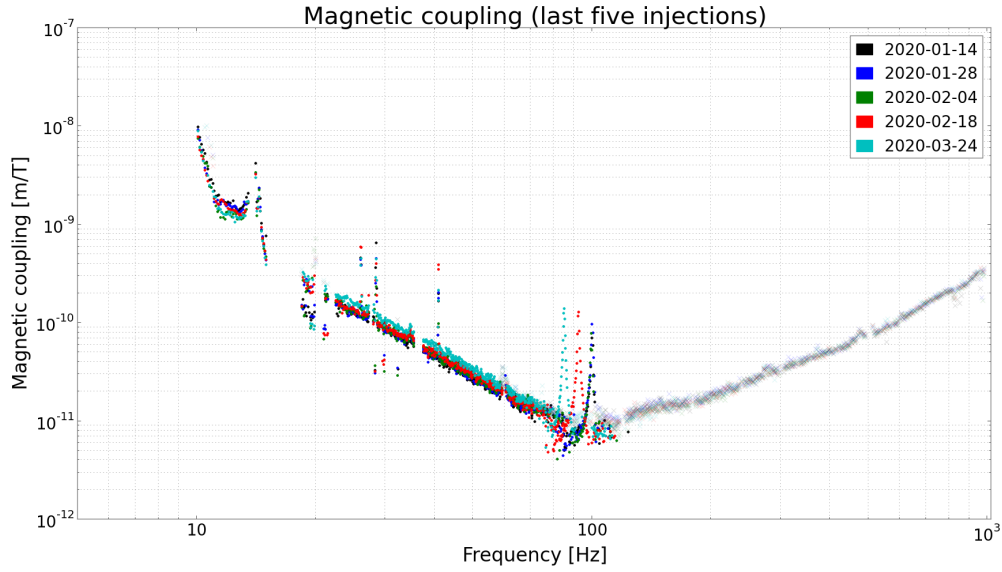


Figure 25. LHO magnetic coupling measured by the last five wall-mounted coil injections performed in O3.

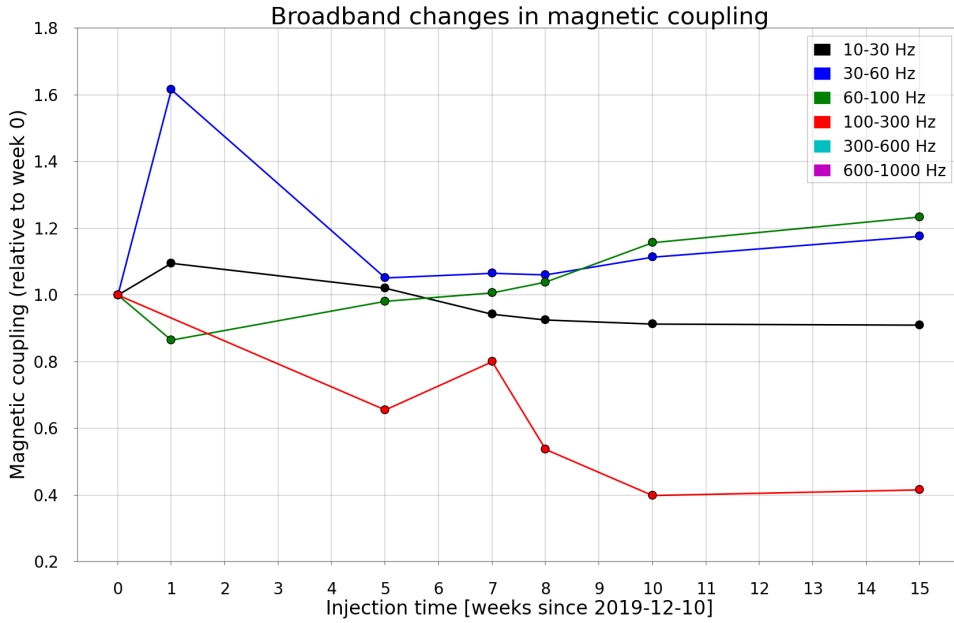


Figure 26. Time-lines of magnetic coupling changes relative to the start of the observing run.

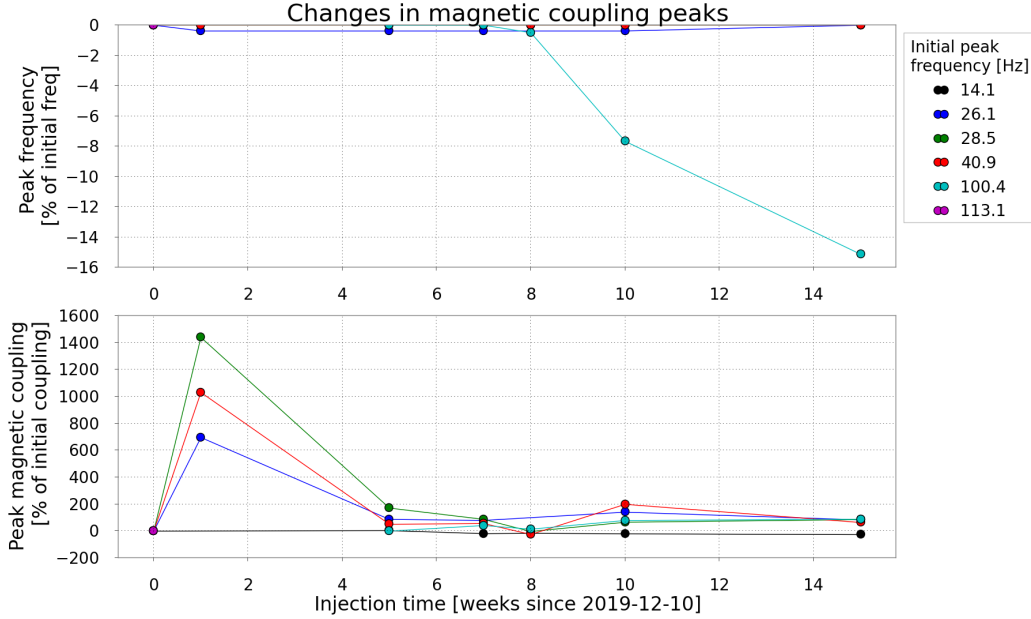


Figure 27. Weekly trends in frequency (top) and amplitude (bottom) of peaks in the magnetic coupling functions.

Changes can be seen in both the broadband and narrowband structure of the coupling function. Just within these five weeks, the level of broadband coupling varied by as much as a factor of about 1.5. Since the injection is produced from a same location and at the same amplitude every time, uncertainties due to the injection source as discussed in Section 4.4 do not account for these variations. Broadband changes over specific frequency ranges tracked over the full course of O3 (Figure 26) show significant fluctuations throughout the run.

Furthermore, a large peak in the coupling is seen migrating between 90 and 110 Hz. This is precisely the type of feature often missed by comb injections but will be routinely discovered by broadband injections in future observing runs. Figure 27 shows frequency and amplitude fluctuations in coupling peaks such as this. Although the coupling of the \sim 100 Hz peak is still well below the level that

would produce excess noise in the GW channel, its presence gives reason to be concerned that similar peaks could arise in the future that do couple significantly. These weekly injections would help in identifying when the coupling changed, so instrumentalists can deduce what changes to the electronics may have affected it.

5.4 Validation of gravitational wave event candidates

In addition to investigating sources of environmental influences, knowledge acquired from environmental studies contributes to the vetting of GW event candidates. Analysis pipelines search the strain data for astrophysical signals. They are categorized into modeled searches for binary mergers that match the data to template waveforms (e.g. GstLAL (Cannon et al., 2012) and PyCBC (Usman et al., 2016)) and unmodeled searches that identify excess energy coherent between multiple detectors (e.g. cWB (Klimenko, Yakushin, Mercer, & Mitselmakher, 2008), oLIB (Lynch, Vitale, Essick, Katsavounidis, & Robinet, 2017), and BW (Cornish & Littenberg, 2015)).

The template-based modeled searches are incredibly robust to noise transients. However, environmental noise has the potential to be correlated between detectors by stemming from a common source, such as through electromagnetic signals from distant sources or glitches in GPS-correlated electronics. The analysis pipelines estimate the false-alarm probabilities for GW events based on the background rate of randomly coincident events in the detector network. They generate background events by time-shifting the data stream of one detector relative to another by time steps much longer than the light travel time between detectors and longer than the duration of GW signals. This method does not

account for the possibility of transients being correlated between the detectors due to a common environmental source.

Environmental noise is also particularly relevant to unmodeled searches. Unlike template-based methods, these searches make minimal assumptions about the signal waveform and rely more heavily on signal correlation between sites. They are therefore more likely to pick up chance coincidences of environmental transients of various time-frequency morphology.

Furthermore, even if an environmental signal does not account for excess noise in the strain channel during a GW event, it may still impact parameter estimation analyses that infer properties of the GW source. Most GW events are short in duration, meaning that any chance overlap between an astrophysical signal and a noise artifact, although quite rare, would have a significant impact on these analyses. In O3, many parameter estimation analyses of GW detections had to limit their frequency ranges to avoid contamination from effects such as scattered light noise.

5.4.1 Past methods

The first observation of a GW occurred on 14 Sept 2015 (B. P. Abbott et al., 2016b). The event, a short-duration binary black hole merger designated GW150914, required a number of follow-up investigations to find potential noise sources around the time of the event (B. P. Abbott et al., 2016a). This included an examination of the status of all PEM sensors and any significant signals they observed for possible contamination of the GW signal (R. M. S. Schofield, Roma, et al., 2018). A few of the PEM sensors were not working, but because of redundancy, coverage was sufficient.

Comparisons between constant-Q transform spectrograms (Chatterji, Blackburn, Martin, & Katsavounidis, 2004) of all coincident events in environmental sensors to the time-frequency path of the event revealed that no environmental signals had paths similar to the event candidate. Q-transforms produce a quality-factor-optimized logarithmic tiling of the time-frequency space, making them useful for visualizing transients. The SNRs of the matching signals were also compared to that of the event, showing that even if there were overlapping time-frequency paths, none of the environmental signals were large enough to influence the strain data at the SNR level of the event, based on multiplying the environmental signals by their respective sensor coupling functions.

The validation process for novel events such as GW150914 also includes redundant checks for global sources of environmental noise. We use a dedicated cosmic ray detector located below an input test mass at LHO to examine any association of cosmic ray showers to excess noise in DARM. We also check external observatories for coronal mass ejections, solar radio signals, geomagnetic signals, and radio-frequency (RF) signals in the detection band as well as higher frequencies.

There was specific concern over a co-incident extremely-high current (504 kA) lightning strike over Burkina Faso, prompting additional studies of the effects of lightning on the interferometer (R. M. S. Schofield, 2018). Investigations of similar strikes found no effect on the strain data and investigations of closer strikes confirmed that the magnetometers were much more sensitive to lightning strikes than the interferometer was. In conclusion there was no reason to veto the first detection based on environmental disturbances.

Subsequent detections throughout O1 and O2 employed a similar procedure; however the development of the method described in Section 4.3 for producing coupling functions for all sensors expedited the process. This was especially important for examining environmental noise during GW170817, the first long-duration event detected by LIGO (Abbott et al., 2017a; R. M. S. Schofield, Nguyen, et al., 2018). The longer duration of this event (75 s) unsurprisingly overlapped with many environmental signals. Based on the coupling functions for those sensors, several of these environmental events were loud enough (estimated DARM signals of up to SNR 4) to have contributed to the interferometer readout, but not enough to account for the GW signal. Furthermore, none of them had a time-frequency morphology that correlated with any features in the candidate signal.

5.4.2 Automated validation of O3 events

Since the start of O3, most of the procedure described above has been automated in order to handle the increase in detection rate. The automated vetting is performed by the `pemcheck` routine, which is a part of the Data Quality Report (DQR). When an event is detected by the astrophysical search pipelines, a DQR is initiated and assembles a plethora of tasks for assessing the data quality at each observatory during the time of the event. Among these tasks, an *omega scan pipeline* (Chatterji et al., 2004; Davis et al., 2021b) is used to search for transient noise in all PEM sensors in the time window spanning the event candidate. It does so by producing a Q-transform for each sensor and reporting those in which there is a transient signal with a false-alarm rate below 10^{-3} Hz. The omega scan also reports the frequency and amplitude of the most significant tile for each sensor. The `pemcheck` in O3 used the output of the omega scan to estimate each

sensor's potential affect on the data quality of the detector. The coupling function of each sensor was interpolated at the peak frequency and multiplied by the peak amplitude, producing an estimated DARM amplitude.

Sensors whose estimated contribution exceed one tenth of the DARM background level were flagged for human input, requiring a comparison of the environmental signal morphology to that of the event candidate. If there was sufficient signal overlap, reviewers may advise that analysts perform some noise removal in the data, such as by gating or filtering out the appropriate time or frequency range, before performing further follow up analyses. The event could be retracted, if gating or filtering out the environmental contribution would reduce the signal-to-noise ratio of the candidate to a level no longer consistent with a GW detection.

To confirm that PEM sensor coverage was sufficient to make a confident statement regarding environmental contamination, an additional DQR task checked for the most recent output from `ligocam`, described in Section 4.1.1. This task was used as a supplement to the results reported by `pemcheck`.

During O3, we confirmed that environmental noise did not account for any of the 74 GW events detected (Abbott et al., 2021b, 2021c). Some excess noise was always estimated to potentially exist around the events due to the conservative upper limits we set for our coupling functions, but no signal overlap of any environmental transients with GW candidates was seen even for those worst-case upper limit projections. That said, for most events we cannot rule out the possibility of environmental noise affecting parameter estimation pipelines.

5.4.3 Science Case Study of S200114f

On January 14, 2020, the coherent waveburst (cWB) pipeline (Abbott et al., 2022) reported a GW trigger S200114f that was not associated with any triggers from a template-based search pipeline. It was the highest significance event detected by an unmodeled search alone. Since this meant the possibility of a non-merger source, a science case study team was put together by the LIGO collaboration to assess the astrophysical nature of the trigger. Of particular interest was the existence of environmental noise observed by some accelerometers at the LHO output arm. This was a known source of noise, associated with fan located on the squeezer optics table by HAM6. Ambient fan motion does not produce noticeable transient signals, but changes in the fan speed cause a vibrational impulse that is much louder than the ambient motion. In this case a change in the fan speed right at the time of S200114f, producing a second-long glitch at the fan speed of 76 Hz and at several of its harmonics. Although the higher harmonics produced more noise, the fundamental frequency was very close to the central frequency of the GW trigger, prompting suspicion that it may have accounted for or at least contributed to the signal SNR.

The nearest sensor observing this noise was an accelerometer mounted on the squeezer table itself. Table accelerometers are relatively isolated from most acoustic and vibrational injections made at the beginning of an observing run, so only upper limits were available for making initial noise projections. Follow-up injections were performed soon after that provided much better coverage, and the updated noise projections showed that the expected noise in the strain channel was about an order of magnitude below background levels. This rejects the possibility that the environmental transient accounts for the LHO detection of S200114f, since

the trigger has a significant SNR. However, the estimated projection for the 152 Hz harmonic was only a factor of two below background, so we could not rule out the impact of this noise on any parameter estimation that might be attempted on the full cWB signal.

5.4.4 Event validation in O4

With the GW detection rate expected to increase in O4, a more sophisticated and streamlined vetting routine is necessary. The DQR in O4 will report a p-value for each vetting task, including the pemcheck task. In the case of environmental noise vetting, this p-value represents the null-hypothesis probability, i.e. the probability that environmental disturbances are not contaminating the GW event signal. This probability is defined based on the uncertainty of the coupling functions.

Suppose we have measured the coupling for a sensor at a single frequency bin, $C(f_k)$. As we know systematic uncertainties result in coupling measurements to be log-normally distributed (see Section 4.4.3), we can describe the true coupling with a log-normal distribution with mean $\ln C(f_k)$ and standard deviation $\ln 2$ (corresponding to a factor two uncertainty). If only an upper limit is available, then the coupling must be equal to or less than the upper limit, so it can be described by a uniform probability distribution between 0 and the upper limit. Thus multiplying these distributions by the sensor ambient we get a probability distribution for the projected noise level $h_p(f_k)$ in the GW channel in terms of $\mu = C(f_k) \cdot X(f_k)$:

$$P(h_p) = \frac{1}{h_p \sqrt{2\pi} (\ln 2)^2} \exp \left[-\frac{\ln h_p - (\ln \mu)^2}{2(\ln 2)^2} \right] \quad (5.1)$$

for measurements and

$$P(h_p) = \begin{cases} \frac{1}{CX} & \text{if } x < CX \\ 0 & \text{otherwise} \end{cases} \quad (5.2)$$

for upper limits.

We can write the probability that the projected noise actually exceeds some GW channel background level $h_{\text{bkg}}(f_k)$ based on the corresponding cumulative distribution functions:

$$P(h_p > h_{\text{bkg}}) = \begin{cases} 1 - \frac{1}{2} \left[\text{erf} \left(\frac{\ln h_p - \ln \mu}{\sqrt{2} \ln 2} \right) \right] & \text{(measurement)} \\ 1 - \min(1, \frac{h_p}{\mu}), & \text{(upper limit)} \end{cases} \quad (5.3)$$

This is computed for every time-frequency pixel of a spectrogram, producing a probability spectrogram image that shows how likely there is to be excess noise within each pixel. We can then search for the highest probability within pixels that overlap a GW transient in order to report the probability that environmental noise in the vicinity of the PEM sensor is contaminating the signal of interest. This algorithm is run on every PEM sensor with an available coupling function and the highest probability among all sensors is reported. We report the p-value of consistency with the null hypothesis as one minus the highest probability, so if a low p-value ($\lesssim 0.1$) is reported for a GW event candidate then we cannot rule out the possibility of excess noise contributing to the GW data.

Figure 28 provides an example of a probability spectrogram output by pemcheck for an O3 GW event candidate, S190510g. The candidate signal coincides with scattering noise produced at the LLO Y-end station by a thunderstorm. The coupling projection predicts a peak probability of 0.95, meaning

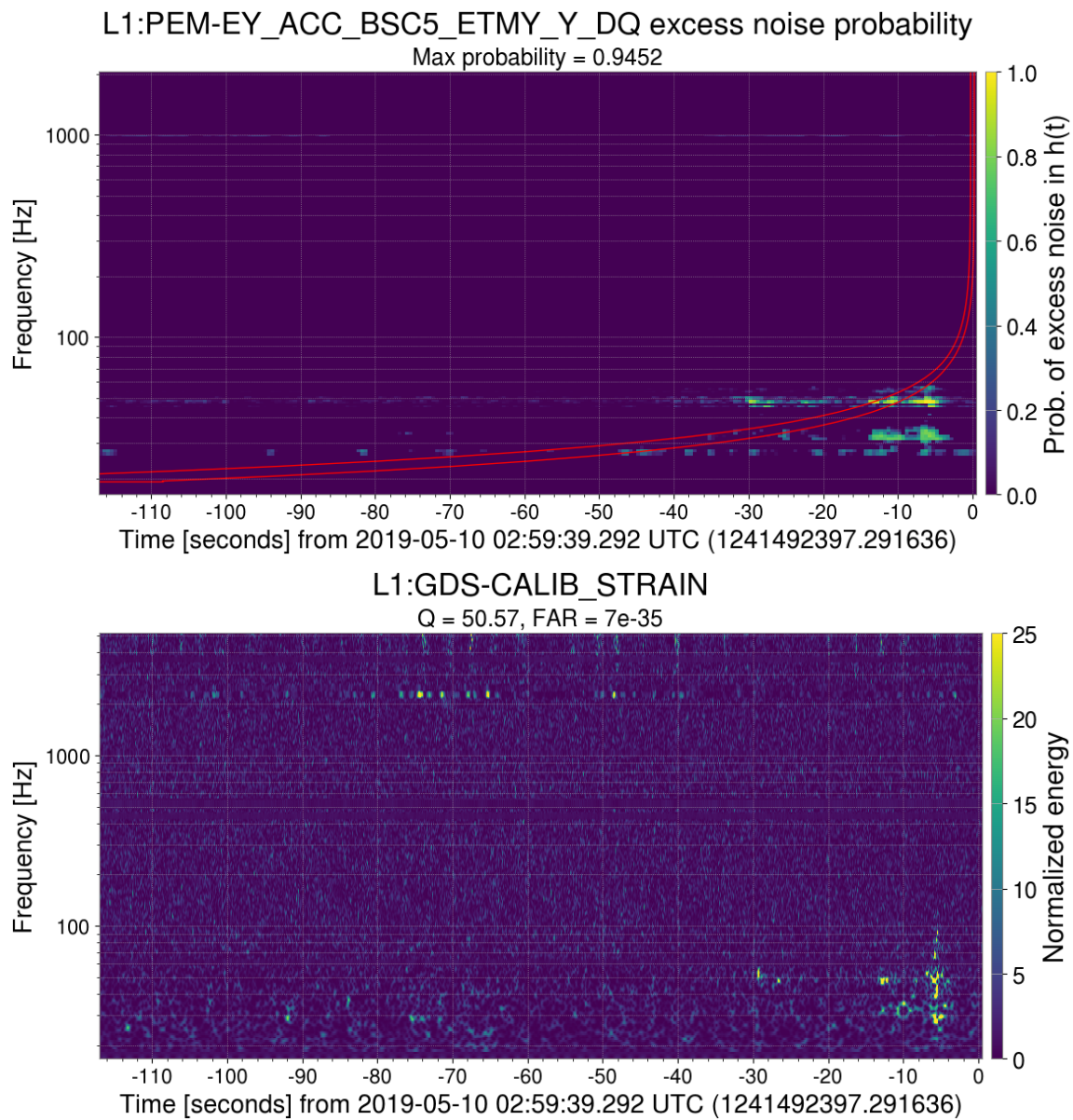


Figure 28. Probability spectrogram of an ETMY accelerometer at LLO (top) and a constant-Q transform of the GW strain channel (bottom). The red lines show the time-frequency path of GW event candidate S190510g.

there is an 95% probability that noise is present in the interferometer overlapping the time-frequency window of the GW event.

There are still limitations to how well this method can predict the presence of excess noise in the GW channel, discussed below.

5.4.4.1 *Coupling function tuning.* Coupling function projections often overestimate the GW background level for a number of reasons. The most common causes are all linked to the fact that coupling functions can only be measured during extended periods of detector maintenance, usually at the start of an observing run, leaving them vulnerable to becoming outdated as noise sources are introduced, changed, or mitigated. If a noise source is introduced near a sensor, such as through the installation of new hardware, the sensor ambient can increase dramatically whether or not the noise source actually couples to the GW channel. If the new noise does not couple, then the projection overestimates the detector amplitude, leading to a spurious claim that a GW candidate signal may be affected by environmental noise. Conversely, if an existing noise source is removed or its coupling mechanism mitigated, then the GW background drops, potentially below the level of estimated ambient noise projections.

For these reasons, coupling functions must be tuned to account for overestimated noise in the time around an event candidate. This is done by simply treating background noise in a long stretch of time before the candidate as if it were a new injection. Rather than re-measuring the coupling function, we can check for frequencies where projections estimate ambient coupling to exceed the GW background, dividing the coupling function by the ratio by which it is overestimating. The result is a coupling function that at most projects noise at background levels.

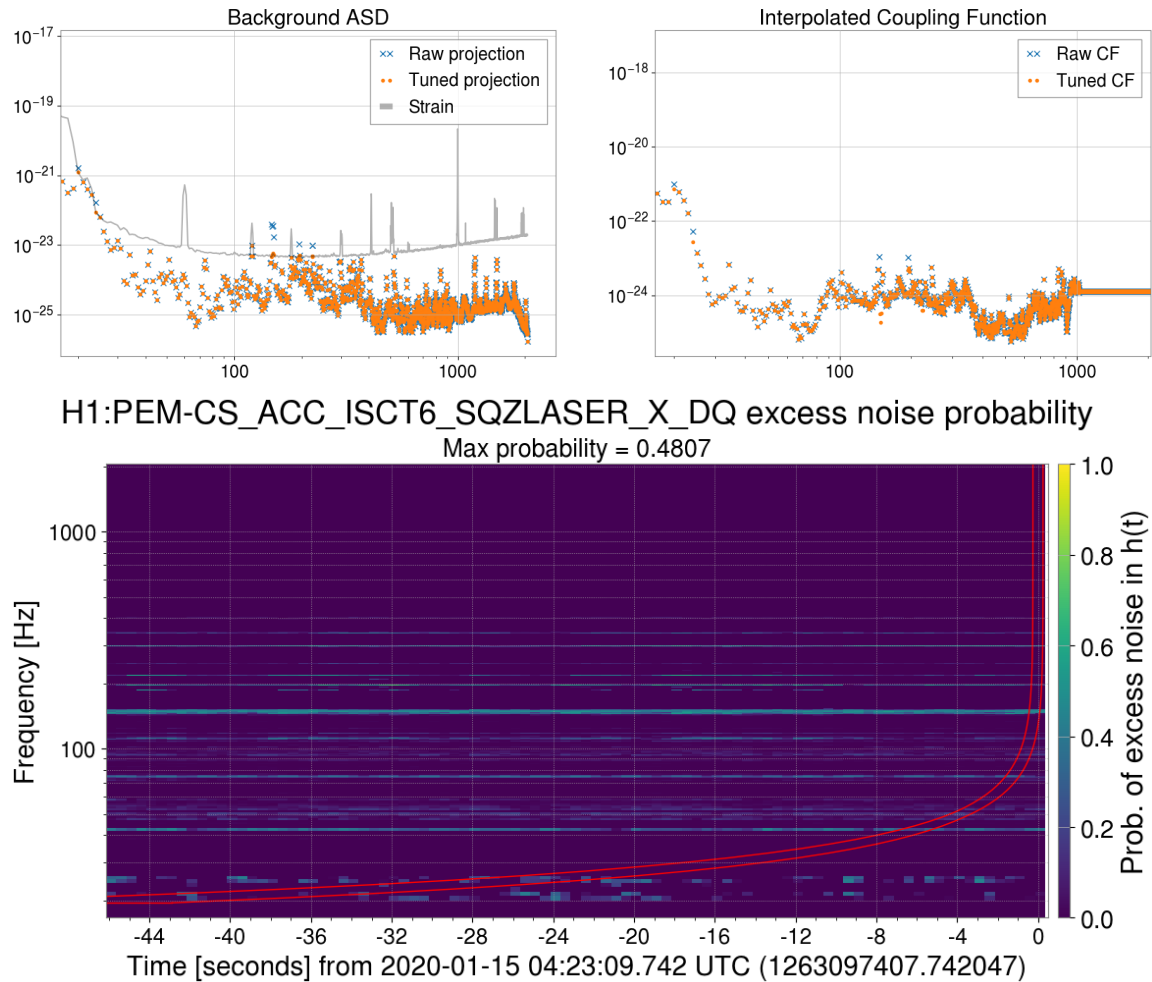


Figure 29. Coupling function tuning (top) and the resulting probability spectrogram (bottom).

Figure 29 shows an egregious case of projected noise for an accelerometer on the squeezed light optics table overestimating the strain background amplitude. The tuning reduces this to match the strain background, and the resulting probability spectrogram does not estimate a significant probability that excess noise is present.

5.4.4.2 Grouping nearby sensors. Even after tuning coupling functions, projections can still be overestimated in the presence of short duration (≤ 1 s) transients that are not likely to couple based on physical reasons. Rack magnetometers (placed on the metal racks that hold the various control systems, data acquisitions systems, and power supplies in the electronics rooms) observe the highest rates of localized short-duration transients, routinely picking up magnetic fields from changes in nearby currents. When these glitches coincide with a GW event candidate they predict a probability of excess noise usually above 90%. Although the coincident rate is low for typical (BBH) events, a long-duration GW signal such as a BNS will typically overlap with at least a few electronics glitches.

Since coupling functions are only intended to be used for noise sources distant from the sensors, projections from sensors placed close to each other ($\lesssim 1$ m) should be highly correlated if the input noise is environmental and not local to the individual sensors. To incorporate this knowledge, `pemcheck` groups together magnetometers in each electronics room; their probability spectrograms are stacked and a pixel-wise minimum is computed to generate a combined group spectrogram. This suppresses signals that project above the strain background in one magnetometer but not the others, so the projected excess noise probabilities are much lower than any of the peak probabilities reported by the individual sensors.

CHAPTER VI

GRAVITATIONAL WAVES ASSOCIATED WITH GAMMA-RAY BURSTS

6.1 GW searches

The LIGO-Virgo collaboration searches for gravitational waves associated with GRBs detected by Fermi GBM and Swift Burst Alert Telescope (BAT) using two analyses: a template-based matched-filter search using the `pyGRB` pipeline and a generic transient search using `x-pipeline` (Abbott et al., 2021b, 2022). The GRBs are classified as short if $T_{90} + |\delta T_{90}| < 2$ s, long if $T_{90} - |\delta T_{90}| > 4$ s, and ambiguous if they lie in between. The `pyGRB` pipeline is used for analyzing short and ambiguous GRBs, while `x-pipeline` is used for all GRBs, short, ambiguous or long. This does not account for short GRBs that are followed by periods of extended emission, for which measures of T_{90} may substantially exceed these thresholds. For more robust classification one must also consider spectral properties, most commonly the spectral hardness or peak energy of the event, but since our sample consists of observations from multiple observatories with different spectral sensitivities we do not employ such quantities when organizing our sample. The GRBs sample for a LIGO-Virgo observing run is collected from the Fermi and Swift GRB catalogs, and the best sky localization and timing information is used.

6.1.1 X-Pipeline

One of the analyses searching for GWs associated with GRBs uses the generic transient search library `x-pipeline` (Sutton et al., 2010). This pipeline analyzes GW strain data from multiple observatories around the time of a GRB. This is an unmodeled method for finding GWs, as it does not rely on template-based matched-filtering. Instead, given a GRB event, `x-pipeline` searches for

excess power coherent between LIGO-Virgo detectors and consistent with the sky localization and time window of the GRB. The search time window starts 600 s before the GRB trigger time and ends at 60 s after trigger time, or at T_{90} if $T_{90} > 60$ s. This is sufficient to cover the time delay between GW emission from a progenitor and any GRB prompt emission (Aloy, Müller, Ibáñez, Martí, & MacFadyen, 2000; Burlon, Ghirlanda, Ghisellini, Greiner, & Celotti, 2009; Burlon et al., 2008; Koshut et al., 1995; Lazzati, 2005; Lazzati, Morsony, & Begelman, 2009; MacFadyen, Woosley, & Heger, 2001; Vedrenne & Atteia, 2009; Wang & Mészáros, 2007; Zhang, Woosley, & MacFadyen, 2003). While some GW emissions, such as from CCSN, are expected to reach frequencies up to a few kilohertz (Radice, Morozova, Burrows, Vartanyan, & Nagakura, 2019), we restrict our search frequency range to the most sensitive band of the GW detectors, 20–500 Hz, since detecting such signals above a few hundred hertz requires extremely high GW energies (Abbott et al., 2019) and expanding the frequency range would also significantly increase the computational cost. To constrain the sky location of the GRB event, the search uses a grid based on the best localization known either from Fermi GBM or Swift BAT.

Since x-pipeline is an unmodeled search, it primarily relies on coherence between detectors to determine the significance of a GW signal. To do this, it combines the data from multiple detectors. For a network of detectors, the data measured by a set of D detectors is

$$\mathbf{d} = \mathbf{F}\mathbf{h} + \mathbf{n} \quad (6.1)$$

where each component of the vectors \mathbf{d} and \mathbf{n} is the Fourier-transformed output of a detector and its noise, respectively,

$$\mathbf{h} = \begin{pmatrix} h_+ \\ h_\times \end{pmatrix} \quad (6.2)$$

represents the plus and cross polarizations of the GW signal, and $\mathbf{F} = [\mathbf{F}_+ \ \mathbf{F}_\times]$ is a matrix whose rows represent the antenna response of each detector to the plus and cross polarizations of the GW signal, respectively. These matrix components are dependent on the sky location of interest, e.g. of a GRB trigger. The components of \mathbf{d} , \mathbf{n} , and \mathbf{F} are noise-spectrum-weighted, i.e. the raw value is divided by the one-sided noise power spectral density of the detector, such that \mathbf{n} is normalized. We refer to the noise-spectrum-weighted \mathbf{d} as the energy measured in the detector. We define the *standard likelihood energy*

$$E_{\text{SL}} \equiv \sum_k^D \mathbf{d}^\dagger P^{\text{GW}} \mathbf{d} \quad (6.3)$$

where $P^{\text{GW}} \equiv \mathbf{F}(\mathbf{F}^\dagger \mathbf{F})^{-1} \mathbf{F} \mathbf{F}^\dagger$ is a projection operator that projects the data into the subspace spanned by the antenna response vectors \mathbf{F}_+ and \mathbf{F}_\times .

To identify signals, x-pipeline Fourier transforms the individual detector streams over many time windows to produce time-frequency maps where each pixel represents the energy d_k of detector k for a particular time and frequency. These maps give access to the temporal evolution of the spectral properties of the signal. They are combined over the detector network via eq. (6.3) to form a single map of pixels representing the standard likelihood energy. Clusters are identified by selecting the 1% of pixels with the highest standard likelihood energies

and grouping together adjacent selected pixels. Each cluster is assigned an overall detection statistic which is the sum of the standard likelihood energies of its pixels, and the cluster with the largest statistic is the best candidate for a GW detection.

The significance of a candidate is determined based on the probability of the event being produced by the background alone. The data around the GRB trigger is divided into a 660 s *on-source* segment and many equally-long *off-source* segments before and after the on-source. The candidate significance is determined by comparing the SNR of the trigger within the on-source segment to the distribution of the SNRs of the loudest triggers in the off-source segments. As a requirement, the off-source segments are drawn from at least at least ~ 1.5 hr of coincident data from at least two detectors around the time of a GRB. This is small enough to select data where the detectors should be in a similar state of operation as during the GRB on-source segment, and large enough so that statistical errors using artificial time-shifting of the data are at the sub-percent level.

We quantify the sensitivity of the generic transient search by injecting simulated signals into off-source data. For each waveform family injected we determine the largest significance of any surviving cluster associated with the injections. We compute the percentage of injections that have a significance higher than the best event candidate and look for the amplitude at which this percentage is above 90%, which sets the upper limit. We include O3b calibration errors (Acernese et al., 2022; Sun et al., 2021) by jittering the amplitude and arrival time according to a Gaussian distribution representative of the calibration uncertainties. These injection sets allow us to calculate the 90% exclusion distance, D_{90} , for each injection waveform. These D_{90} estimates represent the distance within

which our null result is 90% likely to exclude the existence of a GW signal caused by the emission mechanism for that waveform.

We choose simulated waveforms to cover the search parameter space of three distinct sets of circularly polarized GW waveforms: BNS and NSBH binary inspiral signals, stellar collapse signals, and disk instability signals.

Circular sine-Gaussian (CSG) injections represent GW emission from stellar collapses defined in Equation (1) of Abbott et al. (2017) with a Q factor of 9 and varying center frequency of 70, 100, 150, and 300 Hz. In all cases, we assume an optimistic emission of energy in GWs of $E_{\text{GW}} = 10^{-2}M_{\odot}c^2$. This set of waveforms closely represents a number of emission models for short-duration GWs occurring during the collapse of the star.

Binary inspiral injections are chirp-like waveforms (similar to that of GW170817 as seen in Figure 1, top left). They are generated based on masses sampled from a Gaussian distribution centered at $1.4 M_{\odot}$, with a width of $0.2 M_{\odot}$ for an NS in a BNS merger, and with a width of $0.4 M_{\odot}$ for an NS in an NSBH merger. The distribution for GWs emitted by BNS mergers addresses the case of short GRB events as in Abbott et al. (2017) and adopted in the pyGRB search.

Long-duration accretion disk instability (ADI) injections are used to represent GWs produced by instabilities in the magnetically suspended torus around a rapidly spinning BH formed by a massive core-collapsing star, as described in Section 2.4.2 (M. H. van Putten, 2001; van Putten et al., 2004). Although the quadrupole mass moments within the torus can take on many forms, the waveforms used for the x-pipeline search are based on an approximation in which two overdense regions are formed on opposite sides of the torus and extract angular momentum from the central BH until the BH is no longer spinning, after

which the lumps disperse and the torus returns to stability (Santamaría & Ott, 2013). The spin-down produces GWs following a downwards-sweeping signal, different from the chirp that would be seen if the binary was simply spiraling inwards (Figure 30).

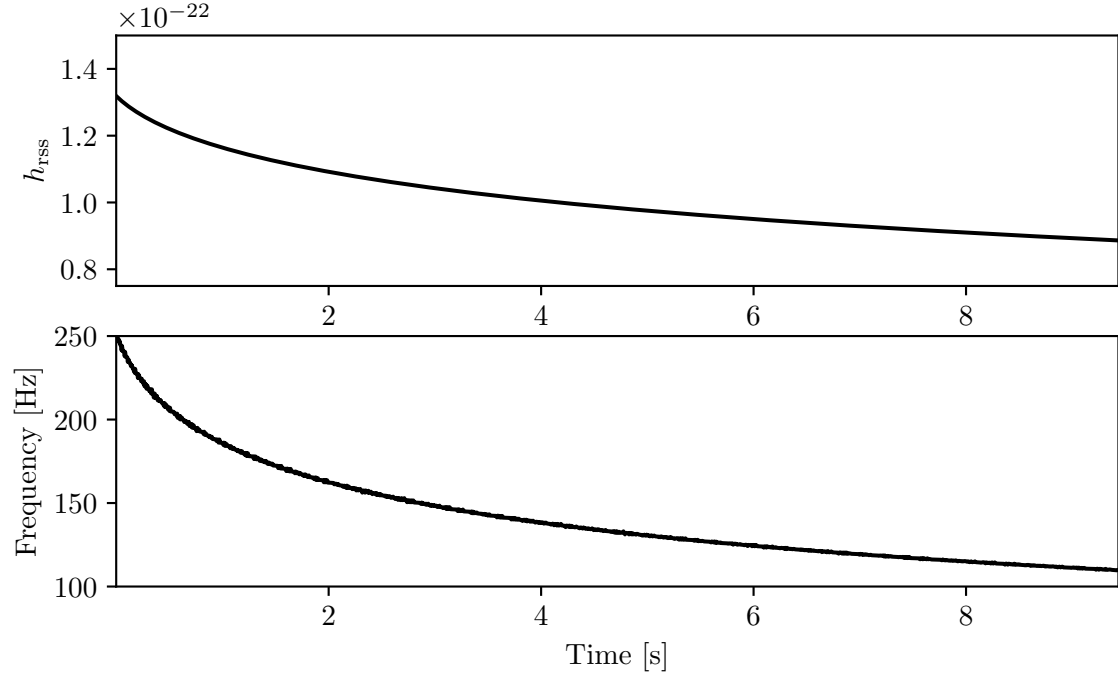


Figure 30. Example waveform of a ADI-B injection at 100 Mpc. Parameters are given in Table 4.

The ADI waveforms are parameterized by the mass M and dimensionless spin parameter χ of the central BH, and the fraction ϵ of the accretion disk mass (which is fixed at $1.5 M_\odot$) that forms into lumps. The parameters used to generate the five families of ADI signals are shown in Table 4, along with the duration, frequency, and E_{GW} of each waveform.

Table 4. Parameters and properties for accretion disk instability waveform injections.

Waveform Label	$M (M_{\odot})$	χ	ϵ	Duration (s)	Frequency (Hz)	$E_{\text{GW}} (M_{\odot}c^2)$
ADI-A	5	0.30	0.050	39	135–166	0.02
ADI-B	10	0.95	0.200	9	110–209	0.22
ADI-C	10	0.95	0.040	236	130–251	0.25
ADI-D	3	0.70	0.035	142	119–173	0.02
ADI-E	8	0.99	0.065	76	111–234	0.17

6.1.2 Vetoing noise signals

Combining the detector data streams coherently does not guarantee that chance coincidences between noise transients in the individual detectors cannot happen. Before combining the data, *data quality* (DQ) vetoes are applied to the single-detector signals. DQ vetoes are observation periods flagged as problematic for various reasons. Each detector has its own set of DQ vetoes, which are separated into different categories (Davis et al., 2021a, 2021b). Category 1 DQ vetoes represent times during which detectors were not operating in their nominal state. Many of these times correspond to large machines like forklifts and cranes being operated, for example. Category 2 vetoes indicate periods where excess noise likely to be caused by known instrumental effects is present. Examples from O3 include periodic 70 Hz glitches caused by vibrations of a camera shutter at the LLO End-Y station, thunder noise identified by microphones at LLO during storms, and large earthquakes at LHO. Category 3 flags are based on statistical correlations with auxiliary sensors. Category 4 flags indicate times when hardware injections (signals intentionally generated in the interferometer to test search analyses or quantify correlations between the GW channel and auxiliary channels) were being performed. The x-pipeline search completely removes times flagged by Category

1 vetoes before performing any analysis. Category 2 and 4 flags are applied to the single-detector data streams prior to combining them.

After generating the coherent energy data stream and ranking the time-frequency pixel clusters, another step is taken by x-pipeline to further deal with non-astrophysical transients. A coherent consistency test vetoes clusters based on the *null energy* stream that is the difference between the total energy in the data $E_{\text{tot}} = \sum_k \|d\|^2$ and the standard likelihood energy defined in eq. (6.3):

$$E_{\text{null}} \equiv E_{\text{tot}} - E_{\text{SL}} = \sum_k^D \mathbf{d}^\dagger \mathbf{P}^{\text{null}} \mathbf{d} \quad (6.4)$$

where $\mathbf{P}^{\text{null}} = (\mathbf{I} - \mathbf{P}^{\text{GW}})$ is a projection operator orthogonal to \mathbf{P}^{GW} (\mathbf{I} is the identity operator). The null energy can be written as

$$E_{\text{null}} = \sum_k \sum_{\alpha, \beta} d_\alpha^\dagger \mathbf{P}_{\alpha\beta}^{\text{null}} d_\beta \quad (6.5)$$

which consists of cross-correlation terms ($\alpha \neq \beta$) and auto-correlation terms ($\alpha = \beta$). The auto-correlation part is the *incoherent energy*

$$I_{\text{null}} \equiv \sum_k \sum_\alpha \mathbf{P}_{\alpha\alpha}^{\text{null}} \|d_\alpha\|^2 \quad (6.6)$$

which dominates E_{null} for a non-astrophysical signal. Therefore $I_{\text{null}}/E_{\text{null}} \gg 1$ if a candidate is a GW and $I_{\text{null}}/E_{\text{null}} \simeq 1$ if it is a noise artifact. The coherent consistency cut applies a threshold on this ratio, determined by a tuning procedure, and candidates falling below the threshold are vetoed. Figure 31 shows the results of this step being applied to the on-source segment of a GRB analysis. The ratio

cut is applied in this case about a factor of two above the diagonal, where $I_{\text{null}} = E_{\text{null}}$.

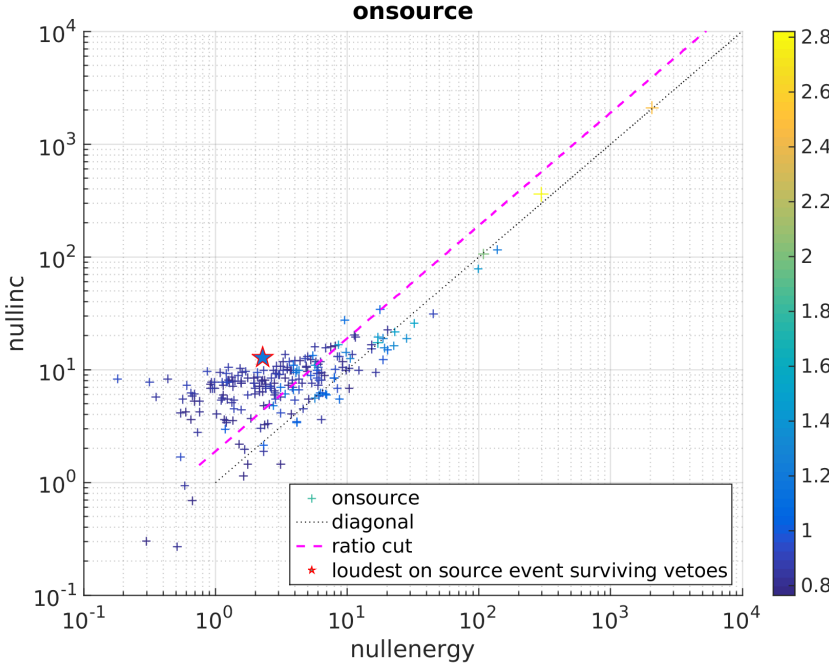


Figure 31. Coherent consistency cut performed by x-pipeline to veto noise triggers. The x - and y -axes represent E_{null} and I_{null} , respectively.

In the O3a search, the sensitivity to long-duration (≥ 10 s) GW signals was often limited by loud background noise transients. While the coherent consistency tests easily veto these glitches, many long-duration simulated signals would overlap such a glitch by chance. In these cases the simulated signal and glitch would be clustered together and subsequently vetoed together. To address this problem, an “autogating” procedure was implemented for O3b. For each detector, the total energy in the whitened data stream is computed over a 1 s window. If this total fluctuates by more than 50 standard deviations above the median value, then the data is zeroed out over the interval where the threshold is exceeded. A 1 s inverse Tukey window is applied at each end of the zeroed interval to transition smoothly

between the whitened and zeroed data. To minimize the possibility of a loud GW transient triggering a gate, the procedure cancels a gate if there is a simultaneous energy excursion above 10 standard deviations in any other detector. The threshold of 50 standard deviations is low enough to gate the most problematic loud glitches, while being high enough that the only GWs zeroed out by the gate would have been detectable by all-sky searches. Empirically we find that this procedure is effective at reducing the impact of loud glitches without affecting the sensitivity to low-amplitude GW signals.

6.2 O3b search for GWs associated with GRBs

Since O3 was split into two halves, O3a and O3b, the LIGO-Virgo GRB search was also split in two (Abbott et al., 2021b, 2022). The main differences in O3b where changes in the detector during the in-between commissioning phase resulted in improvements to the sensitivity of the LIGO detectors, and as mentioned above the autogating algorithm was introduced.

The full sample of GRBs occurring in O3b consists of seven short GRBs, 12 ambiguous GRBs, and 89 long GRBs. Of these, only two have known redshifts: GRB 191221B ($z = 1.148$) (Kuin & Swift/UVOT Team, 2019; Vielfaure et al., 2019) and GRB 200205B ($z = 1.465$) (Vielfaure & Stargate Collaboration, 2020). Since x-pipeline searches for coincident excess power, we perform the generic transient search for GRBs where at least two of the three LIGO-Virgo detectors were active. This leads to 86 GRBs to analyze and is also compatible with the network observing time of at least two detectors (85.3%).

Running x-pipeline produces a “closed-box” results page, which summarizes the results of the search on a “dummy” on-source window chosen from

among the off-source windows. This allows us to tune the parameters of the search, the injections, or the pre- and postprocessing to produce the most sensitive closed-box results before actually analyzing the on-source data (the “open-box” analysis). We first analyze each GRB *without* autogating, and rerun the closed-box analysis *with* autogating only if the initial closed box results suggest that autogating would improve the sensitivity of the search. The glitches targeted by autogating affect the ability of x-pipeline to detect long-duration signals, so we can determine if a closed-box analysis would perform better with autogating applied by looking for a clear plateau or dip in the detection efficiency curves of the long-duration ADI waveforms, accompanied by signs of high-energy triggers in diagnostic figures produced in the results page. If such a problem does exist, then the closed-box analysis is rerun with autogating, and the box with better efficiency curves (usually the autogated version) is opened. Otherwise, if autogating is not likely to affect the results, then we open the initial non-autogated box.

As an example of this procedure, we will consider the analysis of GRB191101A, an extreme case of noisy background data. This is a long GRB observed by Swift during which LHO, LLO, and Virgo were all active. Figure 32 shows the Gaussianity measures for the three detectors (LHO, LLO, and Virgo represented as H1, L1, and V1). The Gaussianity measures represent the ratios between the variance of the detector spectra to their means; high values correspond to high deviations from Gaussian behavior. The low-frequency excess is likely associated with scattered light noise, whereas the flat component is typical of the broadband glitches that autogating is designed to combat. The LHO and Virgo measures, meanwhile, lie within the normal levels of non-Gaussianity, shown by the black dashed lines at the bottom of the figure.

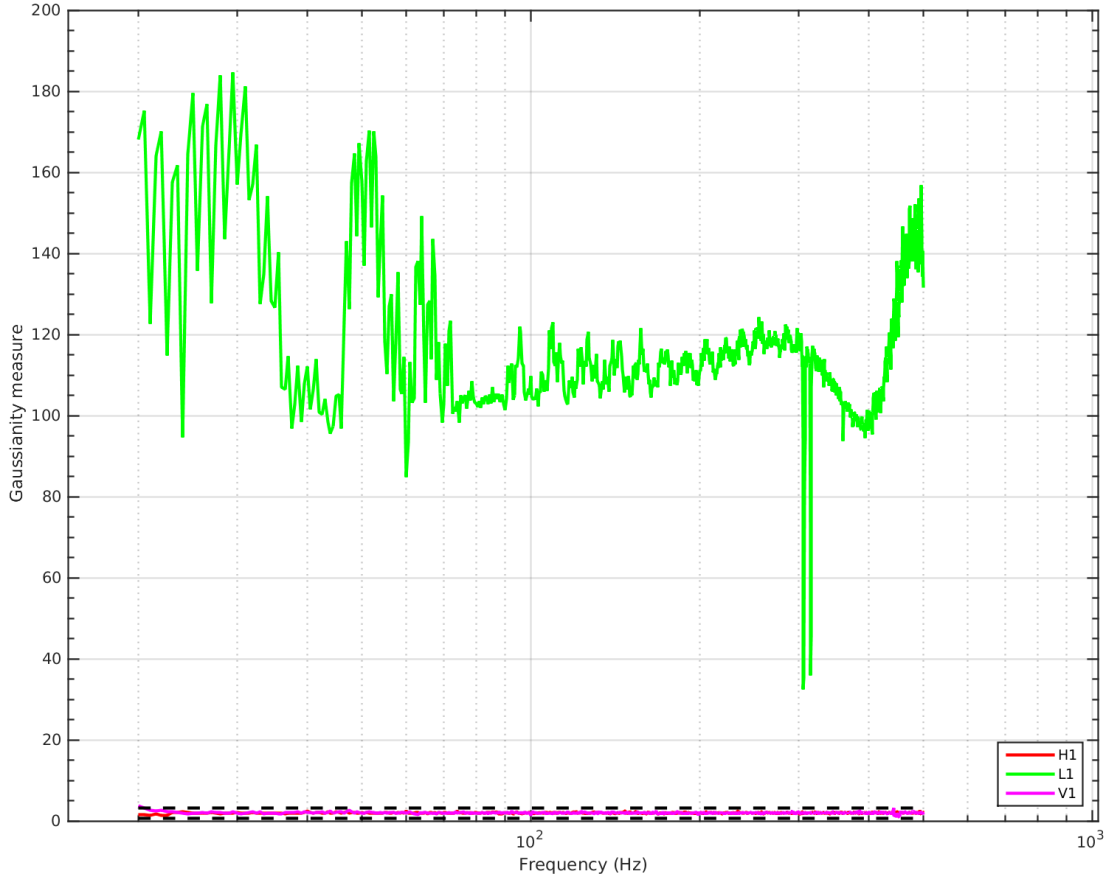


Figure 32. Gaussianity measures around the time of GRB191101A without autogating. The black horizontal dashed lines represent the expected levels of non-Gaussianity. LHO (H1) and Virgo (V1) are both within these bounds, while LLO (L1) far exceeds them.

Figure 33 shows the distribution of triggers in LLO and LHO after applying data quality vetoes but before applying coherent consistency vetoes. The most problematic glitches appear as triggers with energies in the tens of thousands. They make up a small minority of all the triggers, but their impact on the pipeline's ability to detect injected signals is tremendous.

Figure 34 shows a major dip in the detection efficiency for a long-duration injection, ADI-C, when autogating is not applied. The dip is entirely fixed with

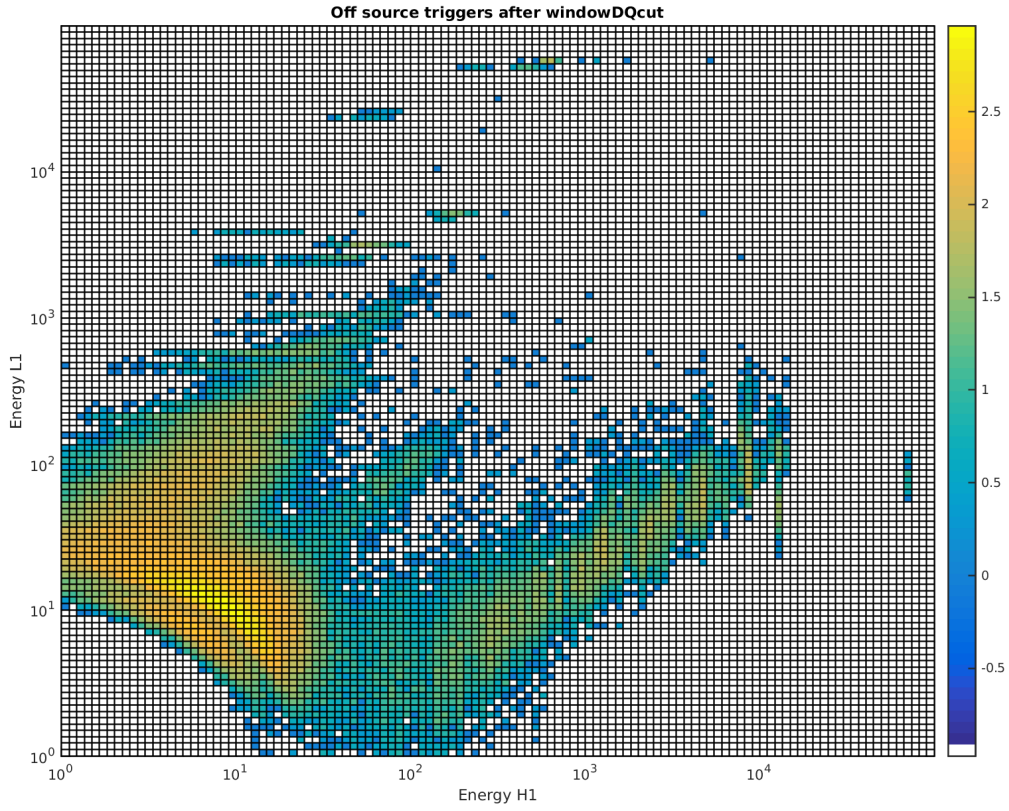


Figure 33. Distribution of off-source triggers in the LIGO detectors without autogating. The x- and y-axes are the signal energy in H1 and L1, respectively.

autogating active, leaving only a small, acceptable plateau in the efficiency curve around 95%.

Ultimately, autogating was performed on more than half of the 86 O3b GRB triggers analyzed by x-pipeline. This seems to suggest that it would be better to have autogating active by default, but it is not clear from an autogated closed box result page if it was needed in the first place. Therefore it is recommended that in future searches we continue to run x-pipeline without autogating first and only apply it when needed. Even though the negative trade-off of autogating (reducing detection efficiency for very high amplitude signals) is not too concerning, keeping the analysis as simple as possible may be a preferable route. Nevertheless, this will have to be weighed against the greater computing time spent for autogating reruns,

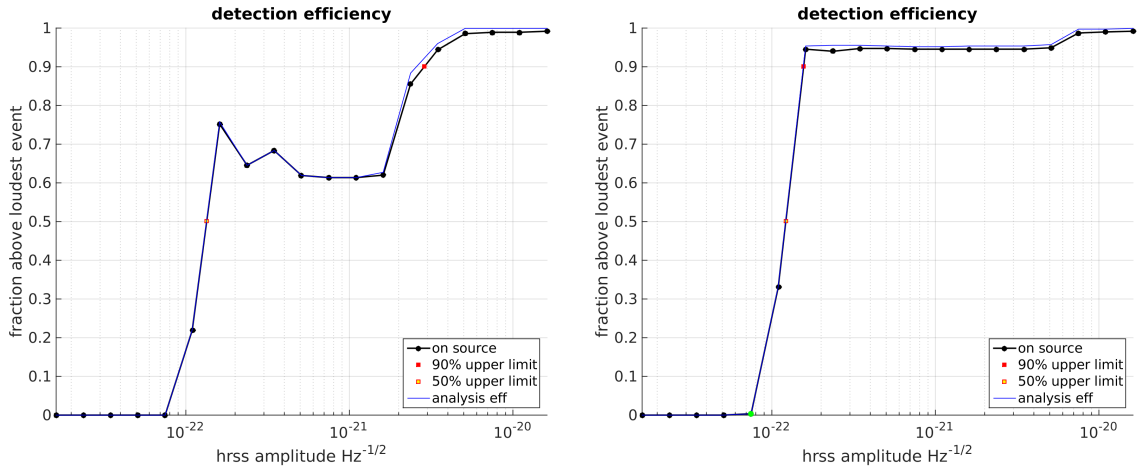


Figure 34. Detection efficiency of ADI-C injected waveforms without (left) and with (right) autogating.

since having to rerun most of the closed box analyses roughly doubles the amount of time before final results are produced.

6.2.1 Results of the O3b search

We rank each candidate by calculating a p-value, the probability of an event or a louder one in the on-source data, given the background distribution, under the null hypothesis. The p-value is calculated by counting the fraction of background trials that contain an event with a greater signal-to-noise ratio than that of the loudest on-source event. Figure 35 shows the distribution of p-values for the 86 GRBs analyzed by x-pipeline. In this plot, a significant event would appear at a much lower p-value in the lower left corner of the plots, and be outside (to the left) of the 90% confidence region. The plot shows that the p-value distribution is consistent with the background. The lowest reported p-value found during O3b for the generic transient search was 7.95×10^{-3} (GRB 200224B). Although this p-value is very small, it is not unexpected given the high number of GRBs analyzed.

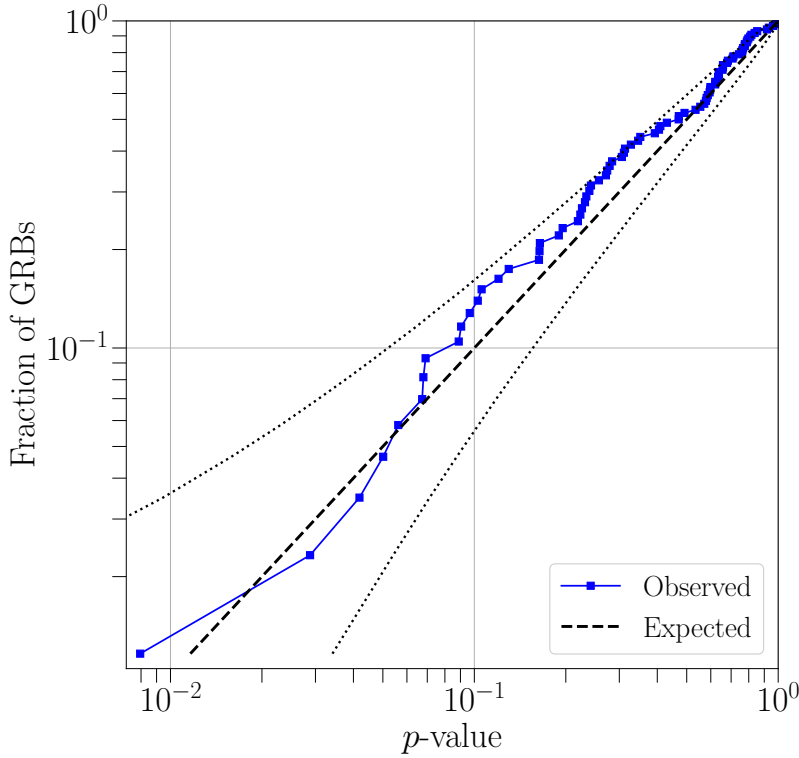


Figure 35. Cumulative distribution of p-values for the loudest on-source events of the O3b X-pipeline analyses. The dashed line indicates an expected uniform distribution of p-values under a no-signal hypothesis, with the corresponding 90% band as the dotted lines.

Given that no loud GW signals are observed coincident with any of the GRBs in this search, we perform a weighted binomial test to determine the probability of observing our set of p-values assuming a uniform background distribution (Abadie et al., 2012; B. Abbott et al., 2008). A small probability would suggest that there may be a population of subthreshold GW signals that our search did not identify. This type of weighted binomial test uses the lowest re-weighted p-values from the searches. For the generic transient search, the test gives a probability of 0.76. The same test carried out in O3a returned a probability of 0.30 (Abbott et al., 2021b). In O2 (removing GW170817/GRB 170817A) and O1 the probabilities were 0.75 and 0.75, respectively (Abbott et al., 2017; B. P. Abbott

et al., 2019). As in these previous analyses, the probabilities obtained in O3b suggest that no weak GW sources can be attributed to the population of GRBs.

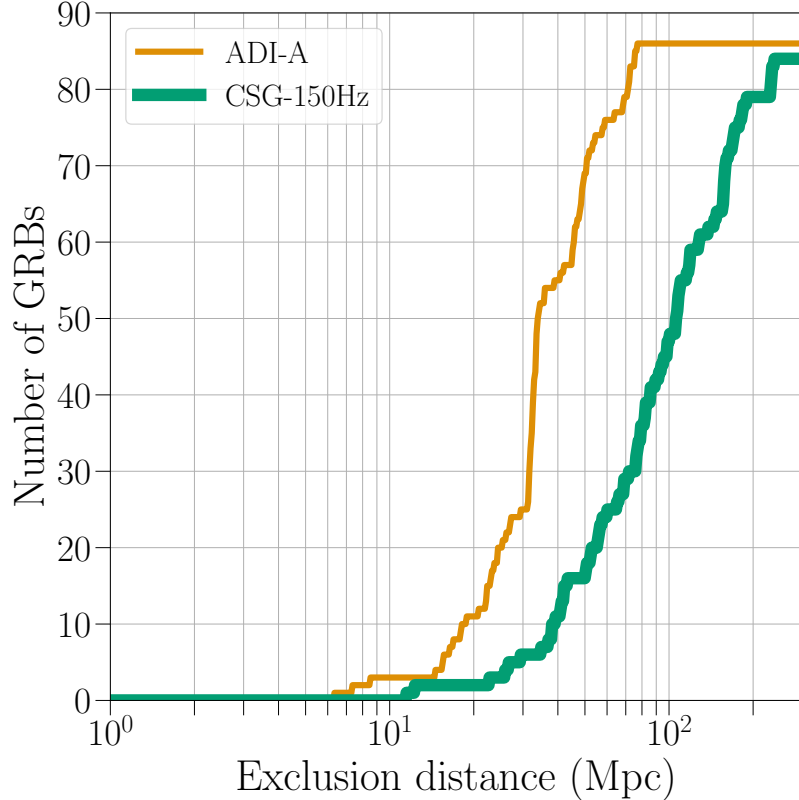


Figure 36. Cumulative distributions of O3b exclusion distances for 150-Hz sine-Gaussian and ADI-A waveforms.

We derive a 90% confidence level lower limit on the distance for each of the 86 GRBs analyzed with the generic transient search, based on the different emission models. Figure 36 shows the distribution of D_{90} values for the ADI-A model and for a CSG with central frequency of 150 Hz. The limits reported depend on the sensitivity of the instruments in the network, which change with time and sky localization of the GRB events. We marginalize these limits over errors introduced by detector calibration. Table 5 reports the median D_{90} , for the set of GRBs for the different signals. The limits vary by nearly an order of magnitude due to the

variety of signals used in our analysis. On average, the median values for the O3b generic transient search are about 50% greater than those reported in O3a (Abbott et al., 2021b).

Table 5. Median 90% exclusion distances (D_{90}) for the generic transient search during O3b.

	CSG 70 Hz	CSG 100 Hz	CSG 150 Hz	CSG 300 Hz
D_{90} [Mpc]	166	126	92	42
	ADI-A	ADI-B	ADI-C	ADI-D
D_{90} [Mpc]	34	140	54	22
	ADI-E			
D_{90} [Mpc]			52	

6.2.2 Noise effects in the generic transient search

Comparing the exclusion distances of the O3a and O3b search sheds some light on the impact of detector and search pipeline improvements on the sensitivity of the x-pipeline analysis. Table 6 presents the improvement in the median D_{90} for each waveform model as a fraction of the O3a value. The exclusion distances for the shorter-duration CSG waveforms, which are not expected to be affected by autogating, increased by about 30% on average.

Table 6. Relative increase in median D_{90} for each x-pipeline simulated waveform.

	CSG 70 Hz	CSG 100 Hz	CSG 150 Hz	CSG 300 Hz
$\Delta D_{90}/D_{90,\text{O3a}}$	0.12	0.19	0.25	0.49
	ADI-A	ADI-B	ADI-C	ADI-D
$\Delta D_{90}/D_{90,\text{O3a}}$	0.43	0.14	0.85	0.92
	ADI-E			
$\Delta D_{90}/D_{90,\text{O3a}}$			0.55	

Given the large number of GRBs analyzed, it would be unlikely for the difference to be explained by chance improvement in antenna response (i.e. due to more GRBs lining up with the sky region where the GW detector network is most sensitive). X-pipeline reports the antenna response of the GW detectors for each GRB analyzed. These can be summed up over the active detectors for each GRB and averaged over the full GRB sample. The result is a 9.2% improvement in antenna response, which is not negligible but can only account for a small portion of the differences in exclusion distances.

For the longest duration ADI-C, ADI-D, and ADI-E waveforms, we see the greatest improvements, over 50% higher than in O3a (Figure 37, top). For short-duration waveforms, the highest-frequency 300-Hz sine-Gaussian injections show the greatest change (Figure 37, bottom). These are all well above the change expected from a chance difference in antenna response.

Considering that longer-duration waveforms see greater improvement, the most obvious likely contributor is the implementation of autogating. However, autogating cannot account for the changes in the D_{90} of short-duration models. These can only be explained by better GW detector sensitivity and/or reduced rates of short-duration glitches that overlap the injected signal. Such glitches cause the entire injection to be vetoed, so it is not recovered by the search pipeline. In particular, glitches caused by low-frequency scattering noise (discussed in Section 5.2) can pepper a stretch of time with short-duration glitches, overlapping injections made at multiple points. A method for reducing the occurrence of these glitches, reaction chain (RC) tracking, was implemented at LIGO Hanford (LHO) on Jan 7, 2020 at LIGO Livingston (LLO) and Jan 15, 2020 (Soni et al., 2020).

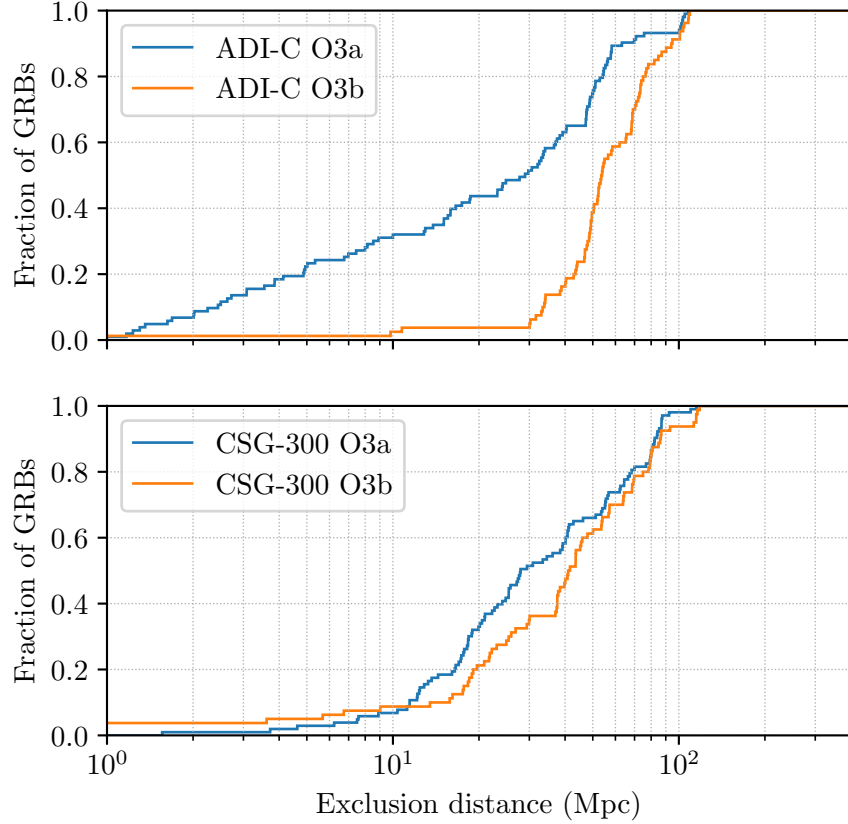


Figure 37. Cumulative distributions of O3a and O3b exclusion distances for the ADI-C (top) and 300-Hz sine-Gaussian (bottom) waveforms. These show the greatest improvement between O3a and O3b among their respective waveform sets.

Figure 38 gives evidence for the effect of glitch mitigation on x-pipeline sensitivity. Although there is clearly a bias towards higher antenna responses after RC tracking, they do not entirely account for the huge substantial increase in exclusion distances.

In summary, noise mitigation is a crucial part of improving the sensitivity of the generic transient search. As discussed above, there may plenty that can be inferred even in the absence of detections. Better detector sensitivities in O4,

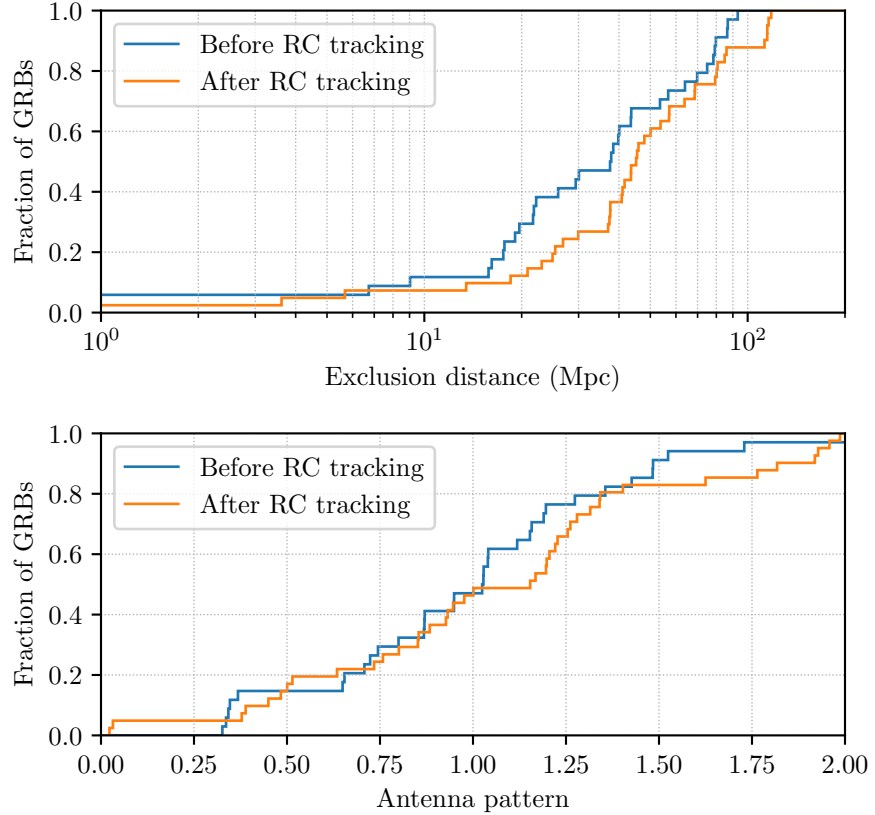


Figure 38. Cumulative distributions of CSG-300 Hz exclusion distances (top) and the detector network antenna factors (bottom) for GRBs before and after the implementation of RC tracking.

along with the development of new glitch subtraction methods, could allow more confident exclusion of GW emission models, or some regions of their parameter space, associated with GRBs.

6.2.3 Model exclusion

Although x-pipeline is an entirely unmodeled GW search pipeline, given the substantial improvement in the exclusion distances in O3b, we may be

approaching the point at which extreme GW emission models associated with long GRBs can be excluded using our null results and the sensitivity estimates for injected waveforms. Using detection efficiency curves of both the O3a and O3b searches, we can compute for each model an exclusion confidence using the method described in Kalmus, Zanolin, and Klimenko (2013) for supernova searches (Abbott et al., 2019). The model exclusion probability given N targeted GRBs is

$$P_{\text{excl}} = 1 - \prod_{i=1}^N [1 - \varepsilon_i(d_i)] \quad (6.7)$$

where $\varepsilon_i(d_i)$ is the detection efficiency at the source distance of d_i . Of the 86 GRBs analyzed in the O3b search by x-pipeline, only one, GRB 191221B has a redshift measurement (GRB 200205B did not occur at a time when at least two detectors were active and was therefore not included). For the remaining GRBs, we have no distance measurement, but instead we can sample d_i from the historical distribution of redshifts measured by Swift BAT since 2005.

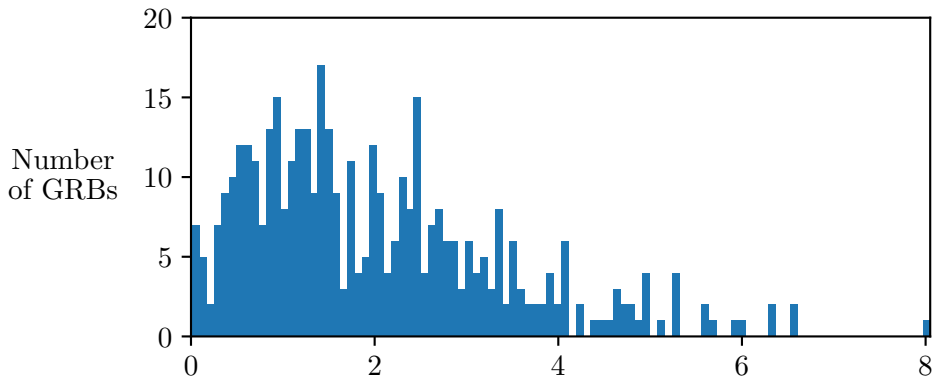


Figure 39. Histogram of redshift measurements for GRBs detected by Swift BAT.

The Swift GRB archive has redshift measurements for 411 triggers (*Swift GRB Archive*, 2022). Figure 39 shows the distribution of those measurements, from which we sample distances for the 86 GRBs analyzed, using inverse transform

sampling, and compute exclusion probability for each model. This is repeated 1,000 times and P_{excl} is averaged for each model across all trials.

Table 7. Exclusion confidence for each injected waveform model.

	CSG 70 Hz	CSG 100 Hz	CSG 150 Hz	CSG 300 Hz
P_{excl}	0.74	0.63	0.44	0.12
	ADI-A	ADI-B	ADI-C	ADI-D
P_{excl}	0.04	0.61	0.15	0.00
	ADI-E			
P_{excl}				0.18

The averages are presented in Table 7. The model with the highest exclusion probability is the 70-Hz sine-Gaussian model. Assuming that the Swift redshift distribution is representative of the GRBs analyzed by x-pipeline, it is more likely than not that we can rule out the very optimistic energies simulated by the low-frequency 70-Hz and 100-Hz sine-Gaussian injections ($E_{\text{GW}} = 10^{-2} M_{\odot} c^2$) based on the lack of GW-GRB joint detections at O3 sensitivity.

If the sensitivity of the LIGO detectors continues to improve in O4, we may well be able to begin ruling out the most extreme emission models. The exclusion probability for the ADI-B model is 0.61, making it the only unfavorable ADI model so far. This accretion disk instability model is simulated for a central BH mass of $M = 10 M_{\odot}$, a dimensionless spin parameter of $\chi = 0.95$, and a very large clump mass of $\epsilon = 0.2$ times that the central BH. It is the most extreme of the ADI models, and it would not be surprising to see it being ruled out in future searches.

More to be added to this section. Some work is still ongoing.

CHAPTER VII

CONCLUSION

Noise plays a profound role in the field of gravitational wave astronomy. Understanding how the many sources of noise affect the sensitivity and data quality of the LIGO detectors is crucial to improving our ability to detect astrophysical signals. Even in the absence of detections, having better sensitivity allows us to make stronger constraints on models of GW emission.

In this dissertation I have summarized my contributions to the characterization various vibrational and magnetic noise sources. I have presented methods for measuring coupling functions, and produced noise budgets representing their effects on both of the LIGO detectors. The vibrational noise budgets have shown that scattering noise is a dominant issue in the detection band of both interferometers, influencing future plans for mitigating stray light beams in O4 and beyond. Through the magnetic noise budgets we have seen that coupling in the detection band can arise and shift in frequency and amplitude due to changes in hardware around the detectors. Our newly implemented software and hardware infrastructure for making routine magnetic field injections will allow careful monitoring of these changes. At low frequencies, the magnetic noise budgets also suggest that coupling via permanent magnets may become an issue once more in the future, as LIGO comes closer to design sensitivity.

These coupling functions measured for individual sensors have also been essential in developing an automated event validation system for GW candidates. Excess noise estimates computed from coupling functions have allowed us to quantitatively confirm that environmental signals did not account for any of the GW detections made by the LIGO collaboration in the third observing run. The

pipeline for O4 has been expanded to incorporate time-frequency information of a GW event and the local background noise of the environmental sensors to produce p-values representing the statistical significance of noise transients overlapping the event. As the rate of detections continues to increase in the coming years, innovations like these will only become more important, especially if we detect phenomena that have yet to be observed by GW detectors, such as core-collapse supernovae.

The search for GWs associated with GRBs during O3 yielded no new joint detections. However, we set new upper limit exclusion distances on both short and long duration GW emission models. The x-pipeline analysis in O3b was able to exclude the existence of GW emissions up to 140 Mpc for the most extreme accretion disk instability waveform (ADI-B), and up to 166 Mpc for the lowest-frequency sine-Gaussian waveform. These upper limits are far better than the ones set in the O3a search. We showed that the improvements were attributable to both software-based noise subtraction, as well as reductions in transient scattered light noise.

Although much can still be done to develop better astrophysical search pipelines, this dissertation has shown that achieving the scientific goals of the LIGO collaboration requires dedicated studies of noise sources and their impacts on GW searches. The methods for characterizing environmental noise and validating GW events are relevant to any ground-based interferometer. LIGO has already been joined by collaborators at Virgo in Italy and KAGRA in Japan, who have incorporated some of our methods in developing their own noise monitoring systems. LIGO India, although still in its planning phase will hopefully find this work helpful as well. Looking forward, the planned next-generation detector Cosmic

Explorer will push the frontier of GW astronomy even further and likewise require a new generation of noise characterization methods.

APPENDIX A

PEMCOUPLING EXAMPLES

This appendix presents examples of files produced by the `pemcoupling` package to give readers some guidance on interpreting the outputs. Each injection is given its own directory in which results are saved and an HTML page is created with a table of links to the output files, sorted by channel name (Figure A.1).

There are two types of figures produced by `pemcoupling` at the single-injection, single-sensor level: a coupling function plot and an estimated ambient plot. Coupling function plots are produced in the physical, calibrated, sensor units (Figure A.2), as well as in raw counts (Figure A.3). In the former case the units will look like [m/T] for magnetometers, while in the latter the units are [m/counts], regardless of sensor type. Estimated ambients are always shown in calibrated units (Figure A.4). Each plot is annotated with information about the injection and analysis. From left to right, top to bottom:

- Name of the injection, as specified by the user.
- Timestamp of when the analysis was run.
- Number of Number of measurements and upper limits computed.
- UTC and GPS start time of the injection data.
- Number of FFT averages and frequency bin width.
- UTC and GPS start time of the background data.

Table A.1 summarizes the contents of the output ASCII data output file. The data will be preceded by a commented line (starting with a # character)

PEMCoupling results (CSAcoustic_FarOutputOptics_30to100Hz)

[Configuration file](#)

Coupling function results

Key:

Green = success

Yellow = no calibration data given

Orange = no coupling factors found

Red = could not fetch channel, or channel was rejected due to saturation

Channel	Data	Coupling function plots	Amplitude spectra and estimated ambient plots	Notes
L1:PEM-CS_ACC_BEAMTUBE_MCTUBE_Y	ASCII data	coupling function (calibrated) coupling function (uncalibrated)	spectra and estimated ambient	
L1:PEM-CS_ACC_BEAMTUBE_SRTUBE_X	ASCII data	coupling function (calibrated) coupling function (uncalibrated)	spectra and estimated ambient	
L1:PEM-CS_ACC_BEAMTUBE_XMAN_Y	ASCII data	coupling function (calibrated) coupling function (uncalibrated)	spectra and estimated ambient	
L1:PEM-CS_ACC_BEAMTUBE_YMAN_X	ASCII data	coupling function (calibrated) coupling function (uncalibrated)	spectra and estimated ambient	
L1:PEM-CS_ACC_BSC1_ITMY_X	ASCII data	coupling function (calibrated) coupling function (uncalibrated)	spectra and estimated ambient	
L1:PEM-CS_ACC_BSC1_ITMY_Y	ASCII data	coupling function (calibrated) coupling function (uncalibrated)	spectra and estimated ambient	
L1:PEM-CS_ACC_BSC2_BS_Y	ASCII data	coupling function (calibrated) coupling function (uncalibrated)	spectra and estimated ambient	

Figure A.1. HTML page for a single-injection coupling function run.

denoting the comb fundamental frequency if the injection was a comb injection,

e.g. `#combfreq: 7.10.`

Composite coupling function output files are saved to another directory, by default named `CompositeCouplingFunctions`. These figures follow the same organization: a physical coupling function (with colors representing different injections, Figure A.5), a raw coupling function (Figure A.6), and an estimated ambient. (Figure A.7). The raw-counts composite coupling function does not distinguish injections as it is only used to make noise projections, such as by `pemcheck`, as opposed to identify noise sources.

Last is an example of a site-wide estimated ambient (Figure A.8) plot.

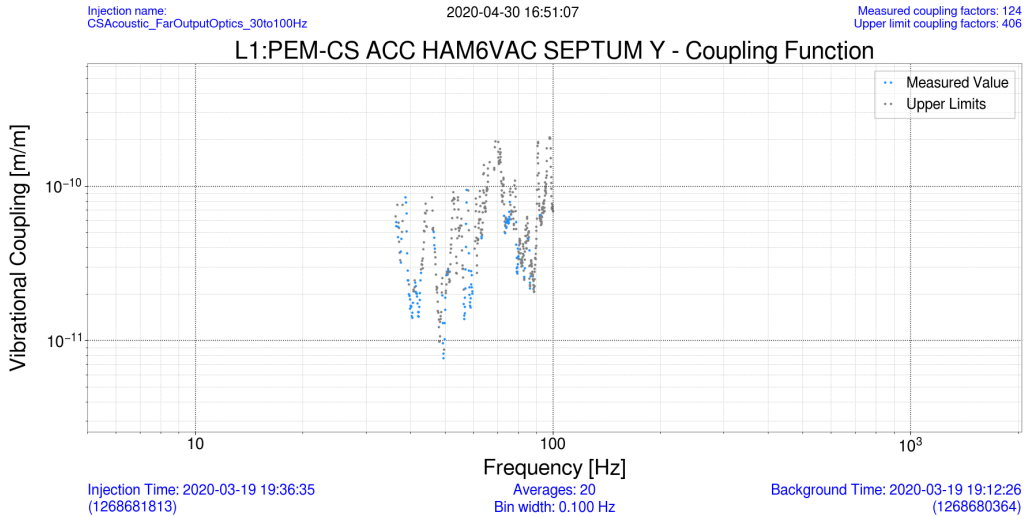


Figure A.2. Coupling function in physical units for the Y-axis HAM 5/6 septum accelerometer from a broadband acoustic injection.

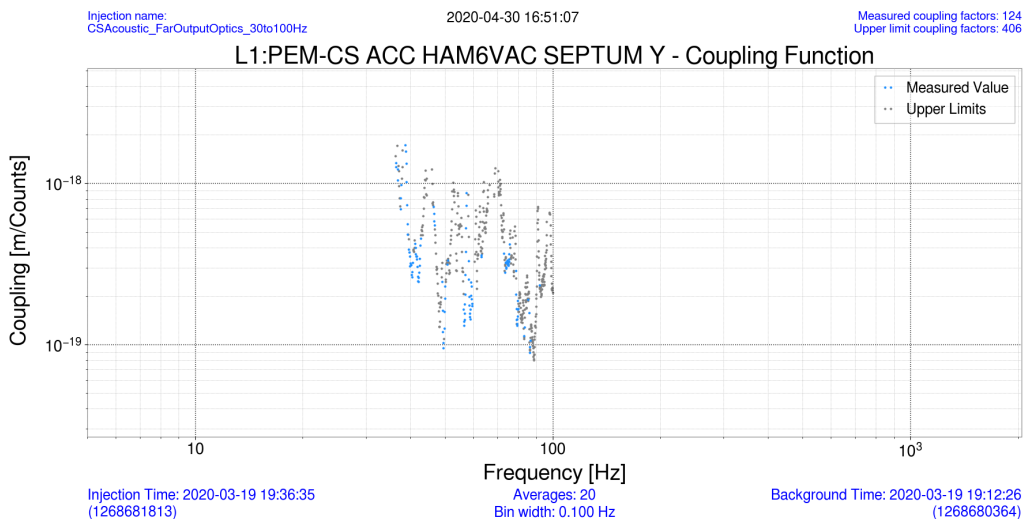


Figure A.3. Coupling function in ADC counts for the Y-axis HAM 5/6 septum accelerometer from a broadband acoustic injection.

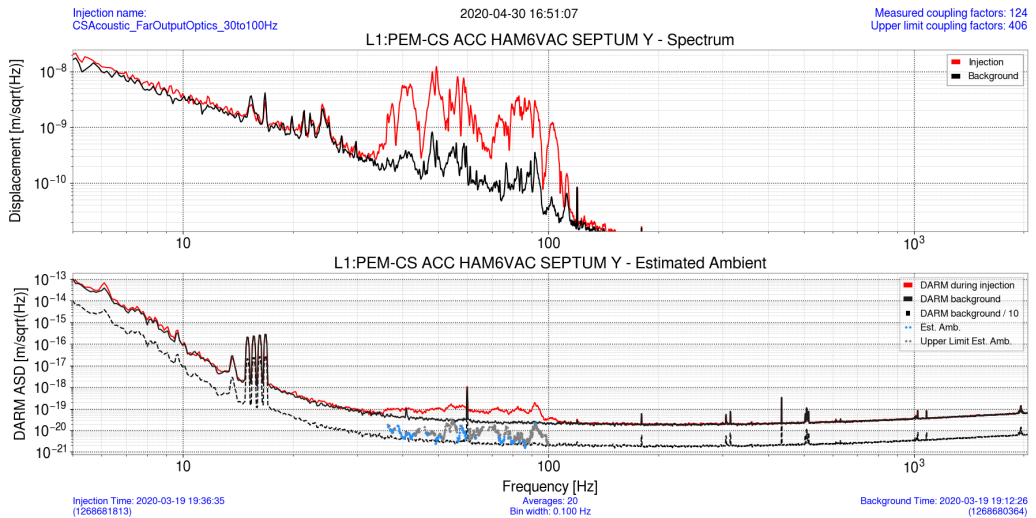


Figure A.4. Estimated ambient for the Y-axis HAM 5/6 septum accelerometer from a broadband acoustic injection.

column	description
frequency	bin center frequency [Hz]
factor	coupling factor in [m/calibrated sensor unit]
factor_counts	coupling factor in [m/ADC count]
flag	“Measured”, “Upper Limit”, “Thresholds not met”, or “No data”
sensINJ	sensor amplitude at injection time [calibrated sensor unit/ $\text{Hz}^{1/2}$]
sensBG	sensor amplitude at background time [calibrated sensor unit/ $\text{Hz}^{1/2}$]
darmINJ	GW channel amplitude at injection time [$\text{m}/\text{Hz}^{1/2}$]
darmBG	GW channel amplitude at background time [$\text{m}/\text{Hz}^{1/2}$]

Table A.1. Column descriptions for the single-injection coupling function output of the pemcoupling package.

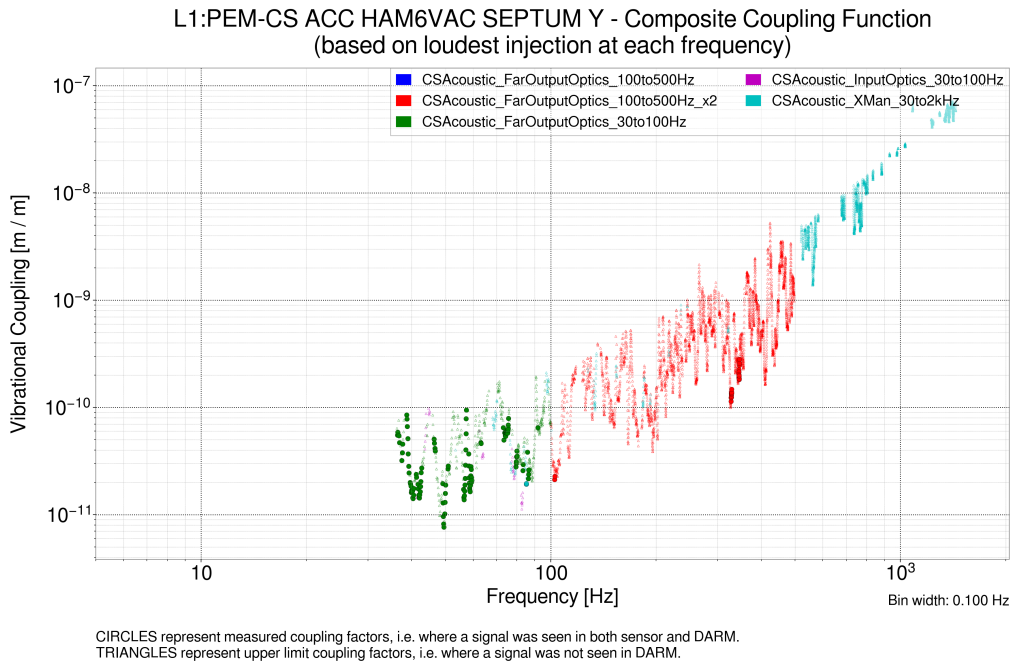


Figure A.5. Composite coupling function in physical units for the Y-axis HAM 5/6 septum accelerometer.

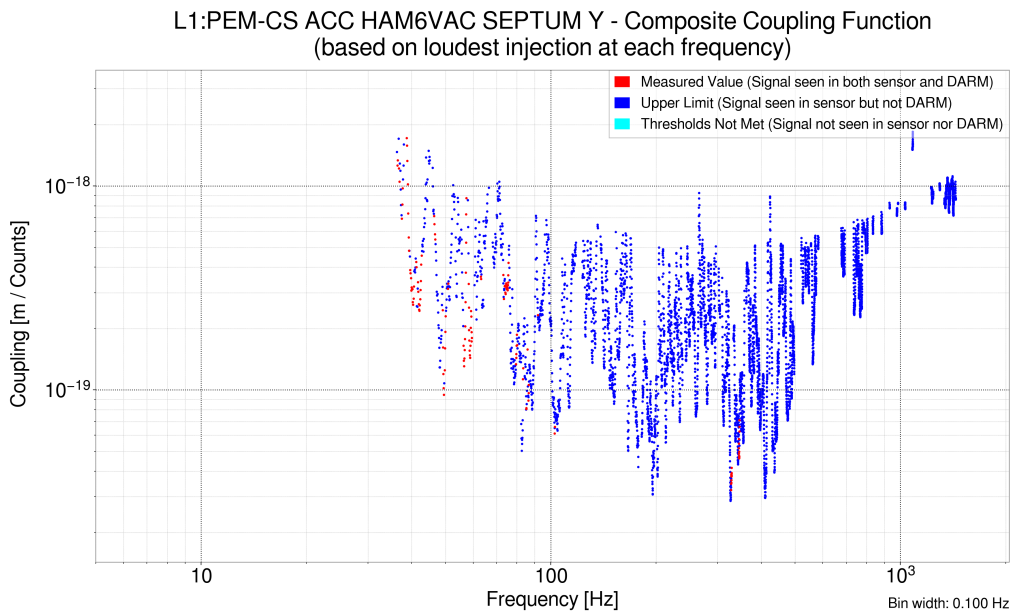


Figure A.6. Composite coupling function in physical units for the Y-axis HAM 5/6 septum accelerometer.

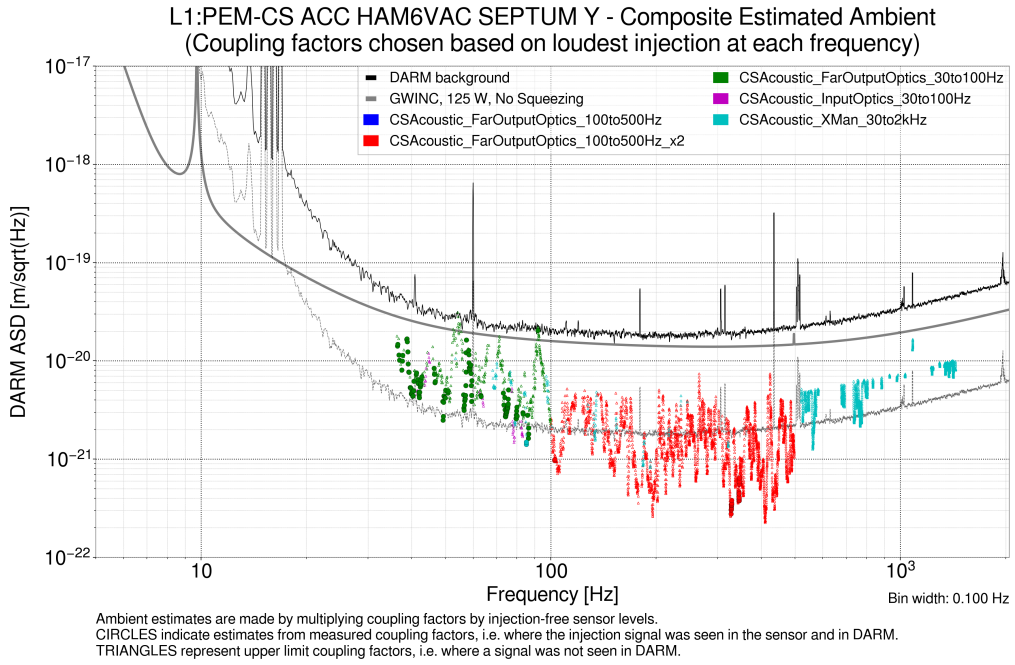


Figure A.7. Estimated ambient for the Y-axis HAM 5/6 septum accelerometer.

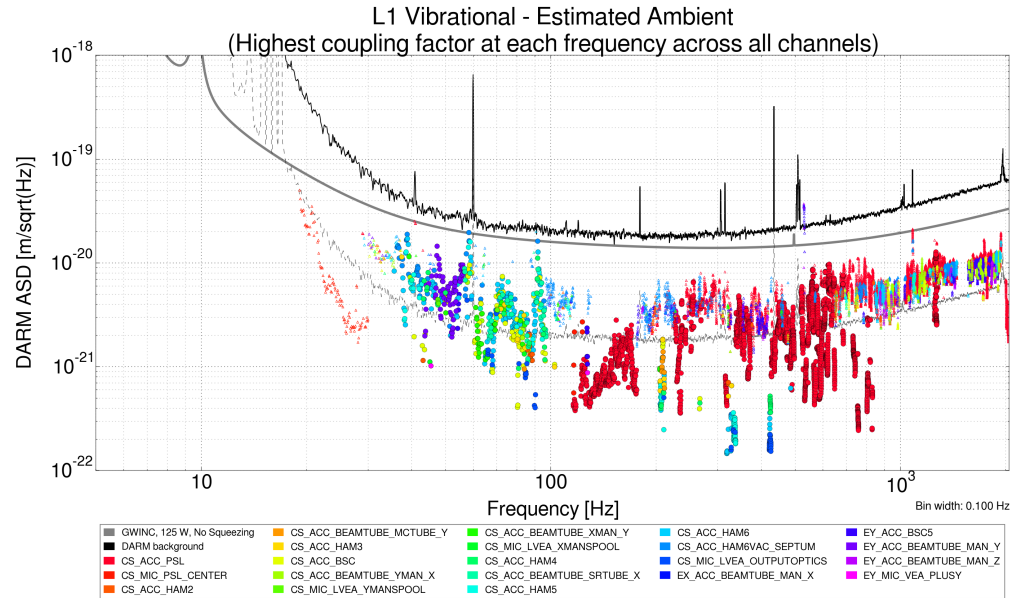


Figure A.8. Site-wide estimated ambient for all vibrational sensors at LLO.

APPENDIX B

PEMCHECK EXAMPLES

This appendix presents screenshots of pemcheck output pages tested on GW events and environmental noise transients. The report page is sorted by likelihood of excess noise in the strain channel, and the top channel is shown alongside a constant-Q transform of the stain channel. Input parameters, chosen based on properties of the GW candidate, are shown, as well as the time and frequency of the peak-probability pixel.

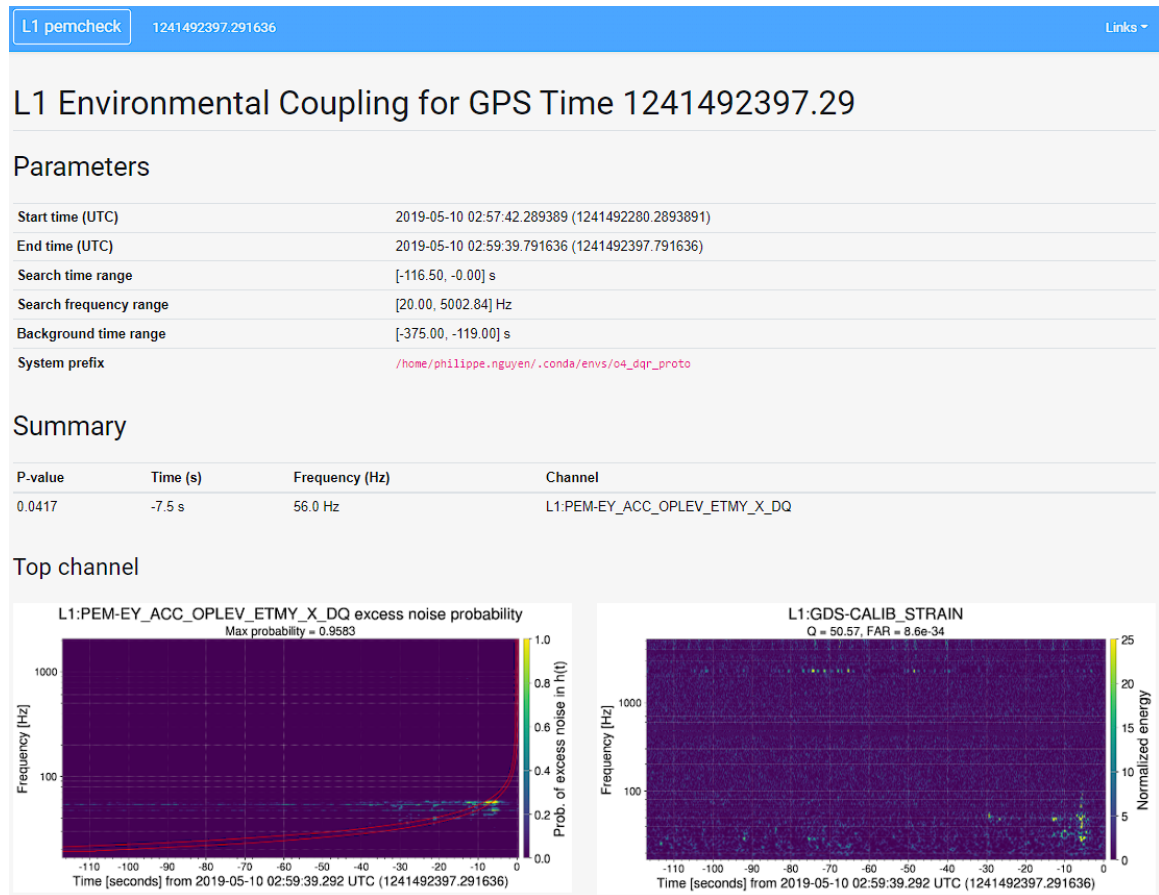


Figure B.1. Example for a long duration CBC merger candidate S190510g, overlapping with excess noise that is almost certainly associated with vibrational noise at ETMY.

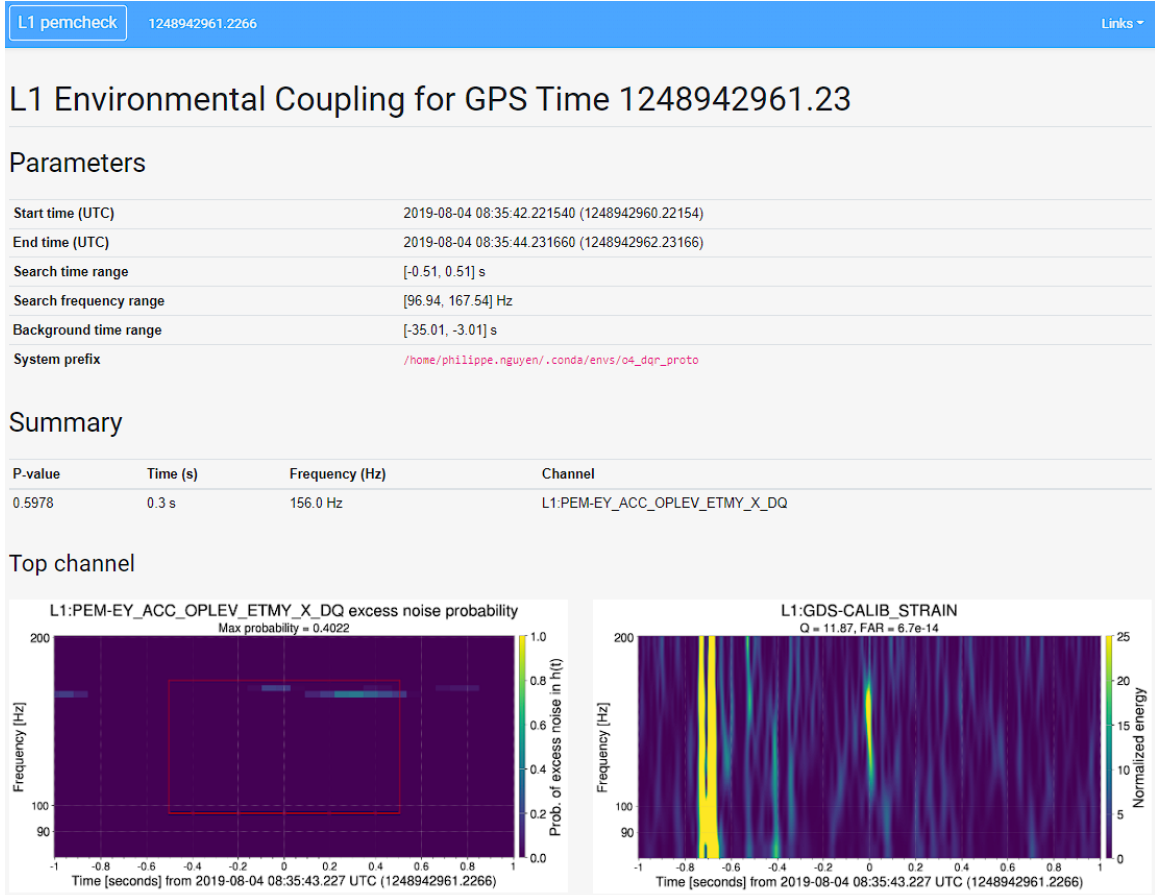


Figure B.2. Example for a burst candidate S190804qr reported by cWB, showing that a loud noise observed near ETMY could contribute to the GW event candidate signal but not with a high probability.

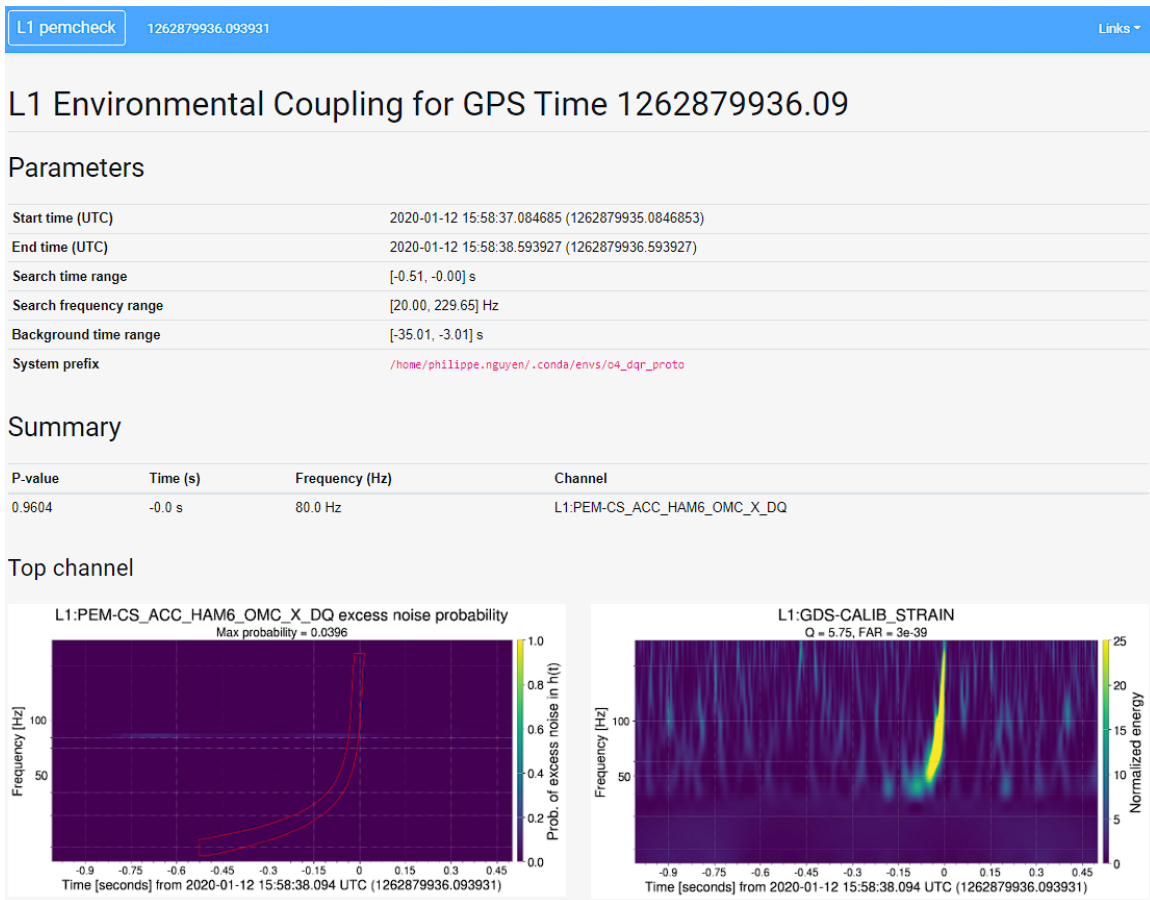


Figure B.3. Example of a typical short-duration CBC merger candidate S200112r, with no excess noise expected to appear in the GW channel.

REFERENCES CITED

- Aasi, J., et al. (2015, March). Advanced LIGO. *Class. Quantum Grav.*, *32*(7), 074001.
- Abadie, J., et al. (2011, Feb). Search for gravitational waves associated with the august 2006 timing glitch of the vela pulsar. *Phys. Rev. D*, *83*, 042001. Retrieved from <https://link.aps.org/doi/10.1103/PhysRevD.83.042001> doi: 10.1103/PhysRevD.83.042001
- Abadie, J., et al. (2012, November). Search for Gravitational Waves Associated with Gamma-Ray Bursts during LIGO Science Run 6 and Virgo Science Runs 2 and 3. *ApJ*, *760*(1), 12. doi: 10.1088/0004-637X/760/1/12
- Abbott, B., et al. (2008, Mar). Search for gravitational waves associated with 39 gamma-ray bursts using data from the second, third, and fourth ligo runs. *Phys. Rev. D*, *77*, 062004. Retrieved from <https://link.aps.org/doi/10.1103/PhysRevD.77.062004> doi: 10.1103/PhysRevD.77.062004
- Abbott, B. P., Abbott, R., Abbott, T. D., Acernese, F., Ackley, K., Adams, C., ... et al. (2017, Oct). Gravitational waves and gamma-rays from a binary neutron star merger: Gw170817 and grb 170817a. *ApJ*, *848*(2), L13. Retrieved from <http://dx.doi.org/10.3847/2041-8213/aa920c> doi: 10.3847/2041-8213/aa920c
- Abbott, B. P., et al. (2016a, Jun). Characterization of transient noise in Advanced LIGO relevant to gravitational wave signal GW150914. *Class. Quantum Grav.*, *33*(13), 134001.
- Abbott, B. P., et al. (2016b, Feb). Observation of gravitational waves from a binary black hole merger. *Phys. Rev. Lett.*, *116*, 061102.
- Abbott, B. P., et al. (2017, November). A gravitational-wave standard siren measurement of the Hubble constant. *Nature*, *551*(7678), 85-88. doi: 10.1038/nature24471
- Abbott, B. P., et al. (2017a, Oct). GW170817: Observation of gravitational waves from a binary neutron star inspiral. *Phys. Rev. Lett.*, *119*, 161101.
- Abbott, B. P., et al. (2017b, oct). Multi-messenger observations of a binary neutron star merger. *The Astrophysical Journal*, *848*(2), L12. Retrieved from <https://doi.org/10.3847/2041-8213/aa91c9> doi: 10.3847/2041-8213/aa91c9

- Abbott, B. P., et al. (2017, June). Search for Gravitational Waves Associated with Gamma-Ray Bursts during the First Advanced LIGO Observing Run and Implications for the Origin of GRB 150906B. *ApJ*, *841*(2), 89. doi: 10.3847/1538-4357/aa6c47
- Abbott, B. P., et al. (2019, July). All-sky search for short gravitational-wave bursts in the second Advanced LIGO and Advanced Virgo run. *Phys. Rev. D*, *100*(2), 024017. doi: 10.1103/PhysRevD.100.024017
- Abbott, B. P., et al. (2019, Sep). GWTC-1: A gravitational-wave transient catalog of compact binary mergers observed by LIGO and Virgo during the first and second observing runs. *Phys. Rev. X*, *9*, 031040. Retrieved from <https://link.aps.org/doi/10.1103/PhysRevX.9.031040> doi: 10.1103/PhysRevX.9.031040
- Abbott, B. P., et al. (2019, November). Search for Gravitational-wave Signals Associated with Gamma-Ray Bursts during the Second Observing Run of Advanced LIGO and Advanced Virgo. *ApJ*, *886*(1), 75. doi: 10.3847/1538-4357/ab4b48
- Abbott, B. P., et al. (2020a, March). GW190425: Observation of a Compact Binary Coalescence with Total Mass $\sim 3.4 M_{\odot}$. *ApJ*, *892*(1), L3. doi: 10.3847/2041-8213/ab75f5
- Abbott, B. P., et al. (2020b, September). Prospects for observing and localizing gravitational-wave transients with Advanced LIGO, Advanced Virgo and KAGRA. *Living Reviews in Relativity*, *23*(1), 3. doi: 10.1007/s41114-020-00026-9
- Abbott, R., et al. (2020, September). GW190521: A Binary Black Hole Merger with a Total Mass of $150 M_{\odot}$. *Phys. Rev. Lett.*, *125*(10), 101102. doi: 10.1103/PhysRevLett.125.101102
- Abbott, R., et al. (2021a, Jun). Constraints on cosmic strings using data from the third advanced ligo–virgo observing run. *Phys. Rev. Lett.*, *126*, 241102. Retrieved from <https://link.aps.org/doi/10.1103/PhysRevLett.126.241102> doi: 10.1103/PhysRevLett.126.241102
- Abbott, R., et al. (2021b, Jun). Gwtc-2: Compact binary coalescences observed by ligo and virgo during the first half of the third observing run. *Phys. Rev. X*, *11*, 021053. Retrieved from <https://link.aps.org/doi/10.1103/PhysRevX.11.021053> doi: 10.1103/PhysRevX.11.021053

- Abbott, R., et al. (2021c). GWTC-3: Compact binary coalescences observed by LIGO and Virgo during the second part of the third observing run.
- Abbott, R., et al. (2021a, July). Observation of Gravitational Waves from Two Neutron Star-Black Hole Coalescences. *ApJ*, *915*(1), L5. doi: 10.3847/2041-8213/ac082e
- Abbott, R., et al. (2021b, July). Search for Gravitational Waves Associated with Gamma-Ray Bursts Detected by Fermi and Swift during the LIGO-Virgo Run O3a. *ApJ*, *915*(2), 86. doi: 10.3847/1538-4357/abee15
- Abbott, R., et al. (2022, jan). Search for continuous gravitational waves from 20 accreting millisecond x-ray pulsars in o3 LIGO data. *Physical Review D*, *105*(2). Retrieved from <https://doi.org/10.1103%2Fphysrevd.105.022002> doi: 10.1103/physrevd.105.022002
- Abbott, R., et al. (2022, April). Search for Gravitational Waves Associated with Gamma-Ray Bursts Detected by Fermi and Swift during the LIGO-Virgo Run O3b. *ApJ*, *928*(2), 186. doi: 10.3847/1538-4357/ac532b
- Abbott, R., et al. (2022). Search for intermediate-mass black hole binaries in the third observing run of Advanced LIGO and Advanced Virgo. *Astron. Astrophys.*, *659*, A84. doi: 10.1051/0004-6361/202141452
- Acernese, F., et al. (2022, February). Calibration of advanced Virgo and reconstruction of the detector strain h(t) during the observing run O3. *Classical and Quantum Gravity*, *39*(4), 045006. doi: 10.1088/1361-6382/ac3c8e
- Adams, S. M., Kochanek, C. S., Beacom, J. F., Vagins, M. R., & Stanek, K. Z. (2013, December). Observing the Next Galactic Supernova. *ApJ*, *778*(2), 164. doi: 10.1088/0004-637X/778/2/164
- Alekseev, E. N., Alekseeva, L. N., Krivosheina, I. V., & Volchenko, V. I. (1988). Detection of the Neutrino Signal From SN1987A in the LMC Using the Inn Baksan Underground Scintillation Telescope. *Phys. Lett. B*, *205*, 209–214. doi: 10.1016/0370-2693(88)91651-6
- Aloy, M. A., Müller, E., Ibáñez, J. M., Martí, J. M., & MacFadyen, A. (2000, March). Relativistic Jets from Collapsars. *ApJ*, *531*(2), L119-L122. doi: 10.1086/312537
- APS Dynamics. (2014, Mar). *APS 113 ELECTRO-SEIS Long Stroke Shaker*. https://www.apsdynamics.com/en/products/details/vibration-exciter/aps-113-ab.html?file=files/spektra_relaunch/inhalte/produktgruppen/datenblaetter/APS_113-AB_AB-HF_Data_Sheet_en.pdf.

- Banagiri, S., Covas, P., & Schofield, R. M. S. (2019, May). *PEM with Rain using HAM6 Vac accelerometer*.
<https://alog.ligo-wa.caltech.edu/aLOG/index.php?callRep=49495>. LIGO.
- Bhat, P. N., Meegan, C. A., von Kienlin, A., Paciesas, W. S., Briggs, M. S., Burgess, J. M., ... Zhang, B. (2016, apr). The third fermi gbm gamma-ray burst catalog: the first six years. *The Astrophysical Journal Supplement Series*, 223(2), 28. Retrieved from
<https://doi.org/10.3847/0067-0049/223/2/28> doi: 10.3847/0067-0049/223/2/28
- Bionta, R. M., et al. (1987). Observation of a Neutrino Burst in Coincidence with Supernova SN 1987a in the Large Magellanic Cloud. *Phys. Rev. Lett.*, 58, 1494. doi: 10.1103/PhysRevLett.58.1494
- Biscoveanu, S., Thrane, E., & Vitale, S. (2020, April). Constraining Short Gamma-Ray Burst Jet Properties with Gravitational Waves and Gamma-Rays. *ApJ*, 893(1), 38. doi: 10.3847/1538-4357/ab7eaf
- Blackburn, K., et al. (2019, May). *Specification of a common data frame format for interferometric gravitational wave detectors (igwd)*.
<https://dcc.ligo.org/LIGO-T970130>. LIGO Document Control Center.
- Blandford, R. D., & McKee, C. F. (1976). Fluid dynamics of relativistic blast waves. *The Physics of Fluids*, 19(8), 1130-1138. Retrieved from
<https://aip.scitation.org/doi/abs/10.1063/1.861619> doi: 10.1063/1.861619
- Blandford, R. D., & Znajek, R. L. (1977, 07). Electromagnetic extraction of energy from Kerr black holes. *Monthly Notices of the Royal Astronomical Society*, 179(3), 433-456. Retrieved from
<https://doi.org/10.1093/mnras/179.3.433> doi: 10.1093/mnras/179.3.433
- Brüel & Kjær. (2021, Jun). *Type 4809 portable shaker/vibration exciter*. <https://www.bksv.com/-/media/literature/Product-Data/bp0231.ashx>.
- Buikema, A., et al. (2020, Sep). Sensitivity and performance of the Advanced LIGO detectors in the third observing run. *Phys. Rev. D*, 102, 062003.
- Burlon, D., Ghirlanda, G., Ghisellini, G., Greiner, J., & Celotti, A. (2009, October). Time resolved spectral behavior of bright BATSE precursors. *A&A*, 505(2), 569-575. doi: 10.1051/0004-6361/200912662

- Burton, D., Ghirlanda, G., Ghisellini, G., Lazzati, D., Nava, L., Nardini, M., & Celotti, A. (2008, September). Precursors in Swift Gamma Ray Bursts with Redshift. *ApJ*, 685(1), L19. doi: 10.1086/592350
- Cannon, K., et al. (2012, March). Toward early-warning detection of gravitational waves from compact binary coalescence. *Astrophys. J.*, 748(2), 136.
- Chatterji, S., Blackburn, L., Martin, G., & Katsavounidis, E. (2004, sep). Multiresolution techniques for the detection of gravitational-wave bursts. *Class. Quantum Grav.*, 21(20), S1809–S1818.
- Chen, W.-X., & Beloborodov, A. M. (2007, mar). Neutrino-cooled accretion disks around spinning black holes. *The Astrophysical Journal*, 657(1), 383–399. Retrieved from <https://doi.org/10.1086/508923> doi: 10.1086/508923
- Christensen, N. (2018, Nov). Stochastic gravitational wave backgrounds. *Reports on Progress in Physics*, 82(1), 016903. Retrieved from <https://doi.org/10.1088/1361-6633/aae6b5> doi: 10.1088/1361-6633/aae6b5
- Cornish, N. J., & Littenberg, T. B. (2015, June). Bayeswave: Bayesian inference for gravitational wave bursts and instrument glitches. *Class. Quantum Grav.*, 32(13), 135012.
- Creighton, J. D. E., & Anderson, W. G. (2011). *Gravitational-wave physics and astronomy*. Wiley-VCH.
- Dai, Z. G., & Lu, T. (1998, May). Gamma-ray burst afterglows and evolution of postburst fireballs with energy injection from strongly magnetic millisecond pulsars. *A&A*, 333, L87-L90.
- Dall'Osso, S., Perna, R., Tanaka, T. L., & Margutti, R. (2017, February). Flares in gamma-ray bursts: disc fragmentation and evolution. *MNRAS*, 464(4), 4399-4407. doi: 10.1093/mnras/stw2695
- Davis, D., Massinger, T., Lundgren, A., Driggers, J. C., Urban, A. L., & Nuttall, L. (2019, February). Improving the sensitivity of Advanced LIGO using noise subtraction. *Class. Quantum Grav.*, 36(5), 055011.
- Davis, D., et al. (2021a, Apr). LIGO data quality vetoes applied to the analysis of o3. *LIGO*. Retrieved from https://dcc.ligo.org/public/0173/T2100045/001/DQdoc_03_draft.pdf

- Davis, D., et al. (2021b, Apr). LIGO detector characterization in the second and third observing runs. *Class. Quantum Grav.*, 38(13), 135014. Retrieved from <https://doi.org/10.1088/1361-6382/abfd85> doi: 10.1088/1361-6382/abfd85
- Ebersold, M., & Tiwari, S. (2020, May). Search for nonlinear memory from subsolar mass compact binary mergers. *Phys. Rev. D*, 101, 104041. Retrieved from <https://link.aps.org/doi/10.1103/PhysRevD.101.104041> doi: 10.1103/PhysRevD.101.104041
- Effler, A., Schofield, R. M. S., Frolov, V. V., González, G., Kawabe, K., Smith, J. R., ... McCarthy, R. (2015, Jan). Environmental influences on the LIGO gravitational wave detectors during the 6th science run. *Class. Quantum Grav.*, 32(3), 035017. doi: 10.1088/0264-9381/32/3/035017
- Eichler, D., Livio, M., Piran, T., & Schramm, D. N. (1989, July). Nucleosynthesis, neutrino bursts and γ -rays from coalescing neutron stars. *Nature*, 340(6229), 126-128. doi: 10.1038/340126a0
- Einstein, A. (1916). Die grundlage der allgemeinen relativitätstheorie. *Annalen der Physik*, 354(7), 769–822. Retrieved from <https://doi.org/10.1002/andp.19163540702> doi: 10.1002/andp.19163540702
- Farah, A., et al. (2020, June). Counting on Short Gamma-Ray Bursts: Gravitational-Wave Constraints of Jet Geometry. *ApJ*, 895(2), 108. doi: 10.3847/1538-4357/ab8d26
- Fryer, C. L., Holz, D. E., & Hughes, S. A. (2002, January). Gravitational Wave Emission from Core Collapse of Massive Stars. *ApJ*, 565(1), 430-446. doi: 10.1086/324034
- Fryer, C. L., & New, K. C. B. (2011). Gravitational waves from gravitational collapse. *Living Rev. Rel.*, 14, 1.
- Hardwick, T. (2019). High power and optomechanics in advanced ligo detectors. *LSU Doctoral Dissertations*. Retrieved from https://digitalcommons.lsu.edu/gradschool_dissertations/5107
- Hartle, J. B. (2003). *Gravity: An Introduction to Einstein's General Relativity* (illustrate ed.) [Book]. Benjamin Cummings.
- Henri, P. (1905). Sur la dynamique de l'électron. In *Proc. acad. sci* (Vol. 140, pp. 1504–1508).

- Hirata, K., Kajita, T., Koshiba, M., Nakahata, M., Oyama, Y., Sato, N., ... Cortez, B. G. (1987, April). Observation of a neutrino burst from the supernova SN1987A. *Phys. Rev. Lett.*, *58*(14), 1490-1493. doi: 10.1103/PhysRevLett.58.1490
- Jaranowski, P., & Krolak, A. (2009). *Analysis of gravitational-wave data*. Cambridge University Press. doi: 10.1017/CBO9780511605482
- Kalmus, P., Zanolin, M., & Klimenko, S. (2013). *Excluding source models with multiple astrophysical observations*.
- Kissel, J. (2017, Nov). *aligo seismic isolation and suspensions cartoon*. LIGO Document Control Center. Retrieved from <https://dcc.ligo.org/LIGO-G1200071/public>
- Klebesadel, R. W., Strong, I. B., & Olson, R. A. (1973, June). Observations of Gamma-Ray Bursts of Cosmic Origin. *ApJ*, *182*, L85. doi: 10.1086/181225
- Klimenko, S., Yakushin, I., Mercer, A., & Mitselmakher, G. (2008, May). A coherent method for detection of gravitational wave bursts. *Class. Quantum Grav.*, *25*(11), 114029.
- Koshut, T. M., Kouveliotou, C., Paciesas, W. S., van Paradijs, J., Pendleton, G. N., Briggs, M. S., ... Meegan, C. A. (1995, October). Gamma-Ray Burst Precursor Activity as Observed with BATSE. *ApJ*, *452*, 145. doi: 10.1086/176286
- Kouveliotou, C., Meegan, C. A., Fishman, G. J., Bhat, N. P., Briggs, M. S., Koshut, T. M., ... Pendleton, G. N. (1993, August). Identification of Two Classes of Gamma-Ray Bursts. *ApJ*, *413*, L101. doi: 10.1086/186969
- Kruk, J., & Schofield, R. M. S. (2016, Aug). *Environmental Monitoring: Coupling Function Calculator*. <https://dcc.ligo.org/LIGO-T1600387/public>. LIGO Document Control Center.
- Kuin, N. P. M., & Swift/UVOT Team. (2019, December). GRB 191221B: Swift/UVOT redshift. *GRB Coordinates Network*, *26538*, 1.
- Kumar, P., & Zhang, B. (2015, February). The physics of gamma-ray bursts & relativistic jets. *Phys. Rep.*, *561*, 1-109. doi: 10.1016/j.physrep.2014.09.008
- Lasky, P. D. (2015). Gravitational waves from neutron stars: A review. *Publications of the Astronomical Society of Australia*, *32*, e034. doi: 10.1017/pasa.2015.35
- Lazzati, D. (2005, February). Precursor activity in bright, long BATSE gamma-ray bursts. *MNRAS*, *357*(2), 722-731. doi: 10.1111/j.1365-2966.2005.08687.x

- Lazzati, D., Morsony, B. J., & Begelman, M. C. (2009, July). Very High Efficiency Photospheric Emission in Long-Duration γ -Ray Bursts. *ApJ*, *700*(1), L47-L50. doi: 10.1088/0004-637X/700/1/L47
- Lee, H. K., Wijers, R. A. M. J., & Brown, G. E. (2000, January). The Blandford-Znajek process as a central engine for a gamma-ray burst. *Phys. Rep.*, *325*(3), 83-114. doi: 10.1016/S0370-1573(99)00084-8
- Lynch, R., Vitale, S., Essick, R., Katsavounidis, E., & Robinet, F. (2017, May). Information-theoretic approach to the gravitational-wave burst detection problem. *Phys. Rev. D*, *95*, 104046.
- MacFadyen, A. I., Woosley, S. E., & Heger, A. (2001, March). Supernovae, Jets, and Collapsars. *ApJ*, *550*(1), 410-425. doi: 10.1086/319698
- Macleod, D., Urban, A. L., Coughlin, S., Massinger, T., Pitkin, M., Rngeorge, ... Badger, T. G. (2021). *gwpy/gwpy: Gwpy 2.1.3*. Zenodo. Retrieved from <https://zenodo.org/record/5788702> doi: 10.5281/ZENODO.5788702
- Maoz, D., & Badenes, C. (2010, 09). The supernova rate and delay time distribution in the Magellanic Clouds. *Monthly Notices of the Royal Astronomical Society*, *407*(2), 1314-1327. Retrieved from <https://doi.org/10.1111/j.1365-2966.2010.16988.x> doi: 10.1111/j.1365-2966.2010.16988.x
- Metzger, B. D., Giannios, D., Thompson, T. A., Bucciantini, N., & Quataert, E. (2011, 05). The protomagnetar model for gamma-ray bursts. *Monthly Notices of the Royal Astronomical Society*, *413*(3), 2031-2056. Retrieved from <https://doi.org/10.1111/j.1365-2966.2011.18280.x> doi: 10.1111/j.1365-2966.2011.18280.x
- Misner, C. W., Thorne, K. S., & Wheeler, J. A. (1973). *Gravitation* (Misner, C. W., Thorne, K. S., & Wheeler, J. A., Ed.).
- Mogushi, K., Cavaglià, M., & Siellez, K. (2019, Jul). Jet geometry and rate estimate of coincident gamma-ray burst and gravitational-wave observations. *ApJ*, *880*(1), 55. Retrieved from <http://dx.doi.org/10.3847/1538-4357/ab1f76> doi: 10.3847/1538-4357/ab1f76
- Mu, H.-J., et al. (2018). Central-engine-powered Bright X-Ray Flares in Short Gamma-Ray Bursts: A Hint of a Black Hole–Neutron Star Merger? *Astrophys. J.*, *858*(1), 34. doi: 10.3847/1538-4357/aaba14

- Mueller, G. (2005, Sep). Beam jitter coupling in advanced ligo. *Opt. Express*, *13*(18), 7118–7132. Retrieved from <http://opg.optica.org/oe/abstract.cfm?URI=oe-13-18-7118> doi: 10.1364/OPEX.13.007118
- Nakar, E. (2007). Short-hard gamma-ray bursts. *Physics Reports*, *442*(1), 166-236. Retrieved from <https://www.sciencedirect.com/science/article/pii/S0370157307000476> (The Hans Bethe Centennial Volume 1906-2006) doi: <https://doi.org/10.1016/j.physrep.2007.02.005>
- Nguyen, P. (2020, Apr). *PEM Coupling Function Tools*. <https://git.ligo.org/pem/pemcoupling>. GitLab.
- Nguyen, P., et al. (2021, jun). Environmental noise in Advanced LIGO detectors. *Class. Quantum Grav.*, *38*(14), 145001. Retrieved from <https://doi.org/10.1088/1361-6382/ac011a> doi: 10.1088/1361-6382/ac011a
- Nguyen, P., & Schofield, R. M. S. (2019, May). *Coupling estimates from PEM injections correctly predict LLO DARM glitch near S190510g from thunder-driven vibration at EY*. <https://alog.ligo-la.caltech.edu/aLOG/index.php?callRep=46025>. LIGO.
- Nguyen, P., & Schofield, R. M. S. (2020, Jul). *Coupling estimates of helicopter flyovers at both sites during O3*. <https://alog.ligo-wa.caltech.edu/aLOG/index.php?callRep=56285>. LIGO.
- Norris, J. P., & Bonnell, J. T. (2006, May). Short Gamma-Ray Bursts with Extended Emission. *ApJ*, *643*(1), 266-275. doi: 10.1086/502796
- Perna, R., Armitage, P. J., & Zhang, B. (2006, January). Flares in Long and Short Gamma-Ray Bursts: A Common Origin in a Hyperaccreting Accretion Disk. *ApJ*, *636*(1), L29-L32. doi: 10.1086/499775
- Piezosystems. (n.d.). *Piezo nanopositioning devices, actuators & controllers*. <https://www.piezosystem.com/>.
- Piro, A. L., & Pfahl, E. (2007, April). Fragmentation of Collapsar Disks and the Production of Gravitational Waves. *ApJ*, *658*(2), 1173-1176. doi: 10.1086/511672
- Planck Collaboration, et al. (2020). Planck 2018 results - vi. cosmological parameters. *A&A*, *641*, A6. Retrieved from <https://doi.org/10.1051/0004-6361/201833910> doi: 10.1051/0004-6361/201833910

- Radice, D., Morozova, V., Burrows, A., Vartanyan, D., & Nagakura, H. (2019, May). Characterizing the Gravitational Wave Signal from Core-collapse Supernovae. *ApJ*, *876*(1), L9. doi: 10.3847/2041-8213/ab191a
- Rastinejad, J. C., Gompertz, B. P., Levan, A. J., Fong, W., Nicholl, M., Lamb, G. P., ... Thöne, C. C. (2022). *A kilonova following a long-duration gamma-ray burst at 350 mpc*. arXiv. Retrieved from <https://arxiv.org/abs/2204.10864> doi: 10.48550/ARXIV.2204.10864
- Rees, M. J., & Meszaros, P. (1994, August). Unsteady Outflow Models for Cosmological Gamma-Ray Bursts. *ApJ*, *430*, L93. doi: 10.1086/187446
- Riess, A., et al. (2021, 12). A comprehensive measurement of the local value of the hubble constant with 1 km/s/mpc uncertainty from the hubble space telescope and the sh0es team.
- Riles, K. (2017, Dec). Recent searches for continuous gravitational waves. *Modern Physics Letters A*, *32*(39), 1730035. Retrieved from <http://dx.doi.org/10.1142/S021773231730035X> doi: 10.1142/s021773231730035x
- Santamaría, L., & Ott, C. (2013, Aug). *Analytic ccsn waveforms: 2. accretion disk instabilities*. LIGO Document Control Center. Retrieved from <https://dcc.ligo.org/LIGO-T1100093/public>
- Schofield, R., Effler, A., Nguyen, P., et al. (2021). *PEM central*. <http://pem.ligo.org>.
- Schofield, R. M. S. (2013, Mar). *Investigations of magnetic coupling to the quads*. <https://dcc.ligo.org/LIGO-G1300300/public>. LIGO Document Control Center.
- Schofield, R. M. S. (2018, Nov). *Lightning, LIGO, and GW150914*. <https://dcc.ligo.org/LIGO-T1800506/public>. LIGO Document Control Center.
- Schofield, R. M. S., Nguyen, P., Banagiri, S., Merfeld, K., & Effler, A. (2019, May). *HVAC noise in DARM roughly consistent with prediction for septum from PEM injections*. <https://alog.ligo-wa.caltech.edu/aLOG/index.php?callRep=48912>. LIGO.
- Schofield, R. M. S., Nguyen, P., Roma, V., Palamos, J., Schale, P., Effler, A., ... Frey, R. (2018, Nov). *PEM vetting report for GW170817*. <https://dcc.ligo.org/LIGO-T1800508/public>. LIGO Document Control Center.

- Schofield, R. M. S., Roma, V., Palamos, J., Hardwick, T., Effler, A., Frey, R., & Talukder, D. (2018, Nov). *PEM vetting report for GW150914*. <https://dcc.ligo.org/LIGO-T1800505/public>. LIGO Document Control Center.
- Soni, S., et al. (2020, Dec). Reducing scattered light in LIGO's third observing run. *Class. Quantum Grav.*, 38(02), 025016.
- Sun, L., Goetz, E., Kissel, J. S., Betzwieser, J., Karki, S., Bhattacharjee, D., ... Urban, A. (2021, June). Characterization of systematic error in Advanced LIGO calibration in the second half of O3. *arXiv e-prints*, arXiv:2107.00129.
- Sutton, P. J. (2013, 3). A Rule of Thumb for the Detectability of Gravitational-Wave Bursts.
- Sutton, P. J., Jones, G., Chatterji, S., Kalmus, P., Leonor, I., Poprocki, S., ... Was, M. (2010, may). X-pipeline: an analysis package for autonomous gravitational-wave burst searches. *New Journal of Physics*, 12(5), 053034. Retrieved from <https://doi.org/10.1088/1367-2630/12/5/053034> doi: 10.1088/1367-2630/12/5/053034
- Swift grb archive*. (2022, July). NASA. Retrieved from https://swift.gsfc.nasa.gov/archive/grb_table/
- Taluker, D., Nguyen, P., et al. (2021, Dec). *LIGO Channel Activity Monitor*. <https://git.ligo.org/pem/ligocam>. GitLab.
- Usman, S., et al. (2016, October). The PyCBC search for gravitational waves from compact binary coalescence. *Class. Quantum Grav.*, 33(21), 215004.
- van Putten, M. H. (2001, August). Proposed Source of Gravitational Radiation from a Torus around a Black Hole. *Phys. Rev. Lett.*, 87(9), 091101. doi: 10.1103/PhysRevLett.87.091101
- van Putten, M. H. P. M., Lee, G. M., Della Valle, M., Amati, L., & Levinson, A. (2014, October). On the origin of short GRBs with extended emission and long GRBs without associated SN. *MNRAS*, 444, L58-L62. doi: 10.1093/mnrasl/slu113
- van Putten, M. H. P. M., Levinson, A., Lee, H. K., Regimbau, T., Punturo, M., & Harry, G. M. (2004, Feb). Gravitational radiation from gamma-ray burst-supernovae as observational opportunities for ligo and virgo. *Phys. Rev. D*, 69, 044007. Retrieved from <https://link.aps.org/doi/10.1103/PhysRevD.69.044007> doi: 10.1103/PhysRevD.69.044007

- Vedrenne, G., & Atteia, J.-L. (2009). *Gamma-Ray Bursts*. doi: 10.1007/978-3-540-39088-6
- Vielfaure, J. B., Arabsalmani, M., Heintz, K. E., Tanvir, N. R., de Ugarte Postigo, A., Malesani, D. B., ... Stargate Collaboration (2019, December). GRB 191221B: VLT/X-shooter redshift. *GRB Coordinates Network*, 26553, 1.
- Vielfaure, J. B., & Stargate Collaboration. (2020, February). GRB 200205B: VLT/X-shooter redshift. *GRB Coordinates Network*, 26998, 1.
- von Kienlin, A., Meegan, C. A., Paciesas, W. S., Bhat, P. N., Bissaldi, E., Briggs, M. S., ... Wilson-Hodge, C. A. (2020, apr). The fourth fermi-GBM gamma-ray burst catalog: A decade of data. *The Astrophysical Journal*, 893(1), 46. Retrieved from <https://doi.org/10.3847/1538-4357/ab7a18> doi: 10.3847/1538-4357/ab7a18
- Wang, X.-Y., & Mészáros, P. (2007, December). GRB Precursors in the Fallback Collapsar Scenario. *ApJ*, 670(2), 1247-1253. doi: 10.1086/522820
- Washimi, T., Yokozawa, T., Tanaka, T., Itoh, Y., Kume, J., & Yokoyama, J. (2020). Method for environmental noise estimation via injection tests for ground-based gravitational wave detectors.
- Weber, J. (1968, Jun). Gravitational-wave-detector events. *Phys. Rev. Lett.*, 20, 1307–1308. Retrieved from <https://link.aps.org/doi/10.1103/PhysRevLett.20.1307> doi: 10.1103/PhysRevLett.20.1307
- Woosley, S. E. (1993, March). Gamma-Ray Bursts from Stellar Mass Accretion Disks around Black Holes. *ApJ*, 405, 273. doi: 10.1086/172359
- Zhang, W., Woosley, S. E., & MacFadyen, A. I. (2003, March). Relativistic Jets in Collapsars. *ApJ*, 586(1), 356-371. doi: 10.1086/367609